SEISMIC ROTATIONAL DATA: ACQUISITION, PROCESSING AND APPLICATIONS

A DISSERTATION
SUBMITTED TO THE DEPARTMENT OF GEOPHYSICS
AND THE COMMITTEE ON GRADUATE STUDIES
OF STANFORD UNIVERSITY
IN PARTIAL FULFILLMENT OF THE REQUIREMENTS
FOR THE DEGREE OF
DOCTOR OF PHILOSOPHY

Ohad Barak
April 2017

© Copyright 2017 by Ohad Barak
All Rights Reserved

Printed as Stanford Exploration Project No. 167
by permission of the author

Copying for all internal purposes of the sponsors
of the Stanford Exploration Project is permitted

I certify that I have read this dissertation and that, in my opinion, it is fully adequate in scope and quality as a dissertation for the degree of Doctor of Philosophy.

(Biondo L. Biondi) Principal Adviser

I certify that I have read this dissertation and that, in my opinion, it is fully adequate in scope and quality as a dissertation for the degree of Doctor of Philosophy.

(Gerald Mavko)

I certify that I have read this dissertation and that, in my opinion, it is fully adequate in scope and quality as a dissertation for the degree of Doctor of Philosophy.

(Joshua Ronen)

Approved for the University Committee on Graduate Studies.

Abstract

Rotations of the ground as a result of the propagation of seismic energy are one of the least-studied phenomena in seismology. This is curious, since unlike other, more complicated geophysical theories, rotations are an observable that we can measure on the Earth's surface. Furthermore, the concept of medium rotation is inherent to elastic continuum theory, and has been known to exist for as long as seismic measurements have been made. In many fields of technology (the aerospace and gaming industry, for example), it is well-understood that to measure motion of a finite body it is necessary to measure both 3D translations and 3D rotations.

However, the industry-standard measurements in exploration and in earthquake seismology have always been of translations on land, pressure in water, or both translations and pressure on the seabed. There is currently no technological solution which would enable the seismological community to record rotational data on a scale similar to the recording of translations.

Part of the reasons for this are circumstantial: the instruments that were more readily available at the time that basic seismological research was taking place measured translations, not rotations. These instruments were improved over the years, leading to the development of the robust geophones and accelerometers common today, with their high sensitivity and wide dynamic range. In marine seismic acquisition, a sensor that measures pressure is the obvious choice, and indeed hydrophones are the mainstay of marine seismic data acquisition. Furthermore, the design of an instrument which would record only rotations and yet would be insensitive to translations is not obvious.

The availability of a particular type of observable data inspired research to acquire and process these data for imaging of the Earth's subsurface (exploration seismology) and for deriving earthquake source mechanisms (earthquake seismology). Geophysical

research (and the resulting extraction of Earth's mineral resources) has been very successful using existing translational and pressure data. So successful, in fact, that the mere idea that the data are incomplete appears either prepostorous or irrelevant upon initial inspection.

The elastodynamic seismic wavefield contains more than just three components of translations and one of pressure. However, until very recently the seismic industry has not asked itself the very simple question: "what observables out of the elastodynamic seismic wavefield would we ideally like to record ?"

My purpose in this dissertation is to show how to include rotational data in the seismic acquisition and processing workflow. I use the term "6C data" to refer to data comprising three components of translations and three components of rotation, and "7C data" if hydrophone data are also included.

First, I cover some of the current rotational-acquisition methods, discussing their benefits and shortcomings. I then propose using existing induction-coil magnetometer technology to record rotations, and show a field data experiment where this possibility is validated.

The combination of rotational motion records together with current translational motion records can aid in the processing of seismic data by providing extra information about the seismic wave modes being recorded. I show one application where particular wave modes are selected and separated from a multicomponent field dataset that has both translational and rotational components.

The use of machine learning algorithms in exploration seismology is not new, and is currently seeing a resurgance due to the rapid increase in data volumes and complexity. I show how to extract feature vectors from a multicomponent dataset comprising both translational and rotational components, and use them as a training set for a machine learning algorithm. This algorithm can then identify particular wave modes based on this training. The possibility of using a machine learning algorithm to identify and separate wave modes from large seismic data volumes is compelling, as it has the potential for saving on time-consuming manual processing steps.

Preface

The electronic version of this report[1] makes the included programs and applications available to the reader. The markings **ER**, **CR**, and **NR** are promises by the author about the reproducibility of each figure result. Reproducibility is a way of organizing computational research that allows both the author and the reader of a publication to verify the reported results. Reproducibility facilitates the transfer of knowledge within SEP and between SEP and its sponsors.

ER denotes Easily Reproducible and are the results of processing described in the paper. The author claims that you can reproduce such a figure from the programs, parameters, and makefiles included in the electronic document. The data must either be included in the electronic distribution, be easily available to all researchers (e.g., SEG-EAGE data sets), or be available in the SEP data library[2]. We assume you have a UNIX workstation with Fortran, Fortran90, C, X-Windows system and the software downloadable from our website (SEP makerules, SEPScons, SEPlib, and the SEP latex package), or other free software such as SU. Before the publication of the electronic document, someone other than the author tests the author's claim by destroying and rebuilding all ER figures. Some ER figures may not be reproducible by outsiders because they depend on data sets that are too large to distribute, or data that we do not have permission to redistribute but are in the SEP data library, or that the rules depend on commercial packages such as Matlab or Mathematica.

CR denotes Conditional Reproducibility. The author certifies that the commands are in place to reproduce the figure if certain resources are available. The primary reasons for the CR designation is that the processing requires 20 minutes

[1] http://sepwww.stanford.edu/public/docs/sep165
[2] http://sepwww.stanford.edu/public/docs/sepdatalib/toc_html/

or more.

NR denotes Non-Reproducible figures. SEP discourages authors from flagging their figures as NR except for figures that are used solely for motivation, comparison, or illustration of the theory, such as: artist drawings, scannings, or figures taken from SEP reports not by the authors or from non-SEP publications.

Our testing is currently limited to LINUX 2.7 (using the Intel Fortran90 compiler) and the SEPlib-7.0.5 distribution, but the code should be portable to other architectures. Reader's suggestions are welcome. For more information on reproducing SEP's electronic documents, please visit *http://sepwww.stanford.edu/research/redoc/*.

Acknowledgments

Only one author's name is ever written in the title of a scientific thesis. What an atrocity! The confluence of forces, people, circumstances and pure luck that have to mix in the right proportions in order that a thesis may be produced must be very specific, so I find it difficult to take credit for this thesis. I feel more like I've just played one of the many roles that brought it to fruition. The hardest part for me was to change all the "we"s in the text to "I"s. (we were not encouraged to think in the singular form in our Kibbutz).

Before mentioning anyone, however, most of the credits for this thesis should go to my wife. It was she who pushed me kicking and screaming into academia, all the way from my small Kibbutz to a strange land on the other side of an ocean and a continent. Since then, she has been (mostly) patiently waiting for me to finally finish up and join the adult world, while earning a living for the family. Love is. She also gave me a son, who wakes me up with bird sounds every morning at around 6:00 to see the sunrise, and who shows me the world with fresh eyes every day.

Although under my name, this thesis is not mine but ours, us, the Stanford Exploration Project. The research presented here would simply not have happened were it not for the unparalleled resource that SEP has: it's people. I owe all these people for many things: Biondo, for never giving up on me, even when it looked like I was totally lost, and for helping me find new ways forward in dark times. I've come to greatly appreciate the practical way Biondo approaches problems, and I hope I picked up on some of it. He also pushed me into running the Silver Lake survey, which has turned out to be the most original part of this thesis. Shuki, my partner in crime, for fearlessly pushing me into ever more esoteric research, and for teaching me the rudementaries of American mannerisms, against my will. Jon, for his wierd, clever ideas, and for showing all of us how to stare for hours at a seismic section and

see new things, and ask "why?". Bob, for always showing us very clearly how we should be doing things, and not despairing when we don't. Stew, for remembering everything, from the most obscure pieces of SEP code, to the smallest comma in a paper reference. They say an elephant never forgets, but whatever the elephant does forget, Stew will be there to remind him. My dear dear friends Elita and Mandy, for sharing an office and their lives with me for 4 years, and making our little office space feel like home. Ali, ("Saidna Ali") who can explain anything well and make anybody feel smarter than they are, and who gave me some of his calm sanity in tough stretches. Chris, for sharing my horrible Austin Powers and Monty Python jokes, and for the delectable gin and tonics. Yang, for his funny, eccentric ways and his full heart that he keeps hidden. Yi, for her energy and her ability to always be happy, smiling and hopeful, no matter the circumstances. Gustavo, for his calm manner and excellent humor, and always listening to my ramblings. Guillaume, with his dark jokes, his complaints about everything, reminding me that not all is rosy in the world but that it's still funny somehow. Ettore, for teaching me things I should have learned in my first year. Sjoerd, for being annoying, unforgiving and unbending, and thus pushing my research by leaps and bounds. That's how good friends help you. Musa, who despite having three kids and zero time, somehow always managed to find time to talk to me and inspire my research. Fantine, for pushing me to pick up some machine learning tricks at the last minute. Yaxun, Claudio, Xukai, Adam, Jason, Huy, Taylor, Eileen, Daniel, Joe, and all others who I may have forgotten but have shared seminar slots in Mitchell with me.

There is only one way to do research, and that is together. SEP's greatest strength is the relationships between the students, the things we do for each other, the life that we cultivate and tend between seminars, reports and meetings. I have been beyond any reasonable definition of lucky to have been part of the SEP group, and to stand on the shoulders of giants. Thank you all, beaucoup.

Research does not generate money, at least not right away, and SEP would not exist without all of our group's sponsors. I wish to thank all SEP's sponsoring companies for ensuring that we can continue doing our research without worrying about where the next paycheck will come from, especially during the recent period when the oil and gas industry has been struggling.

Sitting with Jack Dvorkin in his office and getting some one-on-one instruction

into rock physics and the methods of constructing effective media parameters was also a pleasure, not least because of Jack being very liberal with his use of language and certain non-politically correct Russian phrases. I have also had the pleasure of Gary's dry humor in his rock-physics class, which actually helped me remember much of the material later on, so I suspect he uses humor as a teaching aid.

I would also like to thank the administration staff in the Geophysics dept., who make life easy for all of us. Diane Lau, who retired from being the SEP administrator after 25 years in the business, made sure to organize everything for us at our various meetings, and also made sure to put me in a room with someone who does not snore. Claudia Baroni and Liliane Perreira, who have replaced Diane and continue the tradition of keeping us students away from having to deal with anything not researchy. I also thank our department administrators Nancy Masarweh and Michelle Brunner, who helped me through department bureaucracy, and laughed at my obnoxious humor.

A special mention must go to Robert Brune. It was Bob's boundless determination to get people interested in rotational data that caught Shuki's attention, and then my own. His ongoing contribution to my research included many hours of phonecalls where I tapped his copious knowledge for ideas that would help me with my work. Bob helped Fred Herkenhoff from Chevron incorporate rotation sensors in Chevron's Kettleman survey, which is the dataset I tested most of my methods on. He is a wellspring of fresh, original ideas, and I hope that some of them at least get to a field-testing stage. He is also the man behind the original idea for the seisball display.

I also wish to thank Chevron for releasing the Kettleman data, and particularly to thank Fred Herkenhoff and Ranjan Dash for processing the data so I could use it.

I'm also indebted to my Professors from Tel-Aviv University, Moshe Reshef and Dan Kosloff, for getting me interested in geophysics in the first place and showing me that it is a wonderful combination of computer science, physics, engineering and math. I also thank Dov and Rachel Greenberg, for teaching me about gratitude and how it transforms the world. Shehechiyanu.

My parents (and my sister, who still thinks she's my mother) aren't the kind who push their children into higher education at all costs. They are happy when I'm doing whatever fulfills me. Mostly, they taught me how to perservere in any situation, and

how to take everything in proportion. I learned from them about being resilient in all aspects of life. They also provide me with that ever important feeling of absolutely knowing that there will always be a place for me to return to.

Every day here has been a gift. I hope I can pass some of these gifts forward.

"*I don't know where I'm going, but I sure ain't lost*"

– – – Jess Lair

"*Sometimes it's a little better to travel than to arrive*"

– – – Robert Pirsig, Zen and the Art of Motorcycle Maintenance

"*Truth is stranger than fiction, but it is because fiction is obliged to stick to possibilities; Truth isn't.*"

– – – Samuel Langhorne Clemens

Contents

Abstract **vi**

Preface **viii**

Acknowledgments **xi**

1 Introduction **1**

2 Seismic rotations from induction-coil magnetometers **19**

3 Wave-mode separation with translations and rotations **61**

4 Automatic wave mode identification using machine learning **111**

Bibliography **137**

List of Tables

3.1 Example two-component input data for SVD. 67

List of Figures

1.1 Sketch of the six degrees of freedom of a rigid body in a 3D world. To know what an aircraft is doing, it is not sufficient to know its linear velocity but also its rotations. There are three components to the velocity, and in addition there are three components to the rotation: roll, pitch, and yaw. [**NR**] 2

1.2 The inner ear, the human multicomponent recorder. Utricle and saccule detect linear acceleration, while the semicircular canals detect rotations. Cochlea detects pressure changes. (Blausen, 2014). [**NR**] . . 3

1.3 Two points, P and Q, are separated by $\delta\mathbf{x} = (\delta x, \delta y, \delta z)$. P is displaced by $\mathbf{u}$, and Q is displaced by $\mathbf{u} + \delta\mathbf{u}$. [**NR**] 3

1.4 Dilatational strain field, which generates a fractional volume change but no rotation. [**NR**] 5

1.5 Simple shear strain field, which generates rotation but no volume change. Figure from Pujol (2003). [**NR**] 6

1.6 Pure shear type I strain field, which generates no rotation and no volume change. Figure from Pujol (2003). [**NR**] 7

1.7 Pure shear type II strain field, which generates no rotation and no volume change. Figure from Pujol (2003). [**NR**] 7

1.8 Pure rotation strain field, which generates no volume change. Figure from Pujol (2003). [**NR**] 8

1.9 The medium strains generated by the passage of seismic body waves in an unbounded homogeneous medium. (a) A plane P wave, which generates a dilatational strain. (b) A plane shear wave, which generates a simple shear strain. As a result of their perpendicular propagation directions, the translations of these two waves are identical, even though the strains are different. [**NR**] 11

1.10 The medium strains generated by the passage of seismic surface waves in a laterally homogeneous medium. (a) A Rayleigh wave, which generates a combination of dilatational and rotational strains. (b) A Love wave, which generates shear and rotational strains. (http://web.ics.purdue.edu/braile/edumod [**NR**] 12

1.11 Comparison of the seisball visualization for a three-component data trace representing only translational components (left) vs the same data trace but with six-components representing both translational and rotational components (right). The data are from the Kettleman six-component survey (described in chapter 3), where both translations and rotations were recorded. Note how much richer in ground motion information the 6C data are. Current seismic acquisition only records 3C data like the trace on the left. [**ER**] 13

2.1 a) The ring laser gyroscope in Wettzell, Germany (Source: http://www.fs.wettzell.de). b) Schematic of the ring laser's operation principle (Source: https://en.wikipedia.org/wiki/Sagn Two beams of laser light are shot in opposite directions. If the structure rotates around the axis perpendicular to the plane of the light beams, a frequency interference proportional to the rotation will occur as a result of the change of the length of the path the light beams traverse. [**NR**] 21

2.2 a) a Fiber-optic ring laser gyroscope schematic (Source: http://web.ixblue.com/cn/aw6ym/fibe gyroscope). b) Schematic of the operating principle of a fiber-optic ring laser gyroscope (Source: https://en.wikipedia.org/wiki/Fibre_optic_gyroscope). Light is shot into both ends of the coiled fiber. The light beams' interference will change in proportion to the rotation rate of the instrument. [**NR**] 22

2.3 a) A Magnetohydrodynamic sensor. b) Schematic of a magnetohydrodynamic sensor capable of recording rotational signals down to 10^{-6} rad/sec. A magnet fixed to the sensor casing generates a magnetic flux through the center of the instrument. A conducting fluid acts as an inertial proof mass, when the sensor rotates, the relative velocity between the fluid and the magnetic flux generates a radial electric field, proportional to the rotation rate. (Source: http://www.aptec.com/) [**NR**] 24

2.4 a) An R2 electrokinetic inertial rotation sensor in its casing, approximately 12 cm on each side (The model name given by the original company that built them is "METR03"). b) The internals of the sensor, showing the ring structures. The ring structures are filled with an electrolytic fluid, which generates a current when the sensor rotates around the axis perpendicular to the ring. The amount of current is proportional to the rotation rate. Each sensor has three perpendicular rings, and can therefore record 3-component ground rotations (Figure courtesy of Robert Brune). [**NR**] 25

2.5 a) A Rotaphone instrument. The diameter of the disc is 44.5 cm. b) Schematic of the Rotaphone. The sensor system consists of vertical and horizontal geophones mounted in parallel pairs to a rigid frame anchored to the ground. Separation distance between each geophone pair along the circumference of the disc is 40 cm, much smaller than the seismic wavelength the instrument is designed to record. According to its designers, the dynamic range of the rotaphone is 120 dB, and it can record rotations down to 4 nrad/s. (Source: http://rotaphone.eu) [**NR**] 27

2.6 Induction-Coil Magnetometers, built by the Scripps Institute of Oceanography. Coils of aluminium wire are wound around a magnetically permeable core. A current is induced in the wire when the magnetic flux perpendicular to the coil's cross section changes. [**NR**] 29

2.7 Illustration of how ground rotation is recorded on the magnetic field sensor as represented by the compass, which is coupled to the ground. (a) Before ground rotation, the magnetic field (red) is recorded only by the North component (yellow). (b) During ground rotation, the magnetic field (red) does not change, but its projection on the North and East components (yellow) changes. We can calculate the amount of rotation from the change in projection. Note that translations of the ground will not result in a change of the projection of the magnetic field on the magnetic components. [**NR**] 29

2.8 (a), (c) and (e): Changes in magnetic projections on three orthogonal components as a result of rotations of the components within a constant magnetic field $\vec{H} = (0, 0, 1)$ (a vertical magnetic field, as is the case in the Earth's North pole). (b), (d) and (f): The rigid-body rotations (solid lines) that caused the change in magnetic projections, and the rotations derived from the changes in magnetic projections (dashed lines). In (a) and (b), the rotation axis is $\vec{u} = (1, 0, 0)$ (only around the X axis), and the rotation is recovered correctly. In (c) and (d), the rotation axis is $\vec{u} = \left(\frac{\sqrt{2}}{2}, \frac{\sqrt{2}}{2}, 0.\right)$ and the rotations are recovered correctly. In (e) and (f), the rotation axis is $\vec{u} = \left(\frac{\sqrt{3}}{3}, \frac{\sqrt{3}}{3}, \frac{\sqrt{3}}{3}\right)$ The rotation around the Z axis (the direction of the magnetic field) is not recovered correctly. Rotations around the magnetic field axis cannot be derived since they do not cause a change in the projections. [**ER**] 37

2.9 (a) The arrangement of a single composite station in the Silver Lake survey. Each station had 3 orthogonal ICMs, and a 3C inertial rotations sensor. Two geophones were placed in close proximity in the inline and in the crossline directions. (b) 20 shots were executed off-end, at 5-meter intervals, for a total of 100m of offset. The 'X' (roll) components of the rotation sensors and the ICMs were along the inline direction toward magnetic heading 30^o. The 'Y' (pitch) components of the rotation sensors and the ICMs were along the crossline direction toward magnetic heading 120^o. The 'Z' (yaw) components are downward, while magnetic inclination was 60^o. Note that the figure is not to scale. The distance between the composite stations was 3 meters. [**NR**] 39

2.10 (a) Execution of one of the 20 shots using the Betsy gun. (b) One of the 3 composite stations. The rotation sensor is housed in the grey box, while the ICMs are the white rods arranged orthogonally. (c) We placed one remote 3-component ICM station far from where we were shooting the seismic data, to record the ambient magnetotelluric noise for later removal in processing. [**NR**] 40

2.11 Magnetotelluric magnetic and electric fields observed at Silver Lake, Mojave Desert in March 2015, two months before we performed the Silver Lake survey. Also shown is the public-domain noise floor of the Zonge model ANT/6 magnetometer. Spikes are from 60 Hz power line noise and 0.2 Hz cathodic protection system on a nearby gas pipeline. [**NR**] 42

2.12 Log amplitude spectra of raw data during active shooting, after instrument designature for the various data components was applied. a) Magnetometers before removal of ambient noise. b) Ambient magnetic noise at remote station. c) Magnetometers after removal of ambient noise. d) Vertical geophone. e) Rotation sensors. The B_z component at the remote station recording the vertical ambient magnetic field had problems with its electronics, and therefore recorded much higher levels of noise than were actually in the field. Note the reduction in noise for the B_x and B_y magnetometer components after removal of the ambient field recording. Note that the vertical geophone was recording very low frequencies in the microseism band (below 2 Hz), while the rotation sensors were not, indicating that the rotation sensors we used do not have sufficient sensitivity at the very low end of spectrum. [**ER**] 44

2.13 Silver Lake receiver gathers at station 1, in the 5 - 30 Hz frequency band. (a) Vertical geophone. (b) Yaw rotation sensor. (c) Inline vertical geophone difference, which estimates the pitch component. (d) Pitch rotation sensor. (e) Crossline vertical geophone difference, which estimates the roll component. (f) Roll rotation sensor. Clipped values are indicated in red. The direct wave propagating at V=1420 m/sec is very weak and cannot be seen at this clip level. There are two strong Rayleigh wave modes propagating at V=135 m/sec and V=250 m/sec. These are present as rotations measured by geophone-differencing and by the rotations sensors themselves. The amplitudes of the rotations calculated by geophone differencing are greater than those measured by the rotation sensors. [**ER**] 47

2.14 The phase difference between the rotations estimated from vertical geophone differencing and the rotations from the rotation sensors, within the passband. (a) Phase difference for the pitch component. (b) Phase difference for the roll component. Observe that for the roll we do not get a consistent phase difference for the 3 composite stations. There is not much energy on the roll component, therefore the signal to noise ratio is low and it is difficult to estimate the phase difference reliably for all stations. Also, I could not get an estimation of the yaw component from geophone differencing. Therefore, I designatured the rotation-sensors' pitch, roll and yaw components using the pitch phase difference, which appeared to be reliable across stations. [**ER**] 48

2.15 Magnetometer receiver gather at station 1 after designature of the ICMs, before and after removal of the MT field acquired by the remote station. (a) X component. (b) X component of remote station. (c) X component after subtraction of MT field acquired by remote station. (d) Y component. (e) Y component of remote station. (f) Y component after subtraction of MT field acquired by remote station. (g) Z component. (h) Z component of remote station. (i) Z component after subtraction of MT field acquired by remote station. Note that we had instrument problems with the Z component of the remote station (h), and therefore subtracting the MT noise from the Z component produced noisier data than the original. Consequently, for further analysis I used the data shown in (g) rather than the data shown in (i). Note that these data are after application of a bandpass filter between 5 Hz and 30 Hz. [**ER**] 50

2.16 Comparison of rotations derived from ICMs to rotations measured by rotation sensors. (a) Pitch derived from ICM. (b) Pitch measured by rotation sensor. (c) Roll derived from ICM. (d) Roll measured by rotation sensor. (e) Yaw derived from ICM. (f) Yaw measured by rotation sensor. Note the similarity in amplitudes of the Rayleigh-wave arrivals between the magnetometer-derived rotations and those measured by the rotation sensor. Also, note the large phase difference of the pitch component. [**ER**] 53

2.17 Comparison of the rotations measured by rotation sensors (red wiggles) and rotations derived from ICM components (black wiggles). (a), (c) and (e) are the data comparison for station 1 for the pitch, roll and yaw components, respectively. AGC has been applied for display. (b), (d) and (f) are the averaged phase difference between the two signals for all 3 receiver stations. The roll rotational signal is very weak (see Figure 2.16(d)), and the low signal to noise ratio causes the phase difference to be inconsistent across stations for the roll component. [**ER**] 54

2.18 Comparison of the recorded magnetometer data (black wiggles) to forward-modeled magnetic projections (red wiggles) derived from the magnetometer rotations. (a), (c) and (e) are the data comparison for station 1 for the B_x, B_z and B_y components, respectively. AGC has been applied for display. (b), (d) and (f) are the averaged phase difference between the two signals for all 3 receiver stations. Recall that I could not remove the ambient magnetic noise from the 'Z' magnetometer component, which is why it so much noisier than the other two components. [**ER**] 56

3.1 The scaled singular vectors (eq. 3.4) of the two-component input data shown in table 3.1. a) data 1. b) data 2. c) data 3. 'S1' and 'S2' indicate the 1st and 2nd singular vectors. [**NR**] 67

3.2 a) The cube of data resulting from CWT applied to a single two-component trace, comprising the time axis, the component axis and the wavelet scale axis. b) Application of SVD to a window of wavelet scales of one time slice of the data cube in (a) provides the polarization of the data within that particular wavelet scale range. Since there are two data components, there are two orthogonal polarization vectors (eq. 3.4). The red arrow shows the first polarization vector. c) SVD applied to the next wavelet scale window. d) SVD applied to the last wavelet scale window. e) The wavelet-scale (frequency) dependent polarization template. [**NR**] 69

3.3 Map view of the geometry of the Kettleman survey. Five accelerometers (marked with 'A') were positioned on the surface along the survey's inline azimuth at the end of the shot line, with a 2 meter interval. Five geophones (marked with 'G') were buried near the center of the shot line, also spaced at 2 meter intervals inline. 'R2' rotation sensors (marked with 'R') were placed on the surface in between the accelerometer positions and also in between the geophone positions. There were 241 accelerated weight drop shots, 60 vibroseis shots, 57 of the 25 m depth dynamite shots and 54 of the 50 m depth dynamite shots. [**NR**] 72

3.4 6C receiver gather of the accelerated weight-drop source, clipped at the 93rd percentile. Shot spacing was 6.25 m. Components are: (a) vertical, (b) radial, (c) transverse, (d) yaw, (e) roll, (f) pitch. Six shots were executed at each station, and then diversity stacking was applied to increase the signal to noise ratio. The data observable in these sections at this clip level consist entirely of various Rayleigh wave modes, which are not aliased due to the very close shot spacing. [**ER**] 74

3.5 6C receiver gather of the vibroseis source, clipped at the 93rd percentile. Components are: (a) vertical, (b) radial, (c) transverse, (d) yaw, (e) roll, (f) pitch. Shot spacing was 25 m, and so the various Rayleigh wave modes are aliased. Some P-wave reflections are visible at early times on the vertical component. [**ER**] 75

3.6 6C receiver gather of the 25 m depth dynamite source, clipped at the 93rd percentile. Shot spacing was 25 m. Components are: (a) vertical, (b) radial, (c) transverse, (d) yaw, (e) roll, (f) pitch. Compared to the accelerated weight drop and vibroseis surface sources, the amount of ground roll in these data is much lower, though aliasing is still very significant. Some reflections are visible at early times from offset 200 m and on. Note how the signal to noise ratio of the rotation-sensor data is low in (d), (e) and (f). [**ER**] 76

3.7 6C receiver gather of the 50 m depth dynamite source, clipped at the 93rd percentile. Shot spacing was 25 m. Components are: (a) vertical, (b) radial, (c) transverse, (d) yaw, (e) roll, (f) pitch. Reflection data are more visible in these sections vs the 25 m depth dynamite source. Note the low-frequency arrival starting from $t = 0.35$ s at offset=200 m, which appears to be shear-induced energy. Again, note the low signal to noise ratio for the rotational data in (d), (e) and (f). [**ER**] . 77

3.8 Comparison of pitch component acquired by rotation sensor and pitch calculated by differencing adjacent geophones. (a) Rotation sensor pitch for vibroseis source. (b) Geophone-differencing pitch for vibroseis source. (c) Rotation sensor pitch for 50 m depth dynamite source. (d) Geophone-differencing pitch for 50 m depth dynamite source. Note that for both source types, the signal to noise ratio of the pitch derived from geophone differencing is much higher at larger offsets than the pitch measured by the rotation sensor. AGC with a window size of $t = 0.2$ s has been applied to the data for display. [**ER**] 78

3.9 Accelerated weight drop source receiver gather at station 335. Mute has been applied to remove the body waves, and circular spreading to gain the later arrival energy. (a) Vertical accelerometer. (b) Vertical accelerometer in Radon domain. (c) Radial accelerometer. (d) Radial accelerometer in Radon domain. (e) Pitch rotation sensor. (f) Pitch rotation sensor in Radon domain. Two distinct wave modes appear on each receiver component: a slower, lower frequency mode, and a faster, higher frequency mode. Note that on the radial and pitch components, the slower surface wave mode is dominant. [**ER**] 83

3.10 Accelerated weight drop source receiver gather at station 335. Mute has been applied to remove the body waves, and circular spreading to gain the later arrival energy. (a) Transverse accelerometer. (b) Transverse accelerometer in Radon domain. (c) Yaw rotation sensor. (d) Yaw rotation sensor in Radon domain. The dispersion image of the transverse component is noisy, but two surface wave modes can still be identified, with the faster mode being dominant. On the yaw component the faster surface wave mode is clearly dominant. [**ER**] . 84

3.11 Comparison of receiver gather data components after linear moveout and AGC (left column), their correlation (center column) and their average phase difference (right column) for the slower surface wave mode. (a)-(c): Vertical (black) vs Radial (red). (d)-(f): Vertical (black) vs Pitch (blue). (g)-(i): Radial (red) vs Pitch (blue). (j)-(l): Transverse (purple) vs Yaw (green). The radial and pitch components are in phase. The vertical component lags behind the radial and pitch by 90^o. The transverse component lags behind the yaw by 90^o-180^o. [**ER**] 85

3.12 Comparison of receiver gather data components after linear moveout and AGC (left column), their correlation (center column) and their average phase difference (right column) for the faster surface wave mode. (a)-(c): Vertical (black) vs Radial (red). (d)-(f): Vertical (black) vs Pitch (blue). (g)-(i): Radial (red) vs Pitch (blue). (j)-(l): Transverse (purple) vs Yaw (green). The vertical and radial components are mostly in phase, and both lag behind the pitch by about 45^o. The transverse and yaw components are almost in phase for frequency range 21 - 26 Hz. [**ER**] 86

3.13 Data components for the slow ground roll wave mode for the trace at offset 210 m and their hodograms. (a),(e) Vertical vs Radial. (b),(f) Vertical vs Pitch. (c),(g) Radial vs Pitch. (d),(h) Transverse vs Yaw. The hodograms start from the dashed red line and progress to the solid black line. [**ER**] 87

3.14 Data components for the fast ground roll wave mode for the trace at offset 210 m and their hodograms. (a),(e) Vertical vs Radial. (b),(f) Vertical vs Pitch. (c),(g) Radial vs Pitch. (d),(h) Transverse vs Yaw. The hodograms start from the dashed red line and progress to the solid black line. [**ER**] 87

3.15 Receiver gathers of the vertical geophone component of the 4 source types in the Kettleman survey, after NMO with velocity $v = 1700$m/s. (a) Accelerated weight drop. (b) Vibroseis source. (c) Dynamite charge at 25 m depth. (d) Dynamite charge at 50 m depth. Source (a) was acquired with 6.25 m shot spacing, while (b), (c) and (d) were done with 25 m shot spacing. Observe the generally higher quality reflections acquired with the dynamite sources. The two surface sources (a) and (b) generate much more ground roll. AGC with a window size of $t = 0.2$ s has been applied to the data for display. [**ER**] 89

3.16 (g) Vertical geophone component of 50 m depth dynamite data after NMO. (a) Trace of the vertical component at offset=280 m. (b) Absolute values of the continuous wavelet transform coefficients for vertical component. (c) Trace of the radial component at offset=280 m. (d) Absolute values of the continuous wavelet transform coefficients for radial component. (e) Trace of the pitch component at offset=280 m. (f) Absolute values of the continuous wavelet transform coefficients for pitch component. AGC has been applied to (b), (d) and (f) to enable a more equalized view of the wavelet coefficients over the time and scale axes (without AGC, the units are $|\text{mm/s}|$ /scale). The wavelet scale is dyadic, beginning from a frequency of 128 Hz at wavelet scale 0 down to 0.5 Hz at wavelet scale 8. Up until $t = 0.32$ s, the data contain P reflections, while between $t = 0.32$ s and $t = 0.52$ s there is a shear-wave arrival. The lower frequency of the shear arrival can be discerned at $t = 0.4$ s, for wavelet scale=3.8. [**ER**] 92

3.17 A 3C time slice of the continuous wavelet transform of the trace at offset 280 m at $t = 0.22$ s where a P-wave reflection is visible, and the corresponding absolute values of the CWT polarization vector-set for this time slice, scaled by their respective singular values (eq. 3.4). (a) Continuous wavelet time slice. (b) 1st, (c) 2nd, and (d) 3rd polarization vectors. [**ER**] 93

3.18 A 3C time slice of the continuous wavelet transform of the trace at offset 280 m at $t = 0.42$ s where shear-wave energy dominates, and the corresponding absolute values of the CWT polarization vector-set for this time slice, scaled by their respective singular values (eq. 3.4). (a) Continuous wavelet time slice. (b) 1st, (c) 2nd, and (d) 3rd polarization vectors. Note that the 2nd polarization vectors at (c) have a wider frequency band than the 1st polarization vectors at (b), and are more similar to the 1st polarization vectors at 3.17(b), indicating that the dominant shear-wave energy in (b) is overlaying weaker P-wave reflection energy. [**ER**] 94

3.19 The set of scalar w_1 weights (eq. 3.8) applied to the first polarization vector of the data in the wavelet domain to attenuate the shear wave mode appearing at ($x = 280$m, $t = 0.4$s) in Figure 3.16(a). [**ER**] . . . 94

3.20 Receiver gather of 50 m depth dynamite source before (top row) and after (bottom row) polarization filter to attenuate the shear arrival at (t,x) = (0.4 s, 300 m). (a) Vertical component. (b) Radial component. (c) Pitch component. (d) Vertical component. (e) Radial component. (f) Pitch component. Data are shown after NMO with velocity $v = 1700$ m/s to flatten the P-wave reflections. AGC with a window size of $t = 0.2$ s has been applied for display purposes. Observe that the circled shear-induced event has been attenuated, and that the underlying P-wave reflections are visible after filtering. The filter has killed the noise and the P-wave data have survived. [**ER**] 95

3.21 A comparison of the filtering results using continuous wavelet polarization filter versus a low-cut filter on the 50 m depth dynamite receiver gather at station 335. (a) Vertical component. (b) Vertical component after application of continuous wavelet polarization filter. (c) Vertical component after application of a low-cut filter, where the pass band was 25 Hz - 60 Hz. (d) Vertical component (a) in frequency-wavenumber domain. (e) Vertical component (b) in the frequency-wavenumber domain. (f) Vertical component (c) in the frequency-wavenumber domain. AGC was applied to the data prior to FK transform. Observe how in (b) and (e), the polarization filtering does not impartially remove low frequencies, unlike the low-cut filter in (c) and (f), and therefore there is no reduction in the spectral resolution of the data. [**ER**] 96

3.22 Receiver gather of 25 m depth dynamite source before (top row) and after (bottom row) polarization filter to attenuate shear and ground roll energy. (a) Vertical component. (b) Radial component. (c) Pitch component. (d) Vertical component. (e) Radial component. (f) Pitch component. Data are shown after NMO with velocity $v = 1700$ m/s to flatten the P-wave reflections. AGC with a window size of $t = 0.2$ s has been applied for display purposes. The shear-induced energy and the spatially-aliased ground roll have been mostly attenuated, and the underlying P-wave reflections in the top circle are visible after filtering. In the top circle, we can see that the filter has killed the noise and the P-wave data have survived. [**ER**] 98

3.23 Receiver gather of vibroseis source before (top row) and after (bottom row) polarization filter to remove ground-roll energy. (a) Vertical component. (b) Radial component. (c) Pitch component. (d) Vertical component. (e) Radial component. (f) Pitch component. Data are shown after NMO with velocity $v = 1620$ m/s to flatten the P-wave reflections. AGC with a window size of $t = 0.2$ s has been applied for display purposes. The spatially aliased ground-roll energy in the bottom circle has been attenuated, though no coherent P-wave energy is visible underneath the noise. In the top circle, flat P-wave reflections are visible after filtering. [**ER**] 99

3.24 Comparison of the vertical component receiver gather before and after polarization filtering to remove ground-roll energy in the frequency wavenumber domain. (a) Vertical component before filtering. (b) Vertical component after filtering. (c) Vertical component in the F-K domain before filtering. (d) Vertical component in the F-K domain after filtering. AGC was applied prior to FK transform. Note the circled aliased energy that is removed in (d) vs (c). This energy corresponds to the ground roll indicated in the bottom circle in (a) and (b) The broadband, low-wavenumber P reflection energy is more dominant in (b). A standard frequency-wavenumber filter would have had difficulty in separating signal from noise because of the aliasing. [**ER**] 100

3.25 Illustration of the differences between designing the damping weights (eq. 3.7) in the SVD polarization space for 3 components versus 2 components. The axes represent the polarization unit vectors, while the blue arrow indicates the template polarization vector in the 3D space. The red arrow indicates the projection of the template polarization onto one of the 2D planes. (a) The conical shape of the volume in the 3D SVD space that would be damped using the angle-based similarity measure (eq. 3.6) if 3 data components were used. (b) The slice of the 2D SVD space that would be damped using the angle-based similarity measure if only 2 data components were used. (c) The projection of the damped 2D SVD space to the 3D SVD space, which is a wedge-shaped volume rather than a conical one as for 3D damping. The angular difference between two vectors in 3D is more restrictive than for 2D and will affect the similarity measure and the corresponding damping weights. To compare the polarization template matching for different data components, it is therefore necessary to always compare using the same number of components. [**NR**] 102

3.26 Comparison of polarization filtering of the shear-induced and ground roll energy in the 25 m depth dynamite receiver gathers, when using the vertical (V_z), radial (V_x) and pitch (R_y) components as inputs vs when using the vertical (V_z), radial (V_x) and transverse (V_y) components as inputs. (a) The input vertical (V_z) component. (b) The input radial (V_x) component. (c) The input transverse (V_y) component. (d) The input pitch (R_y) component. (e) Vertical component after filtering using V_z, V_x, R_y components. (f) Vertical component after filtering using V_z, V_x, V_y components. (g) Radial component after filtering using V_z, V_x, R_y components. (h) Radial component after filtering using V_z, V_x, V_y components. Data are shown after NMO with velocity $v = 1700$ m/s to flatten the P-wave reflections. AGC with a window size of $t = 0.2$ s has been applied for display purposes. Comparing (e) to (f) and (g) to (h), I observe that the shear-induced energy and particularly the spatially-aliased ground roll at $t = 0.6$ s are better attenuated when using the pitch rotational component, which contains more coherent energy of these wave modes than does the transverse component. [**ER**] 104

3.27 Comparison of polarization filtering of the slow (250 m/s) ground roll in the vibroseis receiver gathers, when using the vertical (V_z), radial (V_x) and pitch (R_y) components as inputs vs. when using the vertical (V_z), radial (V_x) and tranverse (V_y) components as inputs. (a) The input vertical (V_z) component. (b) The input radial (V_x) component. (c) The input transverse (V_y) component. (d) The input pitch (R_y) component. (e) Vertical component after filtering using V_z, V_x, R_y components. (f) Vertical component after filtering using V_z, V_x, V_y components. (g) Radial component after filtering using V_z, V_x, R_y components. (h) Radial component after filtering using V_z, V_x, V_y components. Data are shown after NMO with velocity $v = 1700$ m/s to flatten the P-wave reflections. AGC with a window size of $t = 0.2$ s has been applied for display purposes. Comparing (e) to (f) and (g) to (h), I observe that the spatially-aliased ground roll (circled) is better attenuated when using the pitch rotational component, which contains more coherent energy of the ground roll than does the transverse component. [**ER**] . 106

3.28 Comparison of polarization filtering of the shear-induced wave mode in the 50 m depth dynamite receiver gathers, when using the vertical (V_z), radial (V_x) and pitch (R_y) components as inputs vs when using the vertical (V_z), radial (V_x) and pitch (V_y) components as inputs. (a) The input vertical (V_z) component. (b) The input radial (V_x) component. (c) The input transverse (V_y) component. (d) The input pitch (R_y) component. (e) Vertical component after filtering using V_z, V_x, R_y components. (f) Vertical component after filtering using V_z, V_x, V_y components. (g) Radial component after filtering using V_z, V_x, R_y components. (h) Radial component after filtering using V_z, V_x, V_y components. Data are shown after NMO with velocity $v = 1700$ m/s to flatten the P-wave reflections. AGC with a window size of $t = 0.2$ s has been applied for display purposes. Comparing to (e) to (f) and (g) to (h), I observe that there are no significant differences between the filtering results with the pitch component vs the results using the transverse component, since the shear-induced wave mode is similarly apparent on both of these input receiver components. [**ER**] 108

4.1 Receiver gathers at station 335 for the vibroseis source. a) Vertical accelerometer component. b) Radial accelerometer component. c) Transverse accelerometer component. d) Yaw rotation-sensor component e) Roll rotation-sensor component f) Pitch component derived from differencing two adjacent inline vertical accelerometers. AGC has been applied for display. Note the various types of surface wave modes present, as annotated on (a), but are recorded on all components. The yaw and the roll rotation-sensor components have very low SNR at increasing offsets, and therefore I did not use them in the analysis presented here. [**ER**] 117

4.2 The training data at receiver station 335 for the SVM. a) Feature vectors for each time sample for the multicomponent trace at offset 180m. b) The same feature vectors color coded by their respective classification, 'Class 1' being the slow ground roll mode and 'Class 0' representing everything else. Note the differences between the feature vectors of each class. These feature vectors and their respective labels indicating the wave mode are the input to the SVM training. [**ER**] . 119

4.3 SVM training data at station 335, and testing results on the same training data, for the vibroseis source. Only the vertical component is shown, although the training data comprised the vertical, radial and pitch components. a) Slow ground roll mode training data. b) Fast ground roll mode training data. c) Slow+fast ground roll modes training data. d) Testing classification of slow ground roll mode on training data. e) Testing classification of fast ground roll mode on training data. f) Testing classification of slow+fast ground roll modes on training data. [**ER**] 120

4.4 SVM classification of surface wave modes on test data at station 336, for the vibroseis source. Only the vertical component receiver gather is shown, although the training and test data comprised the vertical, radial and pitch components. g): Input vertical component at station 336. a): classification of slow ground roll mode. b): Complementary data to (a) (i.e., (g) - (a)). c): classification of fast ground roll mode. d): Complementary data to (c) (i.e., (g) - (c)). e): classification of slow+fast ground roll. f): Complementary data to (e) (i.e., (g) - (e)). [**ER**] 122

4.5 SVM classification of surface wave modes on test data at station 337, for the vibroseis source. Only the vertical component receiver gather is shown, although the training and test data comprised the vertical, radial and pitch components. g): Input vertical component at station 337. a): classification of slow ground roll mode. b): Complementary data to (a) (i.e., (g) - (a)). c): classification of fast ground roll mode. d): Complementary data to (c) (i.e., (g) - (c)). e): classification of slow+fast ground roll. f): Complementary data to (e) (i.e., (g) - (e)). [**ER**] 123

4.6 SVM classification of surface wave modes on test data at station 191, for the vibroseis source. Only the vertical component receiver gather is shown, although the training and test data comprised the vertical, radial and pitch components. g): Input vertical component at station 191. a): classification of slow ground roll mode. b): Complementary data to (a) (i.e., (g) - (a)). c): classification of fast ground roll mode. d): Complementary data to (c) (i.e., (g) - (c)). e): classification of slow+fast ground roll. f): Complementary data to (e) (i.e., (g) - (e)). [**ER**] 124

4.7 SVM classification of surface wave modes at station 335, for different seismic source types. Only the vertical is shown, although the training and test data comprised the vertical, radial and pitch. a) Vertical of vibroseis source. b) The portion slow+fast ground roll mode labeled as class 1 from the vibroseis source data used to train the SVM. c) The complementary data containing body waves labeled as class 0 from the vibroseis source data used to train the SVM. d) Vertical of accelerated weight-drop source. e) classification of slow+fast ground roll mode for the accelerated weight-drop source using the SVM trained on the vibroseis data. f) classification of the complementary data for the accelerated weight-drop source using the SVM trained on the vibroseis data. g) Vertical of dynamite source. h) classification of slow+fast ground roll mode for the dynamite source using the SVM trained on the vibroseis data. i) classification of the complementary data for the dynamite source using the SVM trained on the vibroseis data. [**ER**] . 126

4.8 The input training feature vectors at training station 335 for trace at offset 180m, for a varying number of components used in the training. The classification is color-coded. The slow ground roll mode is 'Class 1' (red) and everything else is 'Class 0' (blue). a) Vertical and radial components. b) Vertical, radial and transverse components. c) Vertical, radial, transverse and pitch components. The more components used, the longer is the feature vector, and more differences can be discerned between the feature vectors of the two wave modes. [**ER**] 128

4.9 SVM classification of surface wave modes at testing station 191, for a varying number of receiver components used in training the SVM at station 335. a) Classification of slow+fast ground roll using vertical, radial, transverse and pitch components; b) using vertical, radial and transverse components; c) using only vertical and radial components. d,e,f) The complementary data to (a), (b) and (c), which are classified as body waves. For this receiver gather, adding more components in the SVM training improves the classification of the surface waves vs the P waves. [**ER**] 129

4.10 SVM classification of slow vs fast ground roll modes at testing station 336, for different components used in training the SVM at station 335. a) Classification of slow ground roll using vertical, radial and pitch components; b) using vertical, radial and transverse components. c) Classification of fast ground roll using vertical, radial and pitch components; d) using only vertical and radial and transverse components. For this receiver gather, the SVM does a better job differentiating between the slow and fast ground roll modes when using the transverse component rather than the pitch. [**ER**] 131

4.11 SVM classification of slow vs fast ground roll modes at testing station 191, for different components used in training the SVM at station 335. a) Classification of slow ground roll using vertical, radial and pitch components; b) using vertical, radial and transverse components. c) Classification of fast ground roll using vertical, radial and pitch components; d) using only vertical and radial and transverse components. For this receiver gather, the SVM does a better job differentiating between the slow and fast ground roll modes when using the transverse component rather than the pitch. [**ER**] 132

Chapter 1

Introduction

Rotational motions in seismology are not a familiar subject to most readers from the seismological research community, therefore I will first introduce the concepts and the nomenclatures I intend to use throughout the dissertation. I discuss the acquisition of rotations and translations in fields other than seismology. I provide a review of continuum mechanics concepts, and show how rotational motion is related to the seismic wavefield. I then review some existing applications for data comprising both translational and rotational seismic motion.

SEISMIC ROTATIONAL DATA

Rigid bodies in a three dimensional world have six degrees of freedom: three components of translation and three components of rotation. In seismic acquisition, the time derivatives of translations, i.e. the particle velocities, are commonly recorded by three-component geophones. The rotations, which are not recorded in current industrial seismic acquisition, are termed pitch, roll and yaw, as shown in the following table:

Axis	Particle velocity		Rotation rate	
Z	Vertical	v_z	Yaw	r_z
X	Radial	v_x	Roll	r_x
Y	Transverse	v_y	Pitch	r_y

where v_i are particle velocities along the i axis, and r_i are rotation rates around the i axis.

Two examples that show a recording six degrees of freedom of motion come from avionics and from biology. On an aircraft (Figure 1.1), an onboard inertial navigation system measures both linear motion using accelerometers, and rotations by a gyroscope. These measurements are calibrated with ground based telemetry such as GPS or radar stations to account for instrument drift. A pilot would find it difficult to control a plane without the six-component data these instruments provide.

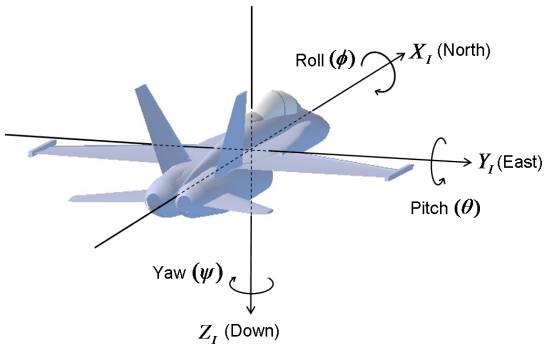

Figure 1.1: Sketch of the six degrees of freedom of a rigid body in a 3D world. To know what an aircraft is doing, it is not sufficient to know its linear velocity but also its rotations. There are three components to the velocity, and in addition there are three components to the rotation: roll, pitch, and yaw. [**NR**] chap1/. jetrotations

In the human body, linear motions and rotations are measured in the inner ear. Figure 1.2 shows the structure of a human ear. Two elements in the ear called the saccule and utricle detect linear acceleration. The three semicircular ducts labels "Anterior", "Lateral" and "Posterior" in the figure record rotations. They contain a fluid, and under the inertia caused by rotational motion, this fluid moves in relation to the solid structure of the ducts. The relative motion of the fluid is felt by hair cells lining the canal, which convert the motion to small electrical signals that are transmitted via the nervous system to the brain. Additionally, the cochlea records pressure changes, which is how we hear. The human ear is in effect a seven-component sensor, and we would find it tricky to orient ourselves in a 3D world without the component inputs from this sensor.

To show where rotations enter into the field of seismology, the next section will review some concepts of continuum mechanics.

Elastic continuum theory review

The analysis presented here follows standard fundamental concepts in continuum mechanics.

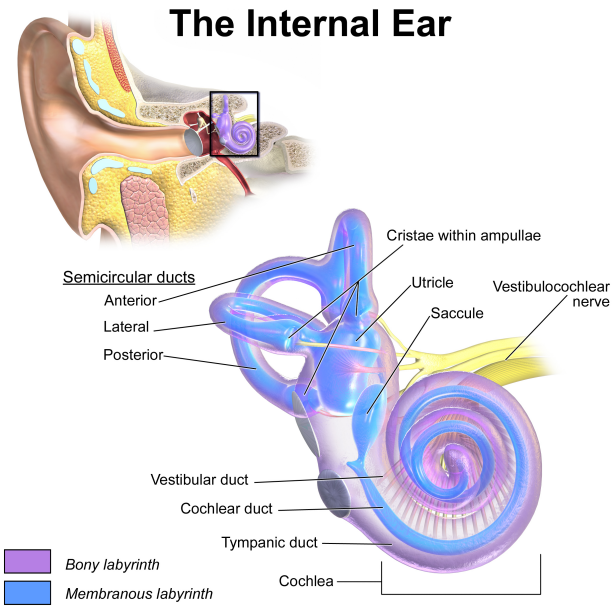

Figure 1.2: The inner ear, the human multicomponent recorder. Utricle and saccule detect linear acceleration, while the semicircular canals detect rotations. Cochlea detects pressure changes. (Blausen, 2014). [**NR**] chap1/. human-ear

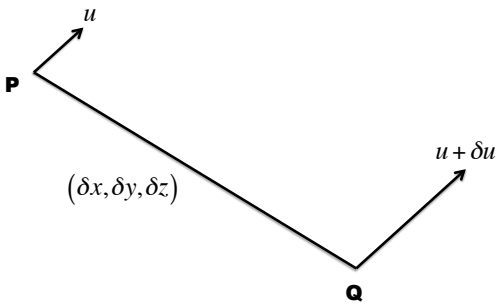

Figure 1.3: Two points, P and Q, are separated by $\delta\mathbf{x} = (\delta x, \delta y, \delta z)$. P is displaced by $\mathbf{u}$, and Q is displaced by $\mathbf{u} + \delta\mathbf{u}$. [**NR**] chap1/. displacement-gradient

A single point in space has no orientation. The cartesian coordinates x, y, z are sufficient to specify its position and motion. Consider that we have two nearby points in space P and Q, separated by $(\delta x, \delta y, \delta z)$, as shown in Figure 1.3. The displacement of point P is given by the vector $\mathbf{u}$. P and Q are considered close enough that the relative displacement $\delta\mathbf{u}$ between these two points can be given to a first order by the displacement-gradient tensor $\mathbf{L}$:

$$\begin{pmatrix} \delta u_x \\ \delta u_y \\ \delta u_z \end{pmatrix} = \mathbf{L} \begin{pmatrix} \delta x \\ \delta y \\ \delta z \end{pmatrix} = \begin{pmatrix} \frac{\partial u_x}{\partial x} & \frac{\partial u_x}{\partial y} & \frac{\partial u_x}{\partial z} \\ \frac{\partial u_y}{\partial x} & \frac{\partial u_y}{\partial y} & \frac{\partial u_y}{\partial z} \\ \frac{\partial u_z}{\partial x} & \frac{\partial u_z}{\partial y} & \frac{\partial u_z}{\partial z} \end{pmatrix} \begin{pmatrix} \delta x \\ \delta y \\ \delta z \end{pmatrix}. \tag{1.1}$$

The rank 2 tensor $\mathbf{L}$ is represented by a square matrix. Any square matrix can be decomposed into a symmetric and an anti-symmetric part as:

$$\mathbf{L} = \frac{1}{2}\left(\mathbf{L} + \mathbf{L}^T\right) + \frac{1}{2}\left(\mathbf{L} - \mathbf{L}^T\right). \tag{1.2}$$

For the displacement-gradient tensor $\mathbf{L}$, the symmetric part is the Cauchy infinitesimal strain tensor ε

$$\varepsilon = \begin{pmatrix} \epsilon_{xx} & \epsilon_{xy} & \epsilon_{xz} \\ \epsilon_{yx} & \epsilon_{yy} & \epsilon_{yz} \\ \epsilon_{zx} & \epsilon_{zy} & \epsilon_{zz} \end{pmatrix} = \begin{pmatrix} \frac{\partial u_x}{\partial x} & \frac{1}{2}\left(\frac{\partial u_x}{\partial y} + \frac{\partial u_y}{\partial x}\right) & \frac{1}{2}\left(\frac{\partial u_x}{\partial z} + \frac{\partial u_z}{\partial x}\right) \\ \frac{1}{2}\left(\frac{\partial u_y}{\partial x} + \frac{\partial u_x}{\partial y}\right) & \frac{\partial u_y}{\partial y} & \frac{1}{2}\left(\frac{\partial u_y}{\partial z} + \frac{\partial u_z}{\partial y}\right) \\ \frac{1}{2}\left(\frac{\partial u_z}{\partial x} + \frac{\partial u_x}{\partial z}\right) & \left(\frac{\partial u_z}{\partial y} + \frac{\partial u_y}{\partial z}\right) & \frac{\partial u_z}{\partial z} \end{pmatrix}, \tag{1.3}$$

while the anti-symmetric part is the infinitesimal rotation tensor $\mathbf{\Omega}$

$$\mathbf{\Omega} = \begin{pmatrix} 0 & -\frac{1}{2}\left(\frac{\partial u_y}{\partial x} - \frac{\partial u_x}{\partial y}\right) & \frac{1}{2}\left(\frac{\partial u_x}{\partial z} - \frac{\partial u_z}{\partial x}\right) \\ \frac{1}{2}\left(\frac{\partial u_y}{\partial x} - \frac{\partial u_x}{\partial y}\right) & 0 & -\frac{1}{2}\left(\frac{\partial u_z}{\partial y} - \frac{\partial u_y}{\partial z}\right) \\ -\frac{1}{2}\left(\frac{\partial u_x}{\partial z} - \frac{\partial u_z}{\partial x}\right) & \frac{1}{2}\left(\frac{\partial u_z}{\partial y} - \frac{\partial u_y}{\partial z}\right) & 0 \end{pmatrix}. \tag{1.4}$$

We can also define an infinitesimal rotation vector $\mathbf{R}$, which is 1/2 of the curl of

the displacement vector $\mathbf{u}$:

$$\mathbf{R} = \begin{pmatrix} R_x \\ R_y \\ R_z \end{pmatrix} = \frac{1}{2}\nabla \times \mathbf{u} = \begin{pmatrix} 0 & -\partial_z & \partial_y \\ \partial_z & 0 & -\partial_x \\ -\partial_y & \partial_x & 0 \end{pmatrix} \begin{pmatrix} u_x \\ u_y \\ u_z \end{pmatrix} = \begin{pmatrix} \frac{1}{2}\left(\frac{\partial u_z}{\partial y} - \frac{\partial u_y}{\partial z}\right) \\ \frac{1}{2}\left(\frac{\partial u_x}{\partial z} - \frac{\partial u_z}{\partial x}\right) \\ \frac{1}{2}\left(\frac{\partial u_y}{\partial x} - \frac{\partial u_x}{\partial y}\right) \end{pmatrix}. \quad (1.5)$$

While the displacement vector $\mathbf{u}$ represents linear motion of a point, the rotation vector represents the rotation of a volume element. The components of the rotation vector $\mathbf{R}$ are measureable in the field, and contain the elements of the anti-symmetric strain tensor $\mathbf{\Omega}$.

Examples of strains

To relate measurements of rotation to seismic data, let us look at several simple variants of medium strain, as shown in Pujol (2003). In the following notation, α is the amount of (infinitesimal) deformation, X_i are the dimensions of the element and $\hat{e}_i$ are unit vectors.

Dilatational strain

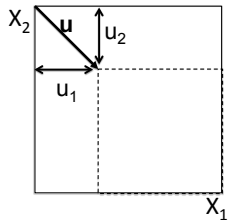

Figure 1.4: Dilatational strain field, which generates a fractional volume change but no rotation. [**NR**] chap1/. strain0

Dilational strain is shown in Figure 1.4. The displacement vector for this strain is

$$\mathbf{u} = (1-\alpha)X_1\hat{e}_1 + (1-\alpha)X_2\hat{e}_2 + (1-\alpha)X_3\hat{e}_3. \quad (1.6)$$

Applying the rotation tensor (1.4) to this displacement, we see that dilatational strain has no rotation:

$$\omega_{ij} = \frac{1}{2}\left(u_{i,j} - u_{j,i}\right) = 0. \quad (1.7)$$

The symmetric strain tensor is

$$\epsilon_{ij} = \frac{1}{2}\left(u_{i,j} + u_{j,i}\right) = \frac{(1-\alpha)}{2}\left(X_{i,j} + X_{j,i}\right) = \frac{(1-\alpha)}{2}\left(\delta_{i,j} + \delta_{j,i}\right) = (1-\alpha)\delta_{i,j}, \quad (1.8)$$

or more explicily,

$$\varepsilon = \begin{pmatrix} 1-\alpha & 0 & 0 \\ 0 & 1-\alpha & 0 \\ 0 & 0 & 1-\alpha \end{pmatrix}. \quad (1.9)$$

The dilatational strain results in a fractional volume change (isotropic compression), given by the divergence of displacements:

$$\nabla \cdot \mathbf{u} = u_{i,i} = 3(1-\alpha). \quad (1.10)$$

Simple shear strain

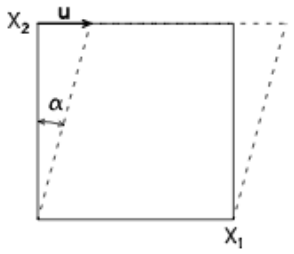

Figure 1.5: Simple shear strain field, which generates rotation but no volume change. Figure from Pujol (2003). [**NR**] chap1/. strain1

As opposed to dilatational strains, shear strains result in no net change of volume, but rather in the shape of an element. Simple shear strain is shown in Figure 1.5. The displacement vector for simple shear strain is

$$\mathbf{u} = \alpha X_2 \hat{e}_1, \quad (1.11)$$

and the symmetric strain and rotational tensors are

$$\varepsilon = \begin{pmatrix} 0 & \alpha/2 & 0 \\ \alpha/2 & 0 & 0 \\ 0 & 0 & 0 \end{pmatrix}; \quad \mathbf{\Omega} = \begin{pmatrix} 0 & \alpha/2 & 0 \\ -\alpha/2 & 0 & 0 \\ 0 & 0 & 0 \end{pmatrix}. \tag{1.12}$$

Simple shear generates rotations, but no change in volume.

Pure shear strain I

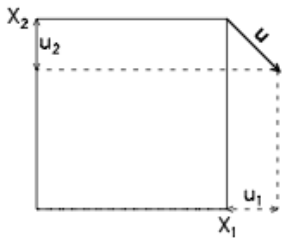

Figure 1.6: Pure shear type I strain field, which generates no rotation and no volume change. Figure from Pujol (2003). [**NR**] chap1/. strain2

Pure shear strain type I is shown in Figure 1.6. The displacement vector for this shear strain is

$$\mathbf{u} = \alpha(X_1\hat{e}_1 - X_2\hat{e}_2), \tag{1.13}$$

and the symmetric strain and rotational tensors are

$$\varepsilon = \begin{pmatrix} \alpha & 0 & 0 \\ 0 & -\alpha & 0 \\ 0 & 0 & 0 \end{pmatrix}; \quad \omega_{ij} = 0. \tag{1.14}$$

Pure shear strain II

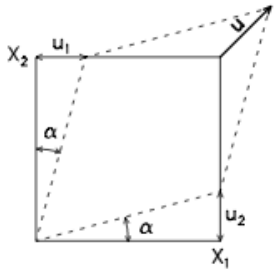

Figure 1.7: Pure shear type II strain field, which generates no rotation and no volume change. Figure from Pujol (2003). [**NR**] chap1/. strain3

Pure shear strain type II is shown in Figure 1.7. The displacement vector for this shear strain is

$$\mathbf{u} = \alpha(X_2\hat{e}_1 + X_1\hat{e}_2), \tag{1.15}$$

and the symmetric strain and rotational tensors are

$$\varepsilon = \begin{pmatrix} 0 & \alpha & 0 \\ \alpha & 0 & 0 \\ 0 & 0 & 0 \end{pmatrix}; \quad \omega_{ij} = 0. \tag{1.16}$$

Unlike simple shear strains that generate rotations, both types of pure shear strains do not generate rotations nor changes in volume.

Pure rotational strain

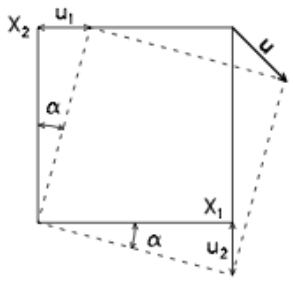

Figure 1.8: Pure rotation strain field, which generates no volume change. Figure from Pujol (2003). [**NR**] chap1/. strain4

A pure rotational strain does not change the shape or the volume of an element, only its orientation. Pure rotational strain is shown in Figure 1.8. The displacement vector for this shear strain is

$$\mathbf{u} = \alpha(X_2\hat{e}_1 - X_1\hat{e}_2). \tag{1.17}$$

and the symmetric strain and rotational tensors are

$$\epsilon_{ij} = 0; \quad \mathbf{\Omega} = \begin{pmatrix} 0 & \alpha & 0 \\ -\alpha & 0 & 0 \\ 0 & 0 & 0 \end{pmatrix}. \tag{1.18}$$

Recording of strains vs recording of translations

Hooke's law of linear elasticity states that the stress σ_{ij} and symmetric strain ϵ_{ij} tensors are related by the fourth-order stiffness tensor C_{ijkl} as

$$\sigma_{ij} = -C_{ijkl}\epsilon_{kl}, \tag{1.19}$$

where, as in the Einstein notation, the repeating indices indicate an implicit summation over the spatial dimensions. In land and in ocean-bottom seismic acquisition, the particle velocities $\vec{v}$ (the time derivatives of translations/displacements) resulting from seismic energy propagating in the Earth are recorded by three-component geophones coupled to the ground. Additionally, in both ocean-bottom node (OBN) and marine streamer acquisition, a hydrophone coupled to the water records deviations in pressure resulting from seismic energy propagating in the water column.

According to Hooke's law, in an isotropic elastic medium, normal stress is proportional to the divergence of particle translations, i.e., the dilatational medium strain:

$$\sigma_{ii} = \left(\kappa + \frac{4}{3}\mu\right)\partial_i u_i, \tag{1.20}$$

where κ and μ are the bulk and shear moduli of the medium.

In an acoustic medium such as water the shear modulus is zero, and the summation of normal stresses is termed pressure, which equals the trace of the stress tensor:

$$P = \kappa\partial_i u_i = \kappa\nabla\cdot\vec{u}. \tag{1.21}$$

A hydrophone effectively measures the pressure variations in equation 1.21 caused by the passage of a P-wave in water. If we knew the particle translations everywhere within a given volume, then we could calculate the pressure value by applying the spatial derivatives shown in equation 1.21 to the recorded translational data. However, receiver stations are usually too sparse in relation to the acquired wavelengths to calculate the spatial divergence of translations, and in any case are commonly spread along a single surface (the sea bottom, or land surface).

The value of the divergence is not redundant even if we measure the three components of translation, since it can be used to ascertain the vertical propagation direction of the waves incident on the sea bottom (Barr and Sanders, 1989). The pressure that the hydrophone records is proportional to the divergence of the particle translations, and is therefore used in upgoing/downgoing wavefield separation of OBN data.

Furthermore, we must remember that the definitions of seismic waves come not from their translations, but from the medium strains they generate. Figure 1.9(a) shows the strains generated by a P-wave propagating through an unbounded, homogeneous medium. Note the dilatational strain (eq. 1.9) it applies to the medium. The particle translations themselves are parallel to the propagation direction.

The propagating shear wave in Figure 1.9(b) generates simple shear strains. The particle translations are perpendicular to the propagation direction of the shear wave. However, because the P-wave and the shear wave are propagating in perpendicular directions, the particle translations are identical, even though the strains are different. A three-component geophone would record the same signal for both of these waves.

A rotation sensor would measure the rotation vector $\mathbf{R}$, i.e. the curl of the translational wavefield (1.5), which contains the elements of the anti-symmetric rotation tensor (1.4). Since a simple shear strain comprises rotational strains (1.12), a rotation sensor in a homogeneous medium would record the passage of the shear wave, but not of the rotation-free P wave.

Similarly, a pressure sensor (i.e., a hydrophone) would record the passage only of the P wave, because, unlike the shear wave, it generates dilatational strains.

The situation is more complicated on a medium interface, where surface waves may occur. For example, the strains generated by the passage of a Rayleigh wave in Figure 1.10(a) are some combination of both horizontal-rotational and dilatational strains. Love waves (Figure 1.10(b)) generate shear and vertical rotational strains. Additionally, at a medium interface mode conversions from P to S may occur. The converted shear mode, combined with the incident and reflected P wave, can combine to form both dilatational and rotational strains at the interface. This is particularly relevant in seismic acquisition, since seismic data are always, invariably, recorded on a medium interface, i.e. the free surface, either on land or on the ocean bottom.

Since strains are spatial derivatives of translations, we may conclude that geophones do not record strains, as they measure medium translations and not the spatial derivatives of those translations. This is the fundamental difference between what geophones measure as compared to what hydrophones and rotation sensors measure. In other words, just as we may not expect to record the dilatational medium strain (1.9) with a three-component geophone, we similarly cannot expect to record the rotational medium strains (1.18,1.12) using a three-component geophone.

Theoretically, if all three components the particle translation wavefield were well sampled in all directions, then we would be able to calculate all medium strains explicitly by summing or differencing the translational components. In practice, however, this would severely increase the expense of seismic acquisition, especially considering vertical sampling which would entail the digging of boreholes at each receiver position. Additionally, the differences in coupling between sensors would need to be taken into account. Therefore, in order to fully capture the complexity of the elastodynamic seismic wavefield at the point of measurement, in addition to geophones we require sensors that can, by design, record medium strains.

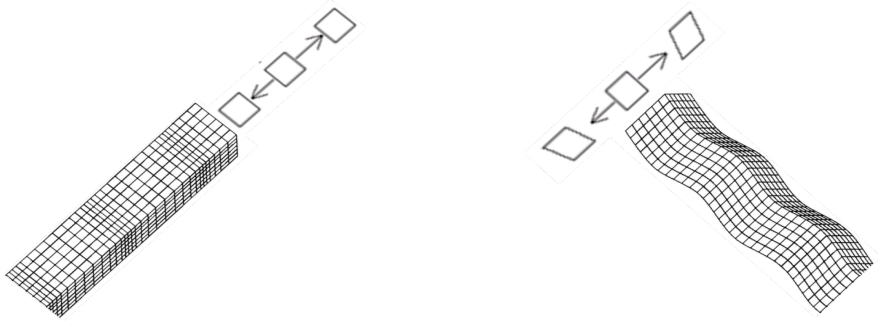

(a) (b)

Figure 1.9: The medium strains generated by the passage of seismic body waves in an unbounded homogeneous medium. (a) A plane P wave, which generates a dilatational strain. (b) A plane shear wave, which generates a simple shear strain. As a result of their perpendicular propagation directions, the translations of these two waves are identical, even though the strains are different. [**NR**] chap1/. P-wave-deform,S-wave-deform

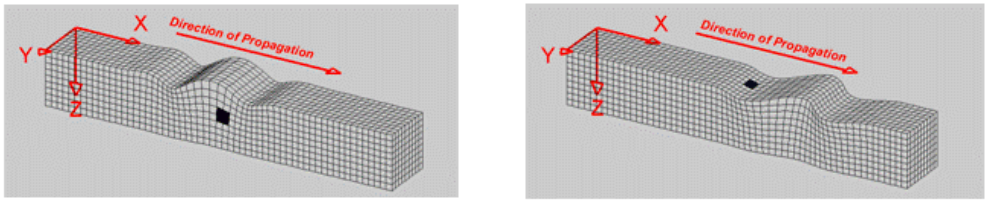

(a) (b)

Figure 1.10: The medium strains generated by the passage of seismic surface waves in a laterally homogeneous medium. (a) A Rayleigh wave, which generates a combination of dilatational and rotational strains. (b) A Love wave, which generates shear and rotational strains. (http://web.ics.purdue.edu/braile/edumod/waves/WaveDemo.htm) [**NR**] chap1/. Rayleigh-wave-deform,Love-wave-deform

Visualization of six components of motion

The standard method of observing seismic trace gathers is to look at either wiggle plots or color plots (usually greyscale) where the axes are time and some spatial axis such as offset. For multicomponent data, it is customary to observe each component in a separate gather. I found that this method is not useful for instructing the viewer in the actual motion that is occuring as a result of the passage of seismic waves, especially if I want to show rotations together with translations.

Robert Brune had the idea of using the BMW corporation symbol to represent the two translational and one rotational degrees of freedom for 2D data. I extended this idea to 3D using a visualization tool called a "seisball". An example of the seisball display is shown in Figure 1.11. The seisball represents the motion of the ground at the receiver position, over time. In Figure 1.11, each ball is a time sample of a trace from the Kettleman six-component dataset (described in chapter 3). The left and right displacement of the ball represents the radial geophone component, while the change in size represents the transverse geophone component. The vertical motion of the ball is represented by vertical displacement, which in this display is also coincident with the vertical temporal axis. The 3D rotations are represented by the seisball's rotations.

Both of the traces shown in Figure 1.11 are from the same receiver position. However, the left trace shows only the translational data as measured by the geophones,

while the right trace shows both the translations and rotations as measured by rotation sensors. What is striking in this display is the amount of ground motion not being recorded by current seismic acquisition.

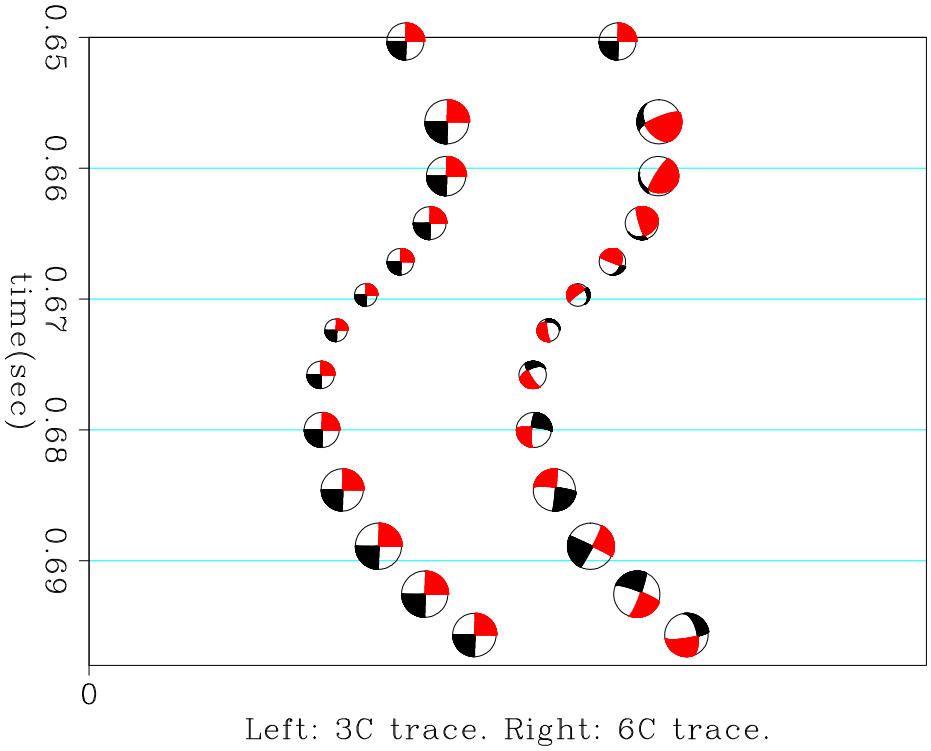

Figure 1.11: Comparison of the seisball visualization for a three-component data trace representing only translational components (left) vs the same data trace but with six-components representing both translational and rotational components (right). The data are from the Kettleman six-component survey (described in chapter 3), where both translations and rotations were recorded. Note how much richer in ground motion information the 6C data are. Current seismic acquisition only records 3C data like the trace on the left. [**ER**] chap1/. VibNomad65-st335-sb-tr

Current applications for seismic rotational data

Most of the research that has been done on seismic rotations was by the earthquake seismology and earthquake engineering communities. There is interest even in the field of gravity-wave measurements, where seismic rotations are effectively noise (Lantz et al., 2009).

Lee et al. (2009) provide some historical background for the study of rotational seismology, and introduce some of the fields of study to which seismic rotations are

relevant. Theoretical seismologists like Aki and Richards (2002) have argued that rotations should be recorded in addition to translations in order to completely describe ground motion. Huang (2003) reports observations of significant ground rotations induced by the 1999 Chi-Chi earthquake in Taiwan.

Of particular importance for the earthquake seismology community is the fact that the seismometers themselves are sensitive to rotations, which is why integration of earthquake accelerometer records may result in an apparent total translation. Trifunac and Todorovska (2001), Grazier (2005) and Pillet and Virieux (2007) discuss the effect of seismic rotations on linear accelerometer recordings for the case of strong motion in the near field of earthquakes. They conclude that a direct recording of rotations is required in order to correct accelerometer measurements for tilt-induced gravitational effects and centrifugal acceleration generated by the seismic rotations, which effectively cause the accelerometer components to lose their vector fidelity.

Lin et al. (2010) carried out a lab experiment, where a six-degree-of-freedom robotic arm generated controlled strong motion on a plate to which both accelerometers and rotation sensors were attached. They show how to dynamically correct the accelerometer records for the rotation-induced effects. The claim is that similar corrections may be required for accelerometers measuring the near-field of earthquakes.

Another interesting application for rotational data is direct shear-wave speed determination. Let $\mathbf{u}(\mathbf{x}^r, t)$ denote a displacement field recorded at receiver position $\mathbf{x} = \mathbf{x}^r$. If the wave being recorded is a plane shear wave in a homogeneous, isotropic medium, then we have:

$$\frac{1}{2}\frac{|\dot{\mathbf{u}}(\mathbf{x}^r)|}{|\mathbf{R}(\mathbf{x}^r)|} = V_s, \tag{1.22}$$

where $\mathbf{R}(\mathbf{x}^r)$ is the rotation at the same receiver position $\mathbf{x} = \mathbf{x}^r$ and V_s is shear-wave velocity. This relation implies that information on subsurface velocity structure (otherwise only accessible through seismic array measurements and combined analyses) is contained in a single point measurement. Igel et al. (a) and Igel et al. (b) report on this very useful application for directly measuring shear-wave velocity and also the back-azimuth of shear arrivals using just one six-component point sensor. Aldridge and Abbott (2009) also demonstrate this concept, calling it "the point seismic array", which offers the intriguing possibility of dispensing with conventional spatially-extended receiver arrays designed to record similar observables. Fichtner

and Igel (2009) derive sensitivity densities for the shear-wave velocity calculated by dividing the particle velocity by the rotations, and show that the shear-wave velocity so derived is relevant only to the near surface in the vicinity of the receiver. A direct measurement of shear phase velocity may therefore be used as a constraint for elastic near-surface tomography.

In earthquake engineering, the traditional approach to testing structure respones is to represent simplified strong earthquake motions, usually only the horizontal translational components of acceleration. Rotational excitation of the torsional (vertical rotation) and rocking components (horizontal rotations) are never considered, due to a lack of such data. Trifunac (2006) discusses structural responses to ground rotations. Using synthetic seismic modeling, he compares the response of structures to translational-only vs translational and rotational ground motions. Analysis of building responses to strong ground rotations may have considerable implications for current building codes.

In the field of exploration seismology, very few studies have been done on seismic rotations, owing mostly to the lack of field data. However, more than 30 years ago Cowles (1984) registered a patent that describes a "Rotational geophone" designed to record seismic rotations.

Aldridge et al. (2007) compare the AVO of rotational data resulting from modeling with a full poroelastic equations vs an "equivalent elastic medium". They note that for the rotational components, which in their simulation contains the shear-wave arrival, there is a discernable difference in the AVO behavior of the full poroelastic medium as compared to the equivalent poroelastic approximation.

Brune et al. (2012) discuss the various uses of translational and rotational data for exploration seismology, including shear-wave selectivity for microseismic applications, and the doubling of the spatial Nyquist frequency for the vertical geophone component. On a free surface, the horizontal rotational component effectively records the spatial gradient of the vertical particle displacement field. The spatial Nyquist frequency can be increased by combining the vertical displacement gradient measured by rotation sensors with the vertical displacement measured by geophones.

Muyzert et al. (2012) demonstrated how the gradient of vertical displacement measured by rotational components can be used to interpolate vertical geophone field

data, and thus mitigated the effect of spatial aliasing of high-wavenumber arrivals in their land data. This is similar to the concept shown in Vassallo et al. (2012), where hydrophone and accelerometer data were combined in marine streamer acquisition to interpolate the pressure wavefield in the crossline direction between streamer cables.

Along similar lines, Yuanyuan and Holt (2015) use the gradient of vertical displacement calculated by differencing geophone pairs to carry out wavefield gradiometry on U.S. array data. The gradiometry enables an estimation of phase velocity in the medium and the back-azimuth of arrivals.

Edme et al. (2014) treat rotational data as a noise model for ground-roll, and use adaptive subtraction in order to remove ground roll from the vertical component of geophone land data. Li and van der Baan (2015) show how to enhance microseismic event localization derived from picked P- and S-wave arrivals in borehole data using both the translational and rotational wavefield.

THESIS OVERVIEW

The goal of this thesis is to describe how rotational seismic field data may be acquired, and how the addition of rotational data components to the current set of acquired components in the exploration seismology industry will aid in the processing of seismic data. The remainder of this thesis is organized as follows:

Rotational data acquisition methods

In Chapter 2, I describe the various technologies currently available for measuring rotations. I show a new method for acquiring rotational data using induction-coil magnetometers. Induction-coil magnetometers generate current when they are rotated within the Earth's magnetic field, and the current is proportional to the amount of rotation. I show how to obtain seismic rotations from the small magnetic deviations recorded by these magnetometers. To validate the method, we performed a seismic survey where both magnetometers and inertial rotation sensors were used to record waves generated by an active source. The results indicate that seismic rotations can be derived from induction-coil magnetometers if the ambient magnetic noise level is low and if the rotation axis is not coincident with the Earth's ambient magnetic field's

direction.

Field data application I: wave mode separation

In Chapter 3, I show how to combine translational data from geophones and rotational data from rotation sensors to identify and separate particular wave modes in a 6C field dataset. I develop a polarization filter in the continuous wavelet domain in order to identify and subsequently attenuate shear and surface wave modes. Since the method operates on a trace by trace basis, it is not sensitive to spatial aliasing issues.

Field data application II: machine learning for wave mode identification

In Chapter 4, I use a machine learning algorithm to identify wave modes on combined translational and rotational field data. I derive feature vectors for the data, and train a Support Vector Machine to identify features of a particular wave mode. Just like the previous chapter, the method is immune to spatial aliasing.

Chapter 2

Seismic rotations from induction-coil magnetometers

Most of the current rotational sensing technology is not targeted toward recording seismic rotations. There is a limited number of instruments that were designed for rotational seismology, and the technology for building them is yet in an immature state. There is no industrial producer of rotation sensors. In this chapter I will review some of the rotational acquisition technologies, and propose a new method of recording rotations using an existing technology that has been employed in large exploration surveys: induction-coil magnetometers.

INSTRUMENTS CAPABLE OF RECORDING SEISMIC ROTATIONS

If we consider the type of sensors required by the exploration seismology industry for recording any observable related to seismic waves, there are several characteristics that are necessary:

1. Durability: The sensor must operate in a variety of temperatures, pressures, and moisture environments.

2. Reliability: The sensor response must be consistent over time, and not be affected by the environment.

3. Sensitivity: The noise floor of the sensor must be lower than the signal amplitude we are attempting to record.

4. Dynamic range: The sensor should be able to record the range of amplitudes that may be present in the signal.

5. Power consumption: Ideally, we would like the sensor to use as little power as possible, particularly in the ocean-bottom node scenario, where the sensor relies on a finite battery for its power.

6. Availability/economy: Current seismic acquisition utilizes thousands of receivers. A desirable sensor will have the characteristics listed above, and yet be cheap enough to manufacture in large quantities so as to make it a viable solution for large surveys.

Admittedly, this is probably only a partial list of requirements.

The existing rotational acquisition technology comprises a range of instruments, each with its particular operating principle, sensitivity, and power requirements. By and large, current rotational acquisition technology was never intended by design to record seismic rotations. Rather, it is the recent interest in seismic rotations as a new field of research that is spurring adaptations in the design of existing sensors to record these (very weak) rotations.

However, there is a principal problem related to recording of rotations: The larger the sensor is, the higher its sensitivity, but the lower is its applicability for exploration seismic acquisition.

In the Kettleman six-component land dataset which will be presented in Chapter 3, the strongest rotational signals observed in the near-field of a vibroseis source were on the order of 10^0 rad/sec. At rotation-rate values of 10^{-4} rad/sec, the signal was no longer visible above the noise. This was not a result of the lack of signal, since the translational geophones were recording signal where the rotation sensors were not, but rather a limitation of the rotation-sensing instruments being used in the survey.

Judging by the experience I've had with recording rotational data, I would say that a rotation sensor would need to record from a few rad/sec down to 10^{-6} rad/sec to be relevant for exploration seismology. Therefore, a useful rotational sensor must have a dynamic range of 120 dB.

Ring-laser Gyroscope

Ring laser gyroscopes operate by measuring the Sagnac effect: a slight change in phase and beat frequencies of two beams of light traveling in an enclosed loop in opposite directions. In a ring-laser gyroscope, as shown in Figure 2.1(b), two counter-propagating light beams are shot in opposite directions. The ring laser is coupled to the ground. When a ground rotation perpendicular to the plane of the ring laser occurs (i.e., around the vertical axis), The path length each light beam traverses changes, and the Sagnac effect is measured by the ring-laser instrument.

Ring lasers were originally designed for measuring physical quantities relevant to field of geodesy, such as minute rotations resulting from variations in the rotation rate of the Earth. They can record rotations down to 10^{-13} rad/sec. Rotations resulting from ambient seismic waves are considered to be noise by the researchers that use ring lasers. However, it was recording of earthquakes by the ring-laser gyroscope in Wettzell, Germany (Schreiber et al., 2006), that sparked recent interest in recording of seismic rotations.

Ring lasers are very large, a few meters on a side as show in Figure 2.1(a). They require constant temperature and pressure conditions, and need to be balanced. Consequently, they aren't applicable for active seismic field surveys.

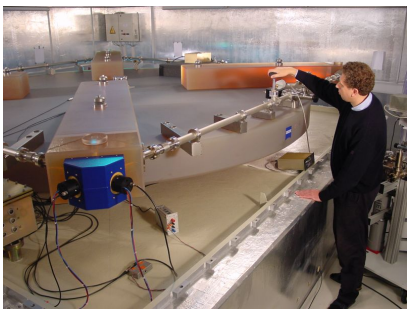

(a)

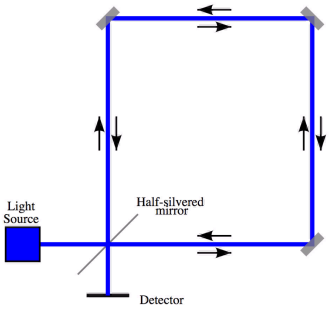

(b)

Figure 2.1: a) The ring laser gyroscope in Wettzell, Germany (Source: http://www.fs.wettzell.de). b) Schematic of the ring laser's operation principle (Source: https://en.wikipedia.org/wiki/Sagnac_effect). Two beams of laser light are shot in opposite directions. If the structure rotates around the axis perpendicular to the plane of the light beams, a frequency interference proportional to the rotation will occur as a result of the change of the length of the path the light beams traverse. [**NR**] chap2/. wetzel-ring-laser,ring-laser-schematic

Fiber-optic Gyroscope

Fiber-optic gyroscopes (FOGs) operate on the same principle as ring lasers, a recording of the Sagnac effect. However, instead of having a large instrument, the FOG economizes on size by having a coiled optical fiber. Two counter propagating, polarized light beams are shot into both ends of the coiled loop (Figure 2.2(b)). When rotation occurs, a phase shift proportional to the rotation is measured. The sensitivity of the instrument can be controlled by the number of coiled loops. Furthermore, they are small enough so that three perpendicular instruments may be assembled into one casing, as shown in Figure 2.2(a). FOGs are used in a variety of platforms that require attitude control such as planes, missiles and submarines.

Current FOGs have reasonable sensitivity at low frequencies, approximately 10^{-8} rad/sec at frequencies below 10 Hz. New models are being developed that would deliver the same sensitivity at higher frequencies that are within the seismic band of interest. However, a possible hindrance to adoption of FOGs in industrial seismic acquisition is their relatively high power usage.

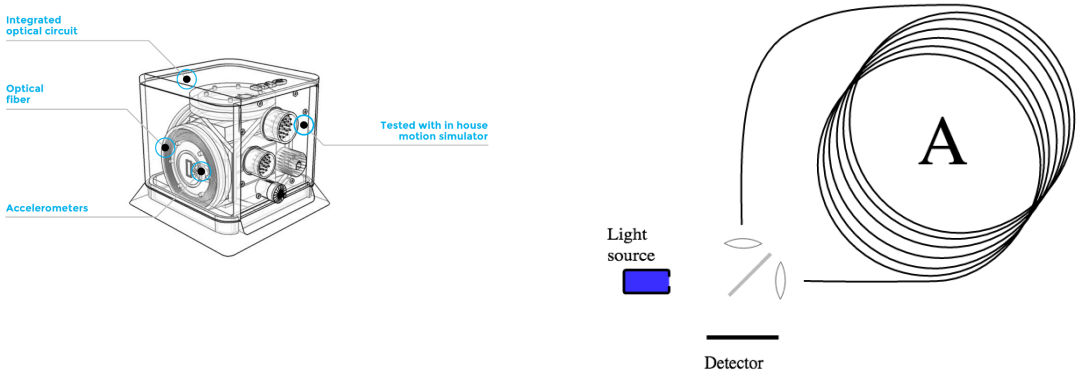

(a) (b)

Figure 2.2: a) a Fiber-optic ring laser gyroscope schematic (Source: http://web.ixblue.com/cn/aw6ym/fiberoptic-gyroscope). b) Schematic of the operating principle of a fiber-optic ring laser gyroscope (Source: https://en.wikipedia.org/wiki/Fibre_optic_gyroscope). Light is shot into both ends of the coiled fiber. The light beams' interference will change in proportion to the rotation rate of the instrument. [**NR**] chap2/. iXblue-FOG,FOG-schematic

Magnetohydrodynamic sensor

A magnetohydrodynamic sensor comprises a locally generated static magnetic field with a conductive fluid as a proof mass to measure rotations. A constant magnetic flux is generated through the central axis of the instrument (Figure 2.3(b)). when the instrument rotates, the inertia of the conductive fluid keeps it in place, resulting in a relative motion between the conductive fluid and the magnetic field. This results in an induced radial electric field, the strength and direction of which are proportional to the amount of rotation.

These types of instruments are physically very small, a few centimeters on a side (Figure 2.3(a)), and have low power consumption. They can record frequencies relevant to seismic exploration, and are currently being used in boreholes to record microseismic energy. Current sensors have a noise floor on the order of 10^{-6} rad/sec and a dynamic range of 100 dB, which may be sufficient for industrial exploration seismology purposes. However, I have not had personal experience with these sensors, so I would be reluctant to make claims about their usefulness.

Electrokinetic sensor

Electrokinetic rotation sensors operate on a principle similar to a magnetohydrodynamic rotation sensor, however for these sensors there is no induced magnetic field involved. There is a a conductive fluid within ring structures, shown in Figure 2.4(b), which acts as the inertial mass. When rotation occurs around the axis perpendicular to the ring structure, the relative motion between the fluid and electrodes embedded within the ring structure generates a current proportional to the rotation rate.

According to manufacturer specifications, the "R2" sensor shown in Figure 2.4(a) has a noise floor of 5.7×10^{-7} rad/sec, and has a flat requency response in the frequency range of 0.05 to 20 Hz.

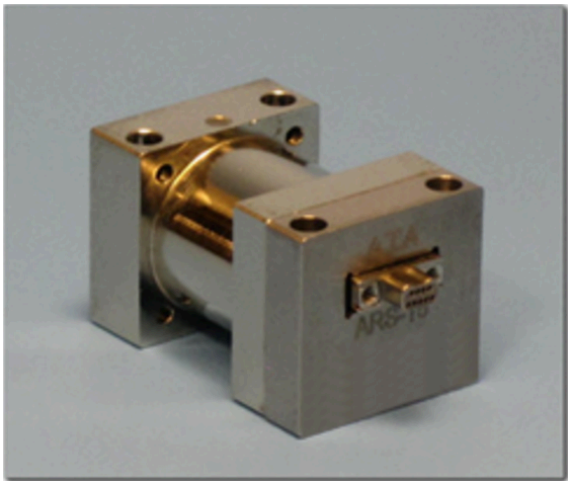

(a)

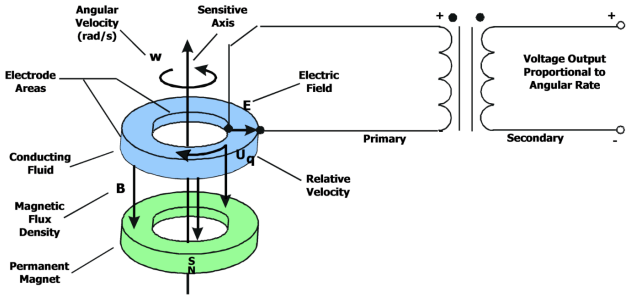

(b)

Figure 2.3: a) A Magnetohydrodynamic sensor. b) Schematic of a magnetohydrodynamic sensor capable of recording rotational signals down to 10^{-6} rad/sec. A magnet fixed to the sensor casing generates a magnetic flux through the center of the instrument. A conducting fluid acts as an inertial proof mass, when the sensor rotates, the relative velocity between the fluid and the magnetic flux generates a radial electric field, proportional to the rotation rate. (Source: http://www.aptec.com/) [**NR**] chap2/. ARS-15-MHD,MHD-schematic

(a) (b)

Figure 2.4: a) An R2 electrokinetic inertial rotation sensor in its casing, approximately 12 cm on each side (The model name given by the original company that built them is "METR03"). b) The internals of the sensor, showing the ring structures. The ring structures are filled with an electrolytic fluid, which generates a current when the sensor rotates around the axis perpendicular to the ring. The amount of current is proportional to the rotation rate. Each sensor has three perpendicular rings, and can therefore record 3-component ground rotations (Figure courtesy of Robert Brune). [**NR**] chap2/. METR03,R2-sensor-internal

Estimating rotations by geophone differencing

Rotations can be estimated by differencing closely-spaced geophones, a method sometimes termed "array-derived rotations" in literature. In Hooke's law, the stress-displacement relation for tangential stresses reads:

$$\sigma_{ij} = \mu \left(\partial_j u_i + \partial_i u_j \right), \tag{2.1}$$

where σ_{ij} are the tangential stresses, u_i are particle displacements and μ is the shear modulus.

At a free surface, or when going from a medium with shear strength to one without shear strength (such as the ocean-bottom interface), the tangential stresses σ_{xz} and σ_{yz} are zero. Therefore, assuming we have receivers laid out on a flat free surface, we have

$$\begin{aligned} \partial_z u_y &= -\partial_y u_z, \\ \partial_z u_x &= -\partial_x u_z, \end{aligned} \tag{2.2}$$

meaning that the vertical derivative of the horizontal displacement component is equal to the horizontal derivative of the vertical displacement component.

Rotations are defined as the curl of the wavefield as shown in eq. 1.5. Since geophones record the time-derivative of displacement (particle velocity), I use the time-derivative of rotation, or rotation rate:

$$\vec{r} = \frac{1}{2}(\nabla \times \vec{v}) = \frac{1}{2}\left(\hat{X}\left(\partial_y v_z - \partial_z v_y\right) + \hat{Y}\left(\partial_z v_x - \partial_x v_z\right) + \hat{Z}\left(\partial_x v_y - \partial_y v_x\right)\right). \quad (2.3)$$

Substituting equation 2.2 into 2.3, we see that on a free surface

$$\begin{aligned} \text{(roll)} \quad r_x &= \partial_y v_z, \\ \text{(pitch)} \quad r_y &= -\partial_x v_z, \\ \text{(yaw)} \quad r_z &= \frac{1}{2}\left(\partial_x v_y - \partial_y v_x\right), \end{aligned} \quad (2.4)$$

i.e., the horizontal rotation-rate components can be derived by differencing vertical geophones, and the vertical rotation-rate components can be derived by differencing horizontal geophones.

The challenge with estimating rotations from geophone differencing is determining the distance required between the adjacent geophones. The upper bound for the distance between the geophones is half the horizontal spatial wavelength, in order to avoid aliasing. The lower bound, however, depends on the level of ambient noise. Differencing the signal of two adjacent geophones necessarily decreases the signal to noise ratio, as we are subtracting most of the actual signal that was recorded on the two geophones. Furthermore, the two geophones may have different coupling to the ground, and the inherent instrument response of the geophones may not be perfectly identical.

To determine the upper bound for the desired spacing between the geophone pairs being differenced, we must make assumptions regarding the frequency and wavenumber of the expected arrivals. To determine the lower bound, we must know the difference in instrument response and coupling for each pair of geophones, and the ambient noise characteristics at each receiver station. Therefore, in practice, acquiring rotations for broadband data by geophone differencing alone may not be reliable.

We would ideally prefer to not rely on geophone differencing for rotational-data acquisition. The exception is the Rotaphone instrument.

Rotaphone

The Rotaphone (Brokesova and Malek, 2015) is an instrument that effectively calculates equations 2.4 on data acquired by pairs of closely-spaced geophones placed on a free surface. Figure 2.5(a) is a photo of the instrument, and 2.5(b) shows the instrument design. The reliable operation of the Rotaphone depends on an in-situ callibration procedure, where the differences in instrument response and coupling for each pair of geophones are explicitly measured, and are later accounted for during field recording. The reliance on multiple pairs of geophones to record the rotations further reduces any errors that result from the differencing of the closely-spaced geophones. Since the Rotaphone has multiple geophones, it effectively records all six components of motion. As of October 2016, two prototype Rotaphone instruments are being tested for microseismic recordings at The Geysers geothermal plant in California.

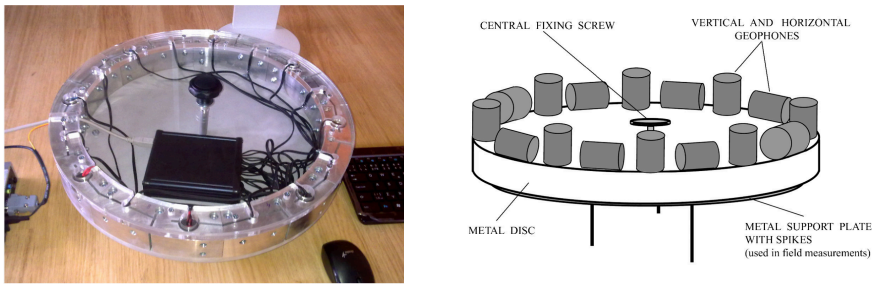

(a) (b)

Figure 2.5: a) A Rotaphone instrument. The diameter of the disc is 44.5 cm. b) Schematic of the Rotaphone. The sensor system consists of vertical and horizontal geophones mounted in parallel pairs to a rigid frame anchored to the ground. Separation distance between each geophone pair along the circumference of the disc is 40 cm, much smaller than the seismic wavelength the instrument is designed to record. According to its designers, the dynamic range of the rotaphone is 120 dB, and it can record rotations down to 4 nrad/s. (Source: http://rotaphone.eu) [**NR**] chap2/. rotaphone,rotaphone-schematic

MAGNETOMETERS AS ROTATION SENSORS

The objective of this chapter is to show how rotation data can be derived from Induction-Coil Magnetometer (ICM) recordings. This concept was explored previously in Kappler et al. (2006) using earthquake data recorded by USGS permanent electromagnetic (EM) land stations in California. The attempt was to explain the coseismic signal appearing on the EM components as a product of ground rotations. I expand on this concept and conduct a seismic field survey using both rotations sensors and ICMs, to validate if and how ICMs may be used as seismic rotation sensors.

ICMs are currently being used in large-scale magnetotelluric and controlled-source electromagnetic surveys, are field deployable in a variety of land and marine environments, and also have a low power consumption. Therefore, the possibility of deriving seismic rotations from magnetometers is compelling, as this acquisition technology is robust and has already seen academic and commercial use. The seismic exploration industry is experienced in deploying these instruments.

ICMs (Figure 2.6) operate according to Faraday's law. Copper wire is wound around a magnetically permeable core. When a change in the magnetic flux perpendicular to the coil's cross-section occurs, a current is induced in the wires.

I explain the connection between magnetic flux changes and seismic rotations as follows: Assume three orthogonal ICMs coupled to the ground, and rotating with the ground as a result of a seismic wave generating a rotational deformation of the medium. The Earth's magnetic field, however, does not rotate and is effectively constant in direction and in amplitude for the period of the seismic wave. The ground rotation therefore manifests itself as a change in the projection of the Earth's magnetic field on the orthogonal ICM components. An illustration of this is shown in Figure 2.7.

The change in projection of the Earth's magnetic field on the ICM components results in a change of flux through the coils, and generates a current. After designature of the ICM, and taking into account the local magnetic field at the point of measurement, we can translate the ICM recording of magnetic flux deviations in Teslas to rotations in radians.

It must be noted that other explanations exist for coseismic EM signals, such as the electrokinetic effect. However, the model that explains coseismic EM data using

Figure 2.6: Induction-Coil Magnetometers, built by the Scripps Institute of Oceanography. Coils of aluminium wire are wound around a magnetically permeable core. A current is induced in the wire when the magnetic flux perpendicular to the coil's cross section changes. [**NR**] chap2/. ICMs

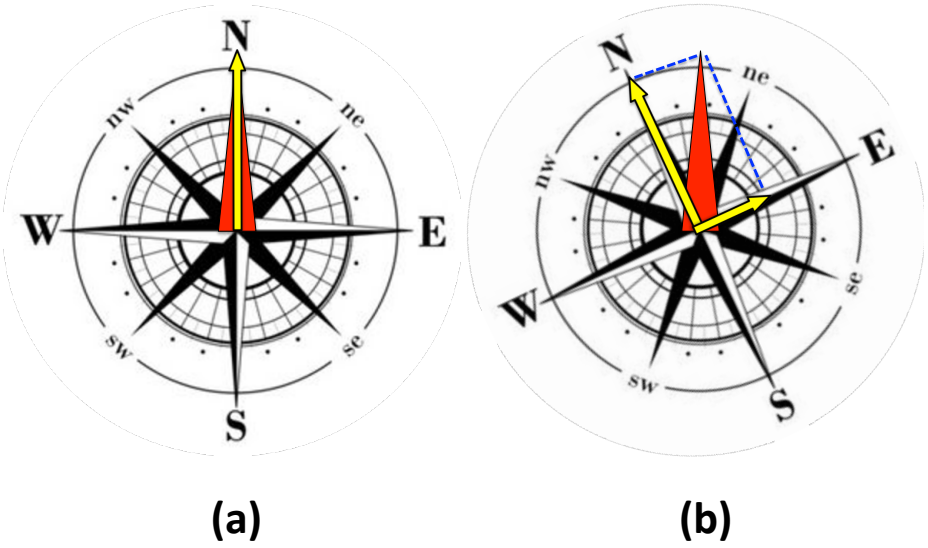

Figure 2.7: Illustration of how ground rotation is recorded on the magnetic field sensor as represented by the compass, which is coupled to the ground. (a) Before ground rotation, the magnetic field (red) is recorded only by the North component (yellow). (b) During ground rotation, the magnetic field (red) does not change, but its projection on the North and East components (yellow) changes. We can calculate the amount of rotation from the change in projection. Note that translations of the ground will not result in a change of the projection of the magnetic field on the magnetic components. [**NR**] chap2/. compass-rotation

the electrokinetic theory has many unconstrained parameters (Pride, 1994). I do not discount the electrokinetic theory as a model for coseismic EM data, since a seismo-electric effect has been experimentally shown to exist by Haines (2004). However, even though the correct combination of the electrokinetic model parameters may explain some of the coseismic EM signal appearing on induction-coil magnetometers, ground rotations are a more parsimonious model that explains these data, and by Occams razor are therefore preferable. Additionally, in the particular field survey we conducted, it is unlikely that the coseismic signal was caused by electrokinetic effects. The presence of water is crucial for generation of a coseismic electrokinetic signal. However, our survey site is extremely arid, and the depth of investigation was shallow, well above the water table.

CONVERSION FROM INDUCTION-COIL MAGNETOMETER RECORDINGS TO ROTATION RATES

Designature of magnetometer data

Faraday's law states that the voltage V generated within a loop of wire is proportional to the rate of change of the magnetic flux Φ passing through the loop

$$V = -\frac{d\Phi}{dt}. \tag{2.5}$$

In an ICM, there are N loops of wire wound around a cylinder of area A. The flux can be written as $\Phi = NAB$, where B is the magnetic induction normal to the area of the wire loop

$$V = -NA\frac{dB}{dt}. \tag{2.6}$$

The magnetic induction B is related to the magnetic field H as $B = \mu_0\mu_r H$, where μ_0 is the magnetic permeability of free space and μ_r is the relative magnetic permeability of the material that the loop of wire is wound around. The expression for an ICM which includes a permeable core is then

$$V = -NA\mu_0\mu_r \frac{dH(t)}{dt}. \tag{2.7}$$

Equation 2.7 shows that the output voltage is linearly related to the number of turns of the wire N, the area of the loops A and the relative permeability of the core material in the loop μ_r. The sensitiviy of the ICM can be controlled by varying these parameters.

Assuming a harmonic time function for the magnetic field $H(t) = H_0 e^{i\omega t}$, the frequency response of an air core ICM is

$$|V| = \omega NA\mu_0 H_0. \tag{2.8}$$

The air core magnetometer has a voltage sensitivity that is proportional to the frequency. For an ICM with a permeable core, additional boundary conditions of the induced magnetic field in the core are required to derive an accurate instrument response. These conditions have been derived by Key (2003), and are used when designaturing the instrument response of the ICM.

The magnetic data after designature are the small deviations of the magnetic field strength on the 3 orthogonal magnetic components over time:

$$\vec{H}^{\text{dev}}(t) = [H_x^{\text{dev}}(t), H_y^{\text{dev}}(t), H_z^{\text{dev}}(t)]. \tag{2.9}$$

In order to have the total projection of the Earth's ambient magnetic field on each ICM components, I add the ambient field value using data from the World Magnetic Model ($\vec{H}^{\text{wmm}}$) (British Geological Survey, 2014) for the location and date when the data were gathered:

$$\vec{H}(t) = [H_x^{\text{dev}}(t) + H_x^{\text{wmm}}(t), H_y^{\text{dev}}(t) + H_y^{\text{wmm}}(t), H_z^{\text{dev}}(t) + H_z^{\text{wmm}}(t)]. \tag{2.10}$$

The Earth's predominant magnetic field is not constant, but it changes at time scales much larger than the period it takes to execute a small seismic survey (9 hours, in our case).

The forward modeling process: Conversion from rotation sensor data to magnetic vector projections

I consider the ground rotations to be the "model" of rotations **m**. The forward modeling operator **F** converts the rotations model to magnetic vector projection data, i.e., $\mathbf{d} = \mathbf{Fm}$. The forward modeling operator itself is an Euler rotation matrix. The rotation matrix applies 3D rotations to the projections of the ambient magnetic field, as specified by the World Magnetic Model, on each magnetometer component:

$$\begin{bmatrix} H_x \\ H_y \\ H_z \end{bmatrix} = \begin{bmatrix} c(R_y)c(R_z) & -c(R_y)s(R_z) & s(R_y) \\ c(R_x)s(R_z) + c(R_z)s(R_x)s(R_y) & c(R_x)c(R_z) - s(R_x)s(R_y)s(R_z) & -c(R_y)s(R_x) \\ s(R_x)s(R_z) - c(R_x)c(R_z)s(R_y) & c(R_z)s(R_x) + c(R_x)s(R_y)s(R_z) & c(R_x)c(R_y) \end{bmatrix} \begin{bmatrix} H_x^{\mathrm{wmm}} \\ H_y^{\mathrm{wmm}} \\ H_z^{\mathrm{wmm}} \end{bmatrix}, \tag{2.11}$$

where c and s are cosine and sine, respectively, and $R_{(xyz)}$ are the components of the rotation vector. I subtract the ambient field in order calculate the magnetic deviations we would expect the magnetometers to record given the ground rotations:

$$\vec{H}^{\mathrm{dev}}(t) = [H_x(t) - H_x^{\mathrm{wmm}}(t), H_y(t) - H_y^{\mathrm{wmm}}(t), H_z(t) - H_z^{\mathrm{wmm}}(t)]. \tag{2.12}$$

The reverse mapping process: rotations from magnetic vector projections

Application of equations 2.5 to 2.10 provides the values of the projections of a constant vector on our 3 orthogonal components. Our components are rotating in space over time, and therefore the vector's projection on the 3 orthogonal components changes according to the rotations.

I consider the magnetic vector projections to be our data **d**. The reverse mapping operator **L** converts the magnetic vector projection data to a model of rotations, i.e., $\hat{\mathbf{m}} = \mathbf{Ld}$. In order to calculate the rotations from the projections, I first convert the projection data to the axis-angle representation. The angle of rotation between

consecutive time steps is calculated by

$$\theta(t) = \cos^{-1}\left(\frac{\vec{H}(t+\Delta t)\cdot\vec{H}(t)}{\left|\vec{H}(t+\Delta t)\right|\left|\vec{H}(t)\right|}\right), \tag{2.13}$$

while the unit vector describing the axis of rotation is

$$\hat{u}(t) = \frac{\vec{H}(t)\times\vec{H}(t+\Delta t)}{\left|\vec{H}(t)\times\vec{H}(t+\Delta t)\right|}. \tag{2.14}$$

Equations 2.13 and 2.14 provide the total amount of rotation and the axis of rotation. However, in order to have meaningful rotation data, i.e., comparable to the measurements we would expect from a three-component rotation sensor, we need to convert from the axis-angle representation to the rotation rate around the three orthogonal axes. For that, we must first convert to a quaternion representation of the rotation angle and axis. The interested reader may refer to Hanson (2005) for a comprehensive explanation of the concept of quaternions, as put forth by Hamilton (1844).

Our quaternion four-vector system state $\mathbf{q}$ begins with no rotation, i.e.

$$\mathbf{q}(t=0) = \begin{pmatrix} q_w \\ q_x \\ q_y \\ q_z \end{pmatrix} = \begin{pmatrix} 1 \\ 0 \\ 0 \\ 0 \end{pmatrix}. \tag{2.15}$$

I use equations 2.13 and 2.14 to get the rotation angle θ and the rotation axis $\vec{u}$, and then convert to a quaternion representation of the rotation $\mathbf{p}$ with

$$\mathbf{p}(t) = \begin{pmatrix} \cos\frac{\theta(t)}{2} \\ u_x(t)\cdot\sin\frac{\theta(t)}{2} \\ u_y(t)\cdot\sin\frac{\theta(t)}{2} \\ u_z(t)\cdot\sin\frac{\theta(t)}{2} \end{pmatrix}. \tag{2.16}$$

In order to rotate our system from its state at time t to its new state at time $t+\Delta t$, we need to apply quaternion multiplication ($\star$) of the quaternion $\mathbf{q}$ by $\mathbf{p}$:

$$\mathbf{q}(t+\Delta t) = \mathbf{p}(t+\Delta t) \star \mathbf{q}(t) = \begin{pmatrix} p_w q_w - p_x q_x - p_y q_y - p_z q_z \\ p_w q_x + p_x q_w + p_y q_z - p_z q_y \\ p_w q_y - p_x q_z + p_y q_w + p_z q_x \\ p_w q_z + p_x q_y - p_y q_x + p_z q_w \end{pmatrix}. \tag{2.17}$$

We can now retrieve the rotations in terms of Euler angles around each axis using the formulation in Diebel (2006):

$$\vec{R}(t) = \begin{pmatrix} \arctan\left(\frac{2q_y q_z + 2q_w q_x}{\left(q_z^2 - q_y^2 - q_x^2 + q_w^2\right)}\right) \\ \text{-arcsin}\left(2\left(q_x q_z - q_w q_y\right)\right) \\ \arctan\left(\frac{2q_x q_y + 2q_w q_z}{q_x^2 + q_w^2 - q_z^2 - q_w^2}\right) \end{pmatrix}, \tag{2.18}$$

In order to get the rotation rate, I apply a first derivative on the time axis:

$$\vec{r}(t) = \frac{d\vec{R}(t)}{dt}. \tag{2.19}$$

Equations 2.13-2.19 constitute the reverse-mapping operator $\mathbf{L}$ which, it is important to note, is not the adjoint nor the inverse of the forward operator $\mathbf{F}$.

The null space of magnetic projections: rotations around the ambient magnetic-field axis

To derive rotations, I rely on the changes of projection of the magnetic field on the three orthogonal ICMs. However, if any part of the rigid-body rotation occurs directly around the magnetic field's axis, no change in projection will occur, and we will effectively be blind to these rotations.

A synthetic example demonstrates this for a scenario where an ICM has sensor antennas in the X, Y and Z directions, and where the ambient magnetic field is constant along the Z axis with a value of 1 Tesla $\vec{H} = (0, 0, 1)$. The solid lines in Figures 2.8(b), 2.8(d) and 2.8(f) are the true rotations applied to the ICM. I use equation 2.11 to forward model the change in magnetic projections recorded by the

three components of the ICM as a result of the rotations. The forward-modeled magnetic projections are shown in Figures 2.8(a), 2.8(c) and 2.8(e). The dashed lines in Figures 2.8(b), 2.8(d) and 2.8(f) are the result of applying the reverse mapping operation in equations 2.13 to 2.19 to the forward-modeled magnetic projections.

In Figure 2.8(a) we see the change in magnetic projections resulting from a rotation around the X axis $\vec{u} = (1, 0, 0)$. Since the Y antenna is maximally coupled to the field (as $\sin(\theta)$, since it is pointing 90 degrees away from the field), we see a strong response of the Y projection to a rotation around the X axis. There is also a weak change in the Z projection, since the Z antenna is weakly coupled to the ambient field (as $\cos(\theta)$).

In Figure 2.8(b) I show the rotation rates that were applied to the system in solid lines (the true model $\mathbf{m}$), and the rotation rates derived from the magnetic projections in dashed lines (the estimated model $\hat{\mathbf{m}} = \mathbf{Ld}$). The only rotation that occured in this case is around the X axis, and it is recovered correctly.

In Figure 2.8(c) the rotations are around both the X and Y axes $\vec{u} = \left(\frac{\sqrt{2}}{2}, \frac{\sqrt{2}}{2}, 0\right)$. We see a strong response of the Y projection to a rotation around the X axis, and a strong response of the X projection to the rotation around the Y axis. Again, there is also a weak change in the Z projection. Observing Figure 2.8(d), we see that both of the rotations around X and around Y were recovered. Note that some rotation occurs around the Z axis as well. This is a result of the coupling between components of 3D rotations: it is not possible to rotate around two axes without causing the third axis to change its attitude in relation to the external frame.

In Figure 2.8(e) the rotations are the X, Y and Z axes $\vec{u} = \left(\frac{\sqrt{3}}{3}, \frac{\sqrt{3}}{3}, \frac{\sqrt{3}}{3}\right)$. Observe that there is no difference in phase between Figures 2.8(e) and 2.8(c). The rotation around the Z axis does not generate a change in projection of the magnetic field on the ICM components. Consequently, observing the bottom panel of Figure 2.8(f), we see that the rotations around the Z axis were not recovered, as the amplitude is much lower and the phase is wrong.

Both the amplitude reduction and phase difference effects in the modeled rotations are the result of the null space of the magnetic projections. We cannot recover the amplitude correctly for the rotations occuring around the ambient magnetic field's direction. Additionally, and rather surprisingly, the fact that all other rotations can

be recovered correctly is what generates the phase difference between the induced rotations and the recovered rotations seen on the bottom of Figure 2.8(f). What we observe are the rotations around Z that are the result of the combined rotations around both X and Y.

The conclusion from Figures 2.8(a)-2.8(f) is that if we rely on the Earth's constant ambient magnetic field to record rotations on a three-component ICM, we will likely not recover all rotations accurately in a seismic survey. Whether this effect is relevant depends on the application for which we intend to use the derived rotational data. It also depends on where the seismic survey is conducted.

For example, in mid-latitudes the inclination of the magnetic field is between 30 and 60 degrees, dipping towards the North or the South. Therefore, we may not lose much of the rotational energy around the vertical or horizontal axes. Conversely, on the North pole where the magnetic inclination is 90 degrees, we would be unable to record the yaw component.

SILVER LAKE SURVEY

The test survey was conducted at Silver Lake, near the town of Baker, California. Dr. Shuki Ronen and I did the survey in conjunction with a field-methods course taught by Prof. Steven Constable and Dr. Kerry Key from the Scripps Institute of Oceanography, with the active participation of their students. Silver Lake is a dry lake bed in the Mojave Desert, where both seismic and magnetic noise are weak enough for our purposes.

Rotations were measured using three methods:

1. Three-component "R2" electrokinetic rotation sensor (Figure 2.4(a)): direct measurement of rotations

2. Three-component ICM (Figure 2.6): measurement of rotations derived from changes in magnetic projections (Equations 2.5-2.19)

3. Geophone differencing of adjacent vertical geophones (Equation 2.4) (Muyzert et al., 2012; Barak et al., 2014).

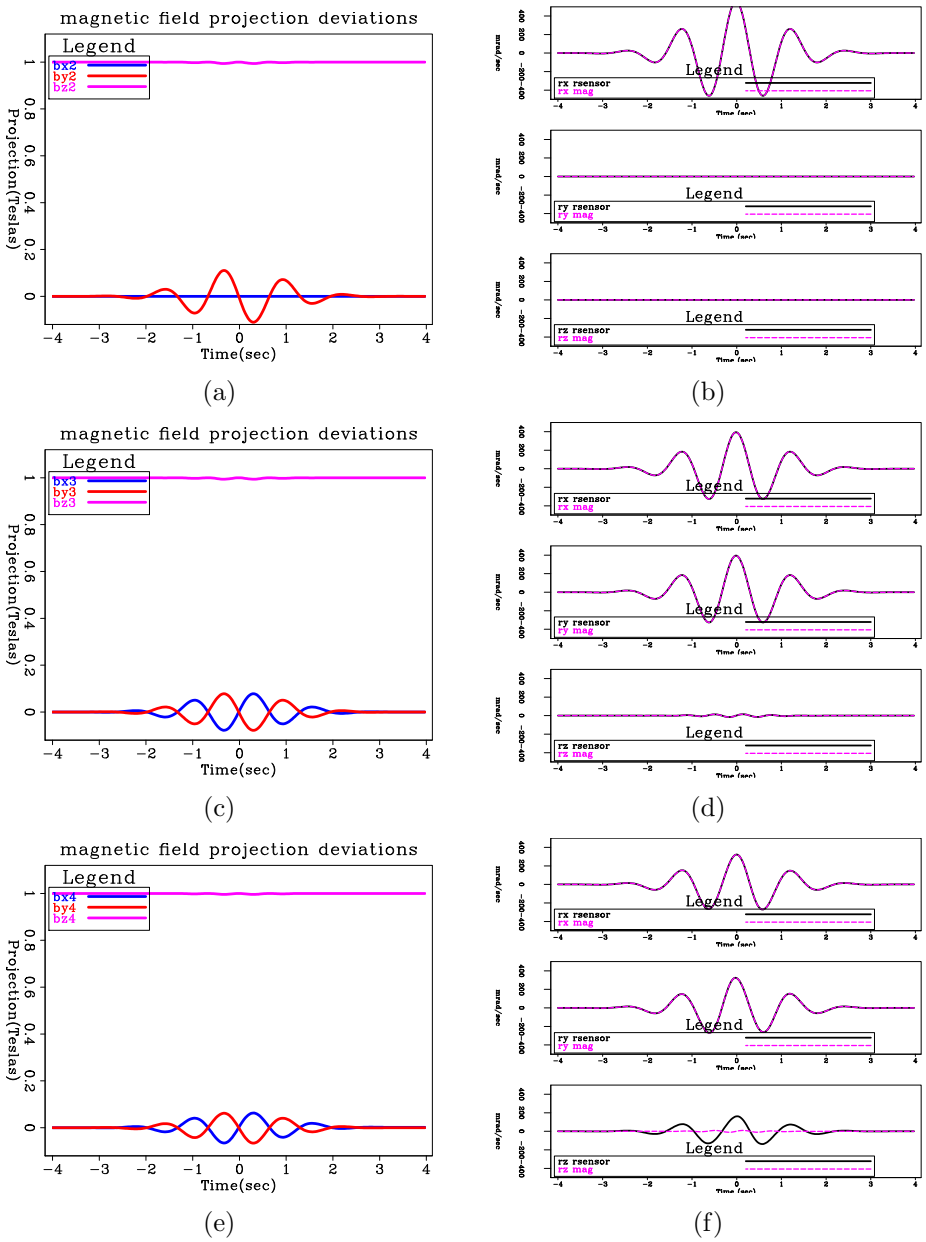

Figure 2.8: (a), (c) and (e): Changes in magnetic projections on three orthogonal components as a result of rotations of the components within a constant magnetic field $\vec{H} = (0, 0, 1)$ (a vertical magnetic field, as is the case in the Earth's North pole). (b), (d) and (f): The rigid-body rotations (solid lines) that caused the change in magnetic projections, and the rotations derived from the changes in magnetic projections (dashed lines). In (a) and (b), the rotation axis is $\vec{u} = (1, 0, 0)$ (only around the X axis), and the rotation is recovered correctly. In (c) and (d), the rotation axis is $\vec{u} = \left(\frac{\sqrt{2}}{2}, \frac{\sqrt{2}}{2}, 0.\right)$ and the rotations are recovered correctly. In (e) and (f), the rotation axis is $\vec{u} = \left(\frac{\sqrt{3}}{3}, \frac{\sqrt{3}}{3}, \frac{\sqrt{3}}{3}\right)$ The rotation around the Z axis (the direction of the magnetic field) is not recovered correctly. Rotations around the magnetic field axis cannot be derived since they do not cause a change in the projections. [**ER**]

chap2/. testcomp2-b,testcomp2-rall,testcomp3-b,testcomp3-rall,testcomp4-b,testcomp4-rall

To acquire these data, we deployed three composite stations comprising the three types of sensors, as shown in Figure 2.9(a). The 'X' (roll) components of both the ICMs and the rotations sensors were oriented in the inline survey direction, which was toward magnetic azimuth 120^o as measured by a compass. The 'Y' (pitch) components were oriented in the crossline direction, toward magnetic azimuth 30^o. The 'Z' (yaw) was positive downward. Since the magnetic inclination at Silver Lake was 60^o at the time of the survey, all the magnetometer components were coupled to the magnetic field, i.e., the ambient magnetic field had a significant projection on each magnetometer component.

I further estimated the pitch component by differencing the two adjacent vertical geophones in the inline direction. The roll component was estimated by differencing the two adjacent vertical geophones in the crossline direction. I could not, however, obtain an estimate for the yaw rotational component by geophone differencing, since we did not have any horizontal geophones.

We had three composite stations, deployed using the pattern shown in Figure 2.9(b). The spacing between receiver stations was 3 meters, and the shot interval was 5 meters. As a seismic source, we used a Betsy gun. An example of the ignition of one Betsy gun shot is shown in Figure 2.10(a). The station deployment is shown in Figure 2.10(b). We used a builder's level to ensure orthogonality between components, and a compass to measure the orientations.

Aside from the three composite stations we used to acquire the active seismic data, we also deployed a remote ICM station (Figure 2.10(c)), far from the shot locations. The purpose if this receiver was to measure the ambient magnetotelluric noise for later removal from the active-seismic ICM data.

Sensitivity of magnetometers to ground rotations

Consider a very simple rotation of the magnetometer axes about the z axis by an angle θ. The magnetic field $\mathbf{H}$ along the sensor axes is then

$$\begin{bmatrix} H_x' \\ H_y' \\ H_z' \end{bmatrix} = \begin{bmatrix} \cos(\theta) & \sin(\theta) & 0 \\ -\sin(\theta) & \cos(\theta) & 0 \\ 0 & 0 & 1 \end{bmatrix} = \begin{bmatrix} H_x \\ H_y \\ H_z \end{bmatrix} \tag{2.20}$$

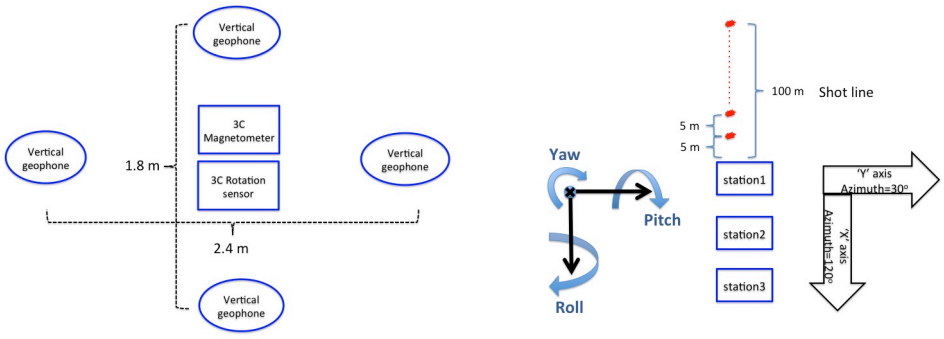

(a) (b)

Figure 2.9: (a) The arrangement of a single composite station in the Silver Lake survey. Each station had 3 orthogonal ICMs, and a 3C inertial rotations sensor. Two geophones were placed in close proximity in the inline and in the crossline directions. (b) 20 shots were executed off-end, at 5-meter intervals, for a total of 100m of offset. The 'X' (roll) components of the rotation sensors and the ICMs were along the inline direction toward magnetic heading 30^o. The 'Y' (pitch) components of the rotation sensors and the ICMs were along the crossline direction toward magnetic heading 120^o. The 'Z' (yaw) components are downward, while magnetic inclination was 60^o. Note that the figure is not to scale. The distance between the composite stations was 3 meters. [**NR**] chap2/. silverlake-station,silverlake-shots

For a magnetic field $\vec{H} = (H_0, 0, 0)$, the field in the rotated coordinates will be

$$H_x^{'} = \cos(\theta) H_x, \tag{2.21}$$
$$H_y^{'} = -\sin(\theta) H_y, \tag{2.22}$$
$$H_z^{'} = 0. \tag{2.23}$$

The change in the magnetic field measured by the magnetometers is

$$\Delta H_x = H_x^{'} - H_x = (1 - \cos(\theta)) H_x, \tag{2.24}$$
$$\Delta H_y = H_y^{'} - H_y = -\sin(\theta) H_y, \tag{2.25}$$
$$\Delta H_z = 0. \tag{2.26}$$

The table below shows the magnetic field changes for various amounts of rotations assuming a nominal 50,000 nT (Earth) magnetic field along x. This shows that a microradian rotation would produce a pico-Tesla level signal on H_y, the maximally coupled orientation direction. Since the magneto-telluric (MT) field in Silver Lake in

(a)

(b)

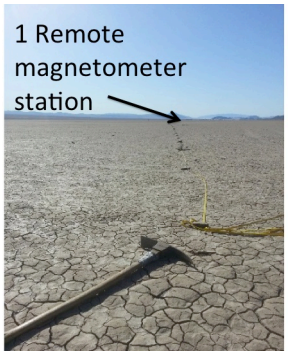

(c)

Figure 2.10: (a) Execution of one of the 20 shots using the Betsy gun. (b) One of the 3 composite stations. The rotation sensor is housed in the grey box, while the ICMs are the white rods arranged orthogonally. (c) We placed one remote 3-component ICM station far from where we were shooting the seismic data, to record the ambient magnetotelluric noise for later removal in processing. [**NR**] chap2/. silverlake-betsy,silverlake-magandrot,silverlake-remote

the seismic frequency band (1 Hz - 100 Hz) is about $10^{-12}\mathrm{T}/\sqrt{\mathrm{Hz}}$, we can expect to be able to detect rotations down to 1 microradian.

θ (rad)	$\lvert 1-\cos(\theta)\rvert$	$\lvert\sin(\theta)\rvert$	$5 * 10^{-5}\lvert\sin(\theta)\rvert$ Tesla
1e-09	0	1e-09	5e-14
1e-08	0	1e-08	5e-13
1e-07	5e-15	1e-07	5e-12
1e-06	5e-13	1e-06	5e-11
1e-05	5e-11	1e-05	5e-10
1e-04	5e-09	1e-04	5e-09
1e-03	5e-07	1e-03	5e-08
1e-02	5e-05	1e-02	5e-07
1e-01	5e-03	0.0998	4.99e-06
1	0.46	0.841	4.21-05

Since the MT field is expected to be laterally uniform over regional spatial scales, we planned to use the remote station to reduce the MT signal from the local measurement, with the possibility of obtaining MT-free data with a spectrum close to the noise floor of the magnetometer antenna we were using (Zonge model ANT/6), which is 10^{-14} to 10^{-13} Tesla, as shown in Figure 2.11. This would give us an equivalent rotational noise floor of about 10^{-9} to 10^{-8} radians.

Amplitude spectra during survey

Figure 2.12(a) shows the spectra of the three magnetometer components at the active-seismic stations while active shooting was being done, while 2.12(b) shows the spectra at the remote station at the same time period. Observe that at low frequencies the ambient magnetic noise is very strong. However, within the typical range of seismic frequencies the ambient magnetic field is between 10^{-1} to 10^{-2} nanoTeslas.

The purpose behind deploying the remote station was to record the ambient magnetic noise without seismic interference, and then remove this noise from the active-seismic magnetometer stations.

From Figure 2.12(b) I could see that the vertical magnetometer antenna at the remote station was recording much higher levels of noise than the horizontal magnetometer components. Further inquiry showed that there was a problem with the vertical antenna's electronics at the remote station. Consequently, I could not use

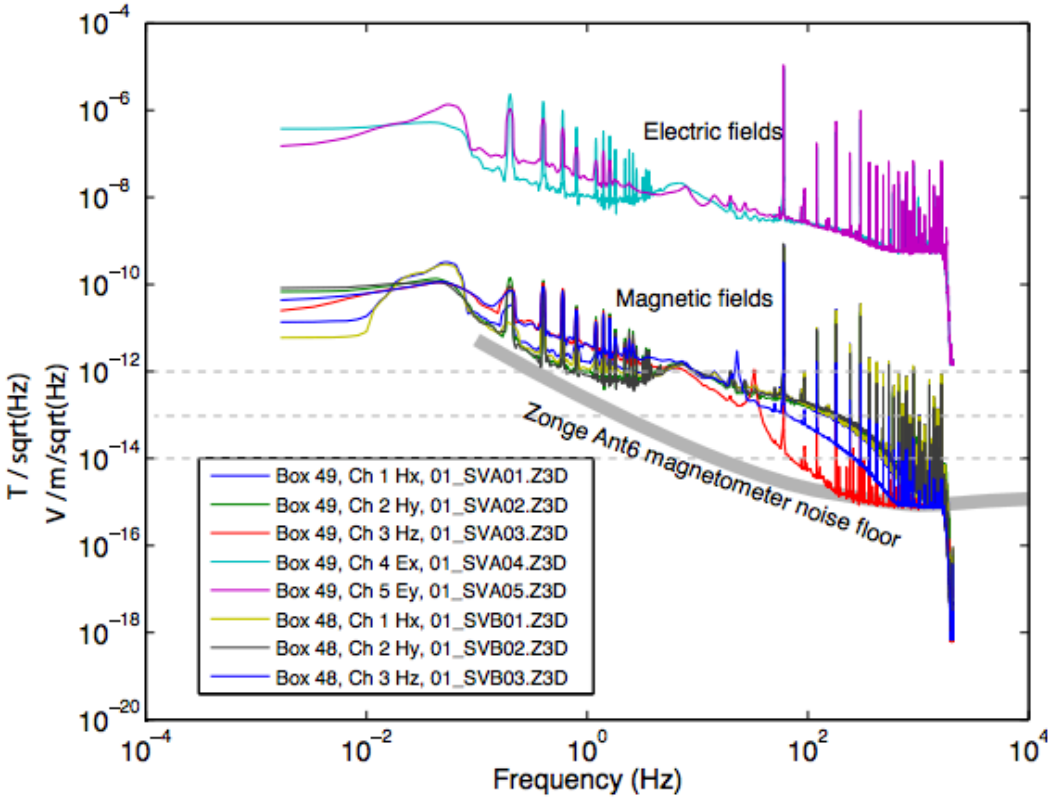

Figure 2.11: Magnetotelluric magnetic and electric fields observed at Silver Lake, Mojave Desert in March 2015, two months before we performed the Silver Lake survey. Also shown is the public-domain noise floor of the Zonge model ANT/6 magnetometer. Spikes are from 60 Hz power line noise and 0.2 Hz cathodic protection system on a nearby gas pipeline. [**NR**] chap2/. silverlake-EM-noise

the vertical magnetometer component at the remote station as a basis for denoising the vertical magnetometer component at the active seismic stations.

Figure 2.12(c) shows the spectra of the three magnetometer components at the active seismic stations after subtraction of the horizontal magnetometer components of the remote station. We see that the majority of the ambient magnetic noise which was removed was in the higher frequency ranges, although there is some reduction of the B_y component's noise between 10 and 30 Hz.

Figure 2.12(d) is the spectrum of the vertical geophone component. It shows that the Betsy gun generated strong seismic energy between 5 and 50 Hz. The microseism band is also apparent in this figure. It seems, however, that the rotation sensors' response rolls off from around 10 Hz and down, and they are not as sensitive as the geophone to the microseism energy. Additionally, from 30 Hz and up some resonances appear on the rotational components. Consequently, and also to reduce some of the magnetic noise, all the following analyses have a bandpass filter between 5 Hz and 30 Hz applied to them.

Designature of rotation sensor

The rotation sensors used in the Silver Lake survey were the "R2" electrokinetic rotation sensors, as shown in Figure 2.4(a). According to manufacturer specifications, these sensors have a noise floor of 5.7×10^{-7} rad/sec, which I assumed to be sufficient for recording rotational data in the Silver Lake experiment. Additionally, some benchtop tests done by Patrycjusz Bachelda from Geokinetics company, who provided us with the sensors, showed that the R2 could reliably record rotational data up to 20 Hz.

The instrument specifications also state that the R2 sensors have a flat phase response in the frequency range of 0.05 to 20 Hz. However, I was unsure whether this was the case for the specific sensors we were using, since the production of these sensors is still very manual. I knew the instrument response of the geophones however, and used it to designature the vertical geophones. I then used vertical-geophone differencing (Eq. 2.4) to get an estimate of the designatured rotational pitch signal. I calculated the phase difference between the rotations measured by the rotation sensors and the rotations estimated by geophone differencing. I then used

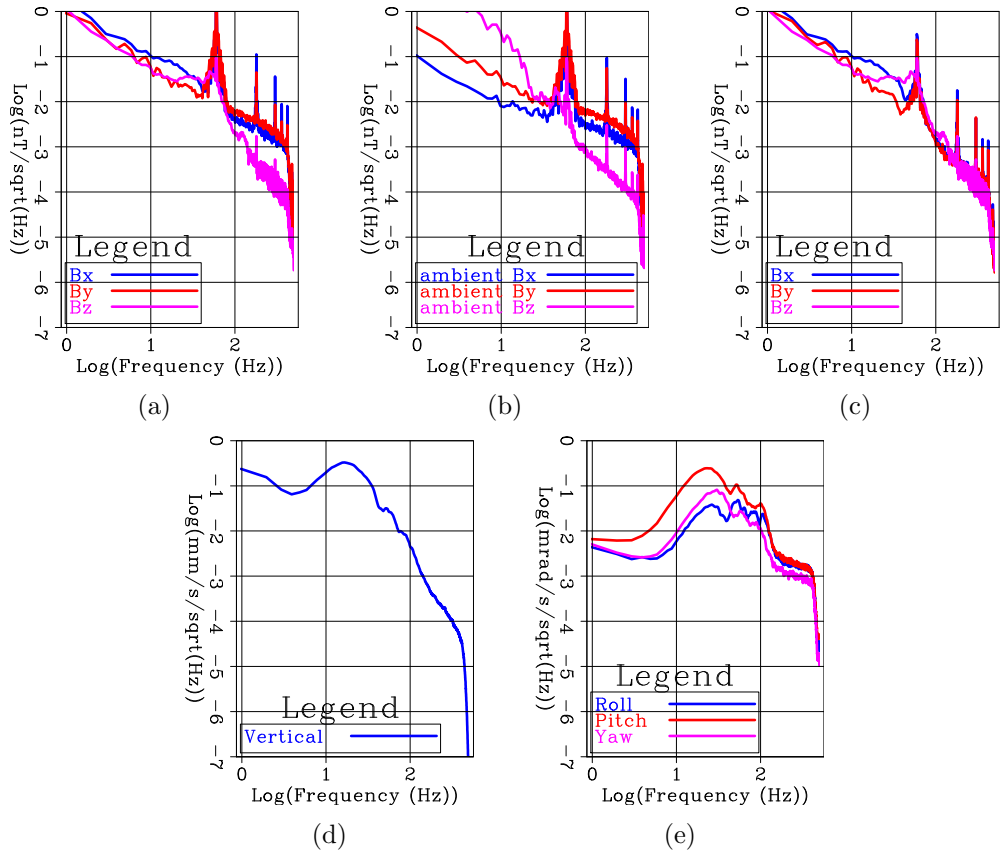

Figure 2.12: Log amplitude spectra of raw data during active shooting, after instrument designature for the various data components was applied. a) Magnetometers before removal of ambient noise. b) Ambient magnetic noise at remote station. c) Magnetometers after removal of ambient noise. d) Vertical geophone. e) Rotation sensors. The B_z component at the remote station recording the vertical ambient magnetic field had problems with its electronics, and therefore recorded much higher levels of noise than were actually in the field. Note the reduction in noise for the B_x and B_y magnetometer components after removal of the ambient field recording. Note that the vertical geophone was recording very low frequencies in the microseism band (below 2 Hz), while the rotation sensors were not, indicating that the rotation sensors we used do not have sufficient sensitivity at the very low end of spectrum. [**ER**] chap2/. mag-spec,remote-mag-spec,clean-mag-spec,vz-spec,rot-spec

this phase difference as the rotation-sensors' instrument response.

Figure 2.13(a) shows a receiver gather of the vertical geophone component at station 1 of the Silver Lake data. The direct P-wave, propagating at a velocity of 1420 m/s, is much weaker than the ground roll, and is therefore not visible in this section. Two surface wave arrivals are clearly visible, propagating at velocities of 135 m/s and 250 m/s. I interpret these as two modes of a Rayleigh wave generated by the Betsy gun source.

Figure 2.13(c) is an estimate of the pitch component resulting from differencing the two adjacent vertical geophones in the inline direction (Eq. 2.4) at station 1 (refer to Figure 2.9(a)). I compare the data in this figure to the rotation-sensors' pitch component shown in Figure 2.13(d). Observe that both sections show the same arrivals with similar maximum amplitudes of up to 0.2 mrad/s. However, the weaker Rayleigh-wave arrival appears to have been better acquired by geophone differencing. For the larger offsets, the rotational amplitudes from geophone differencing are about twice as great as the ones recorded by the rotation sensors. This indicates that the geophones have a greater dynamic range than the rotation sensors. However, all I needed the geophones for was to validate the phase response of the rotation sensors, therefore their amplitude response was of secondary importance.

I expect the pitch rotational component to be dominant for the Rayleigh wave propagating in the inline direction in this 2D survey, since the rotational deformation that a Rayleigh wave generates is perpendicular to its propagation direction, i.e., rotation around the crossline 'Y' axis.

The phase comparison between the pitch calculated by geophone differencing and the pitch measured by the rotation sensor is shown in Figure 2.14(a). There seems to be no drastic phase difference between the signals at all 3 stations for the pitch component.

Figure 2.13(e) is the roll component estimated by differencing the two adjacent vertical geophones in the crossline direction (Eq. 2.4) at station 1. This figure should be compared the rotation-sensor roll component in Figure 2.13(f). Note again the similarity in amplitudes. The roll estimated from geophone differencing appears slightly more coherent than the roll from the rotation sensor.

Compared to the pitch component, the roll component is weaker, and appears

less coherent. This is again in accordance with the rotational deformation we would expect the Rayleigh wave to generate in this survey, i.e., very little rotation around the inline axis.

Figure 2.14(b) shows that we are unable to obtain a consistent phase difference between the roll from geophone differencing and the roll from the rotation sensors for the 3 receiver stations. I attribute this to the fact that the roll signal is indeed very weak, and therefore SNR is low. Consequenctly, discerning the phase difference for the ground roll between these two different measurements of the roll component is difficult.

Figure 2.13(b) is the yaw component of the rotation sensor at station 1. Note that it exhibits an arrival with the same moveout as the Rayleigh wave arrival on the pitch component. Like the roll component, the yaw is much weaker than the pitch signal.

Principally speaking, the yaw component should record Love wave modes. However, both Rayleigh and Love wave modes can be excited by surface sources, and these data have very short offsets making it difficult to identify different modes of surface waves by their respective moveout. Therefore, the surface wave arrivals seen in these data may be a mixture of Love and Rayleigh wave modes. I cannot compare the rotation-sensor's yaw component to the yaw estimated from geophone differencing, since that would require differencing horizontal geophones which we did not deploy in this survey.

The only reliable phase difference we have is for the pitch component (Figure 2.14(a)), which does indeed show a flat response for the rotation sensors over the 3-30 Hz frequency range. Though the phase difference is very small, we used it for designature of all rotational components.

Denoising of magnetometer data

In order to reduce the ambient magnetotelluric noise from our magnetometer measurements, we deployed a remote 3C magnetometer station at a distance of about 1 km from our shooting location. The ambient magnetotelluric field varies very little within such a distance, and I had intended to use the seismic-free measurements from the remote station in order to subtract the ambient magnetic noise from the

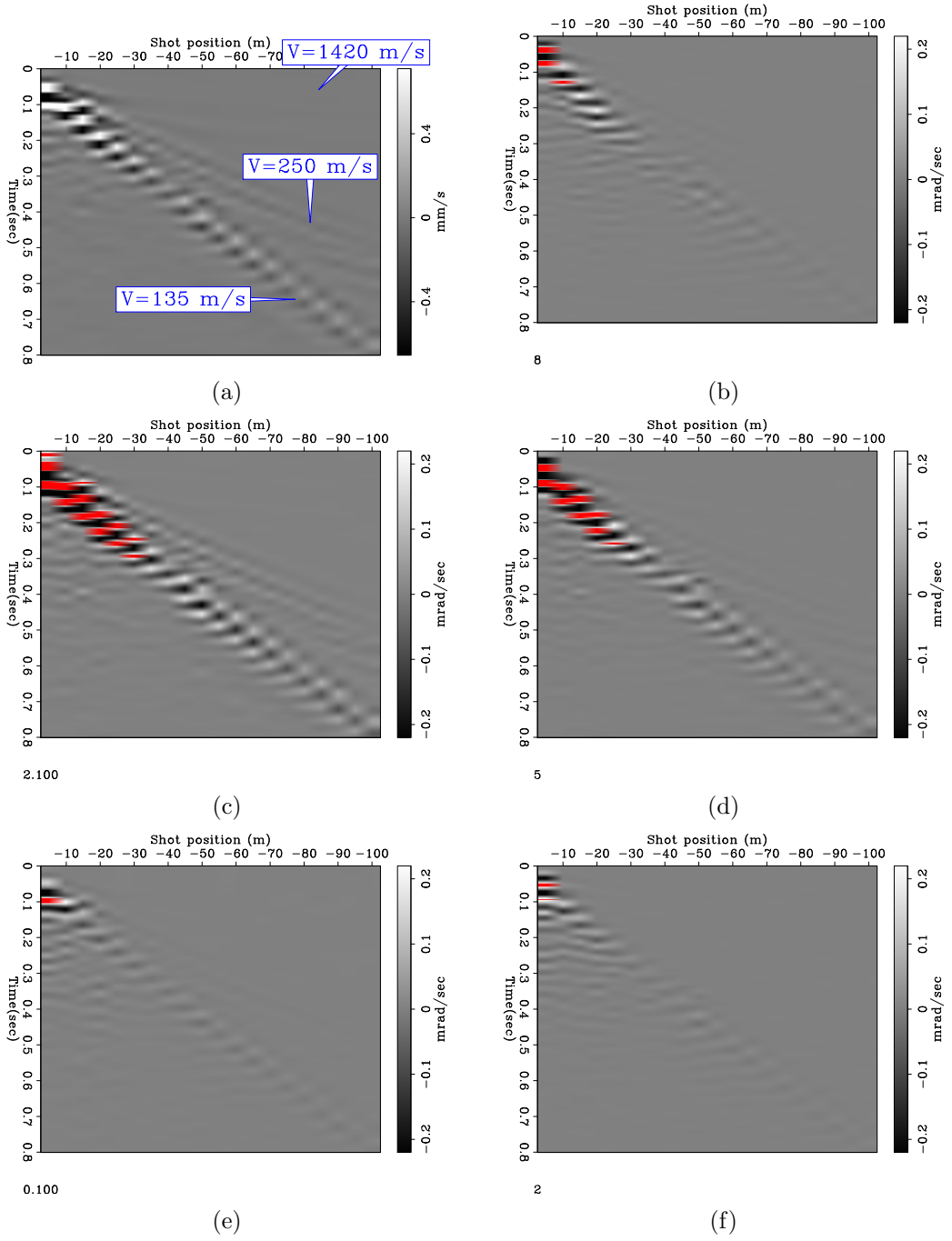

Figure 2.13: Silver Lake receiver gathers at station 1, in the 5 - 30 Hz frequency band. (a) Vertical geophone. (b) Yaw rotation sensor. (c) Inline vertical geophone difference, which estimates the pitch component. (d) Pitch rotation sensor. (e) Crossline vertical geophone difference, which estimates the roll component. (f) Roll rotation sensor. Clipped values are indicated in red. The direct wave propagating at V=1420 m/sec is very weak and cannot be seen at this clip level. There are two strong Rayleigh wave modes propagating at V=135 m/sec and V=250 m/sec. These are present as rotations measured by geophone-differencing and by the rotations sensors themselves. The amplitudes of the rotations calculated by geophone differencing are greater than those measured by the rotation sensors. [**ER**]

chap2/. vz-1-ann,rsn-1rz,geodiff-1ry,rsn-1ry,geodiff-1rx,rsn-1rx

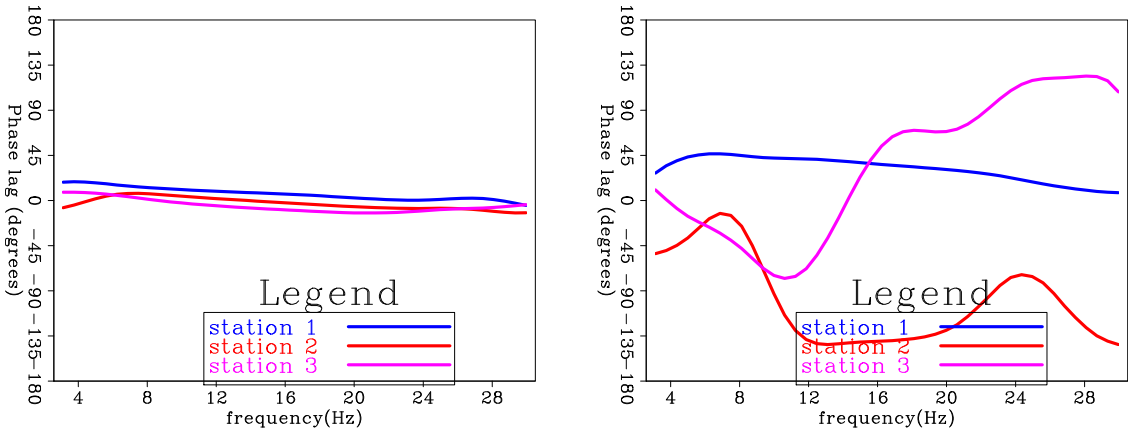

Figure 2.14: The phase difference between the rotations estimated from vertical geophone differencing and the rotations from the rotation sensors, within the passband. (a) Phase difference for the pitch component. (b) Phase difference for the roll component. Observe that for the roll we do not get a consistent phase difference for the 3 composite stations. There is not much energy on the roll component, therefore the signal to noise ratio is low and it is difficult to estimate the phase difference reliably for all stations. Also, I could not get an estimation of the yaw component from geophone differencing. Therefore, I designatured the rotation-sensors' pitch, roll and yaw components using the pitch phase difference, which appeared to be reliable across stations. [**ER**] chap2/. ry-phasediffs,rx-phasediffs

active-seismic magnetometers.

Figures 2.15(a), 2.15(d) and 2.15(g) are the magnetometer receiver gather data recorded at station 1. The data are designatured, and therefore are in terms of nanoTeslas of deviation of the projection of the ambient magnetic field on the magnetometer components.

Note that the signal is stronger on the X (inline) and Z (vertical) components, while the Y (crossline) component is the weakest. This is as we would expect given that the Rayleigh wave's rotation is mostly around the Y axis. As a result of a rotation around the Y axis, the X and Z antennas should record a change in projection of the Earth's constant magnetic field.

Figures 2.15(b), 2.15(e) and 2.15(h) are the X, Y and Z magnetometer data recorded at the remote station. These data do not contain any of the magnetic rotation signal generated by the seismic wave, as they are too far away from the shooting location, but they do contain the same magnetotelluric noise as the active seismic magnetometers. Note the similarity between the remote station's and active station's X and Y components before the arrival of the ground-roll.

Note, however, that the vertical magnetometer antenna at this remote station (Figure 2.15(h)) had an electronic fault, and therefore recorded much more noise than was actually in the field. Consequently, subtracting this noise results in even noisier data, as shown in 2.15(i). I therefore decided to use the original noisy Z magnetometer data in Figure 2.15(g). This had a deleterious effect on the pitch and roll rotational components derived from the magnetometer data, which is discussed in the following section. There was no effect on the yaw component, however, since yaw rotations do not affect the vertical projection of the magnetic field on the magnetometers.

Figures 2.15(c) and 2.15(f) are the X and Y magnetometer data at station 1 after subtracting the noise recorded by the remote stations' X and Y magnetometers, and I used these data for the rest of the analysis.

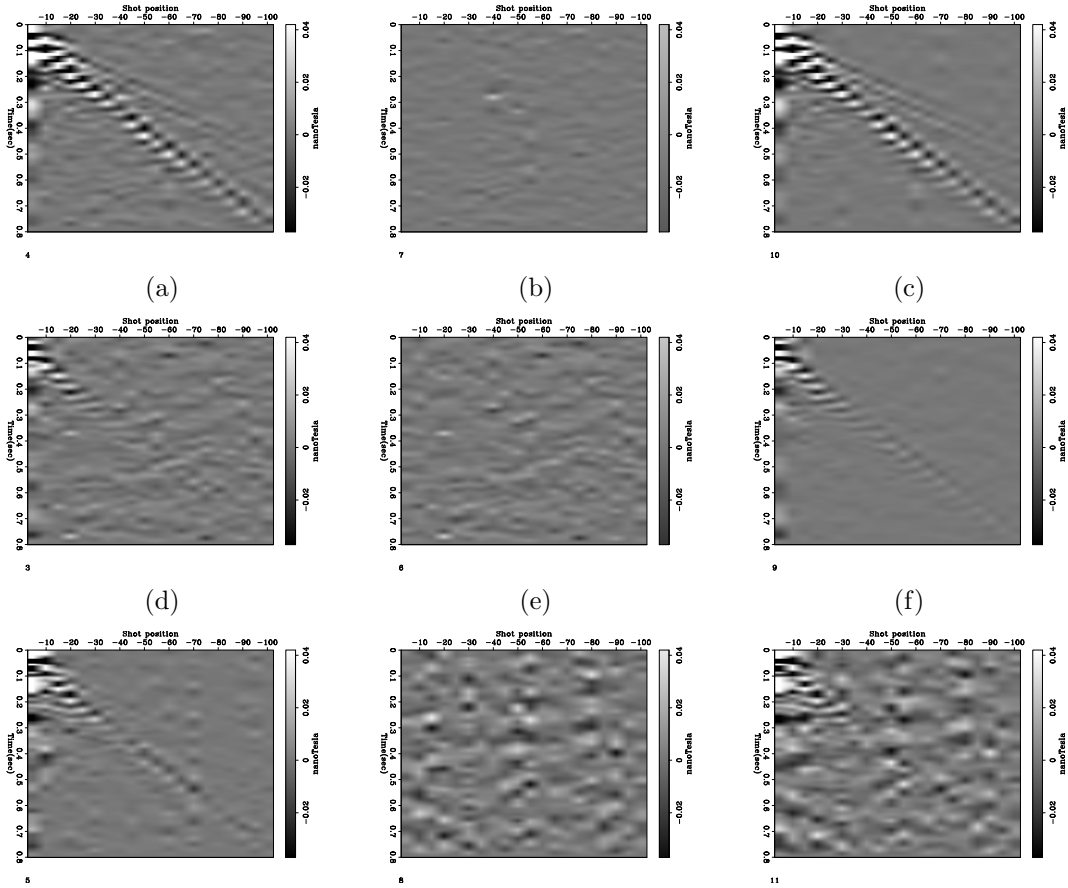

Figure 2.15: Magnetometer receiver gather at station 1 after designature of the ICMs, before and after removal of the MT field acquired by the remote station. (a) X component. (b) X component of remote station. (c) X component after subtraction of MT field acquired by remote station. (d) Y component. (e) Y component of remote station. (f) Y component after subtraction of MT field acquired by remote station. (g) Z component. (h) Z component of remote station. (i) Z component after subtraction of MT field acquired by remote station. Note that we had instrument problems with the Z component of the remote station (h), and therefore subtracting the MT noise from the Z component produced noisier data than the original. Consequently, for further analysis I used the data shown in (g) rather than the data shown in (i). Note that these data are after application of a bandpass filter between 5 Hz and 30 Hz. [**ER**] chap2/. 215a,215b,215c,215d,215e,215f,215g,215h,215i

Reverse mapping: Conversion from magnetometer deviations to rotations

The pitch rotation is effectively recorded as deviations of the projections of the Earth's magnetic field on the X and Z magnetometers, the roll on the Y and Z magnetometers, and the yaw on the X and Y magnetometers. The changes in projections are on the order of microTeslas. In order to derive rotations from these changes in projections I use equations 2.5 to 2.19. These equations represent the reverse mapping operator $\mathbf{L}$, which maps magnetic projection deviations to an estimated model of rotations: $\hat{\mathbf{m}} = \mathbf{Ld}$. I then compare the magnetometer-derived rotations to the rotation-sensor data, which I treat as the "true" model of seismic rotations.

Figure 2.16(a) is the receiver gather of the pitch rotations derived from the magnetometer data at station 1. Compare this with Figure 2.16(b), which shows the rotations measured by the pitch rotation sensor at the same station. In both figures we observe the two strong Rayleigh-wave arrivals. However, the rotations derived from the magnetometers are slightly weaker, and the phase is different. Also, note the higher level of noise in Figure 2.16(a). This noise is the result of the unattenuated ambient MT noise on the vertical magnetometer, which leaks into the derived pitch rotations.

The most significant difference between the pitch component recorded by the rotation sensors and the pitch derived from the magnetometers is the phase of the arrivals. This is more obvious in Figure 2.17(a), which shows a wiggle-trace comparison of the magnetometer-derived pitch component vs the pitch measured by the rotation sensors. Figure 2.17(b) is the average phase difference between the magnetometer-derived pitch and the rotation-sensor's pitch. It shows that within the frequency band of 5 Hz - 30 Hz there is a phase difference between 150^o and 90^o.

The comparison between the magnetometer-derived roll and the rotation-sensor's roll is shown in Figures 2.16(c) and 2.16(d). As previously mentioned, we expect the roll component to have the least energy in this survey, and indeed the magnetometer-derived roll is just discernable above the noise. Just as is the case for the magnetometer-derived pitch component, the noise on the magnetometer-derived roll is the result of the ambient MT noise on the vertical magnetometer.

Figure 2.17(c) shows a wiggle-trace comparison of the roll component at station 1.

The noise is more obvious here than in the pitch component section. Figure 2.17(d) is the average phase difference between the magnetometer-derived roll and rotation-sensor roll. Unlike the pitch component, the phase difference is inconsistent between stations and shows great variability between 90^o and -90^o. Since the roll signal is weak, the noise is relatively stronger making it more difficult to draw conclusions from the phase differences for this component.

Ideally, we would have crossline shots in the survey which would have generated a strong rotational signal on the roll components. However, time constraints in the field did not enable us to include crossline shots in this survey.

Figures 2.16(e) and 2.16(f) compare the magnetometer-derived yaw to the rotation-sensor yaw. Since I was able to remove the ambient MT noise from the X and Y magnetometer antennas, the magnetometer-derived yaw has the least noise of the magnetometer rotations. The earlier, weaker Rayleigh-wave arrival is actually clearer on the magnetometer-derived yaw section than on the rotation-sensor section.

In terms of phase, the difference between the yaw rotations of the magnetometers and that of the rotation sensors is the smallest. Figure 2.17(f) shows that there is a consistent phase difference of between 90^o and 45^o between the stations.

Converting estimated rotations to magnetic projections

By forward-modeling with the estimated model of rotations from the magnetic projection data, we can indirectly observe the effect of the null space, i.e., the rotations around the ambient magnetic field that do not generate a change in the projection of the magnetic field on the ICM components, and are therefore not recorded.

I apply the forward-modeling operator in equations 2.11 and 2.12 to the rotation estimated by the reverse mapping operator: $\mathbf{d}_{\text{est}} = \mathbf{F}\hat{\mathbf{m}} = \mathbf{FLd}$. As I mentioned before, please note that the operators $\mathbf{F}$ and $\mathbf{L}$ are not an adjoint pair. I compare the forward-modeled magnetometer deviations to the recorded magnetometer data. In a noise-free environment, the magnetic-deviation data estimated from the magnetometer-derived rotations will be identical to the recorded magnetometer data.

Figure 2.18(a) is the comparison of the forward-modeled 'X' magnetometer component vs the recorded one. We see that the signals are very similar in phase. The

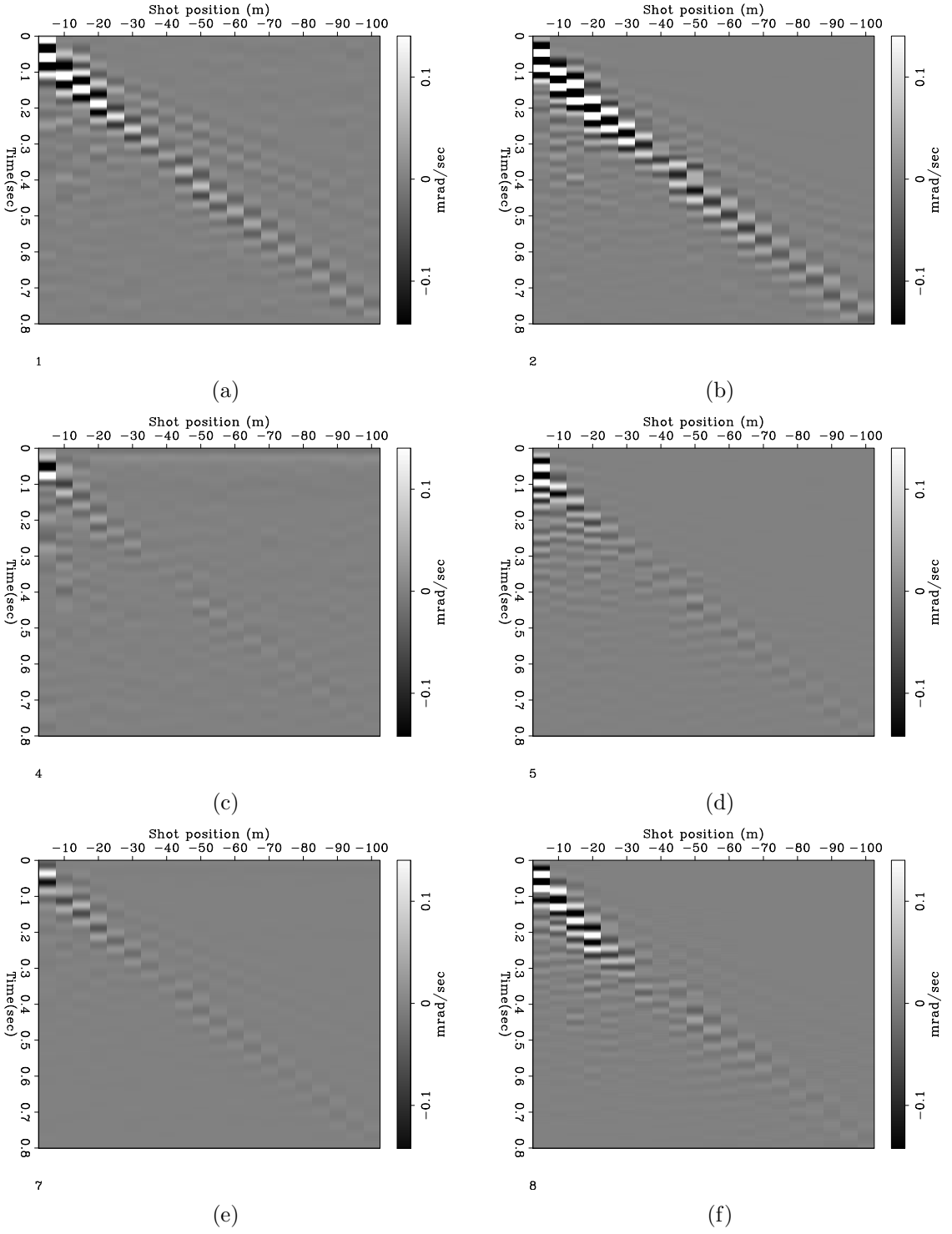

Figure 2.16: Comparison of rotations derived from ICMs to rotations measured by rotation sensors. (a) Pitch derived from ICM. (b) Pitch measured by rotation sensor. (c) Roll derived from ICM. (d) Roll measured by rotation sensor. (e) Yaw derived from ICM. (f) Yaw measured by rotation sensor. Note the similarity in amplitudes of the Rayleigh-wave arrivals between the magnetometer-derived rotations and those measured by the rotation sensor. Also, note the large phase difference of the pitch component. [**ER**] chap2/. 216a,216b,216c,216d,216e,216f

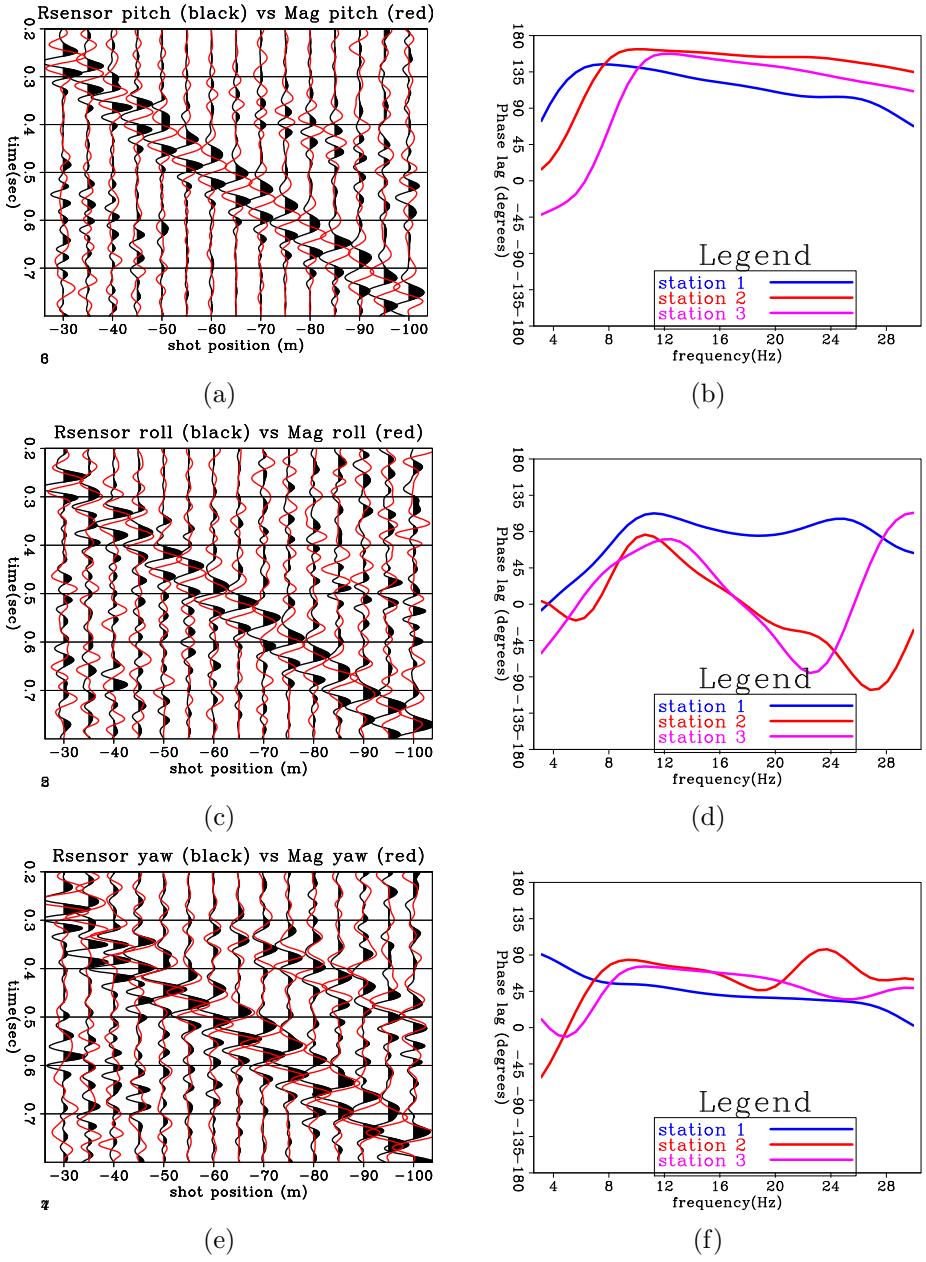

Figure 2.17: Comparison of the rotations measured by rotation sensors (red wiggles) and rotations derived from ICM components (black wiggles). (a), (c) and (e) are the data comparison for station 1 for the pitch, roll and yaw components, respectively. AGC has been applied for display. (b), (d) and (f) are the averaged phase difference between the two signals for all 3 receiver stations. The roll rotational signal is very weak (see Figure 2.16(d)), and the low signal to noise ratio causes the phase difference to be inconsistent across stations for the roll component. [**ER**]

chap2/. 217a,217b,217c,217d,217e,217f

magnetic projection deviations on the 'X' component are the result of the pitch ('Y') and yaw ('Z') rotations. The pitch rotation is the dominant one in the data. Additionally, the 'X' magnetometer component is well-coupled to the field for rotations around the 'Y' axis, as it is nearly orthogonal to the magnetic field. Therefore, the SNR on this component is good, and we see a nearly no phase difference between the recorded and the estimated data.

Figure 2.18(c) shows the comparison between the forward-modeled and the recorded 'Y' magnetometer component. We observe an inconsistent phase shift between the signals. The magnetic projection deviations on the 'Y' component are the result of the roll ('X') and yaw ('Z') rotations, which are weak in this dataset and therefore have low SNR. Another contribution to the low SNR is the noisy magnetometer 'Z' component. Additionally, the magnetometer 'Y' component is not well coupled (i.e., not orthogonal) to the magnetic field for rotations around the 'X' axis.

The same reasoning applies to the inconsistent phase difference we observe for the 'Z' magnetometer component in Figure 2.18(e). The magnetic projection deviations on the 'Z' component are the result of the roll ('X') and pitch ('Y') rotations. Though the pitch rotational component is strong, recall that the magnetometer 'Z' component is contaminated with ambient EM noise. This means that the noise from the magnetometer 'Z' component goes into the estimated rotational models of the roll and pitch components. Mapping this noise back to the magnetic-deviation data domain is the reason for the jittery phase differences seen in Figure 2.18(f).

Interpretation of results

Though the results clearly show that both the magnetometers and the rotation sensors are indeed recording seismic energy, the amplitudes and phases of the rotations recorded by the rotation sensors and those derived from the magnetometers are not identical.

The rotational energy of the magnetometer-derived rotations is approximately 25% lower than that of the rotation sensors. I attribute this difference to the rotations around the Earth's ambient magnetic field's axis; the projection null-space effect shown in Figure 2.8(f). The rotation does not need to be perfectly parallel to the magnetic field's axis in order for the projection's null space to affect the measurements.

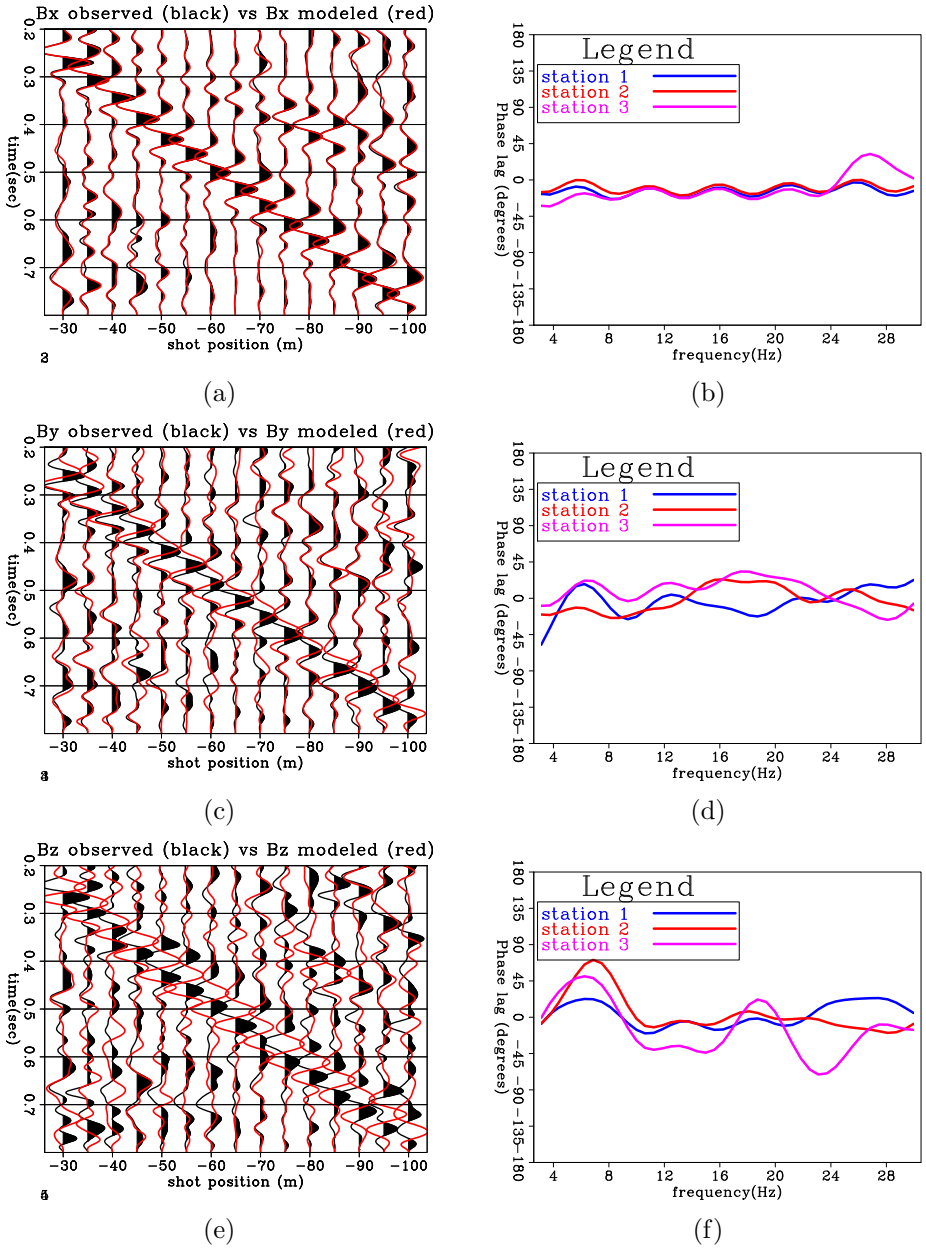

Figure 2.18: Comparison of the recorded magnetometer data (black wiggles) to forward-modeled magnetic projections (red wiggles) derived from the magnetometer rotations. (a), (c) and (e) are the data comparison for station 1 for the B_x, B_z and B_y components, respectively. AGC has been applied for display. (b), (d) and (f) are the averaged phase difference between the two signals for all 3 receiver stations. Recall that I could not remove the ambient magnetic noise from the 'Z' magnetometer component, which is why it so much noisier than the other two components. [**ER**]
chap2/. 218a,218b,218c,218d,218e,218f

If the axis of rotation has a projection on the axis of the magnetic field, then invariably some of the resulting magnetic projections will be insensitive to the rotations. The effect of the null space is evident when I apply the forward-modeling operator **F** to the rotational model derived from the reverse-mapping operator **L** applied to the magnetic deviations.

In the case of the Silver Lake survey, we had aligned the shot line and magnetometer receiver components so that the expected axis of the strongest rotation generated by the Rayleigh wave (pitch) would not coincide with the axis of the magnetic field. As shown in Figure 2.9(b), the horizontal 'Y' and 'X' magnetometers were aligned in along magnetic azimuths 30^o and 120^o, respectively, while the vertical magnetometer pointed down. The inclination of the ambient magnetic field at Silver Lake was 60^o at the time of the survey. The shot line was also done along magnetic azimuth 120^o. Therefore, neither pitch, roll or yaw components were directly around the ambient magnetic field. However, we observe rotations on all components of the seismic rotation sensors, indicating that at least some of the rotations did indeed occur around the magnetic field's axis, leading to a loss of amplitude in the magnetometer-derived rotations.

I attribute the large differences in phase of the pitch component to the null-space issue, since the phase differences appear consistent between receiver stations and along the offset axis. However, the (non-seismic) noise from the vertical magnetometer component necessarily contributed to the rotational signal derived for the perpendicular pitch and the roll components. The case is worse for the roll component, since it has a very low signal to noise ratio to begin with.

We see the smallest phase difference between the two types of rotational measurements for the yaw component. This is partly due to the yaw rotations being well coupled to the magnetic field. It is also due to the yaw component being mostly derived from the magnetic deviations on the X and Y magnetometer components, which I was able to denoise using the remote station's data.

DISCUSSION AND CONCLUSIONS

There are currently very few field-deployable seismic rotation sensors, and none designed for use on the ocean-bottom. Therefore, I presented a methodology for deriving seismic rotations from changes in projection of the Earth's ambient magnetic field on 3-component induction-coil magnetometers (ICMs). These magnetometers are currently being used for magnetotelluric (MT) and controlled-source electromagnetic (CSEM) surveys. The most significant advantage they have over other, existing rotation-sensing technology is that they are an existing solution, currently available, familiar to the applied geophysics community and are field-deployable in both land and marine environments.

The Silver Lake survey shows that, in principle, it is possible to derive rotations from magnetometer data. However, there are limitations to the methodology.

The first challenge is to remove the magnetotelluric ambient noise from the ICM data in order to acquire only the magnetic deviations resulting from the seismic energy. In the Silver Lake survey, we used a remote station to record and remove the ambient MT noise from the active-seismic data.

It follows then that the scenario best suited for recording seismic rotations with magnetometers is the ocean bottom, where the ambient EM noise is much lower than on land. Additionally, considering the cost of deployment of an ocean-bottom node, it is economically desirable to derive as much independent information as possible from the seismic wavefield per receiver deployment.

The most critical challenge, however, is the null space of projections: since the method relies on changes in projection of the Earth's ambient magnetic field on the ICM components, any rotation that occurs around the magnetic field's axis will not be recorded. This will cause the derived rotational amplitudes to be lower than the true seismic rotations.

We cannot predict a priori the axis of rotation of seismic waves, therefore the solution to this problem would not involve a particular orientation of the 3C ICM. Instead, I have considered addressing this issue with an inversion.

Inverting for rotations in the null space of magnetic projections

The forward operator maps rotations to magnetic projections. The reverse-mapping operator maps magnetic projections to rotations. It is possible, therefore, to invert for the rotations that are in the null space.

The inversion would attempt to recover the missing rotational energy by using the collocated 3C geophone data. For example, we expect Rayleigh waves to generate strong rotations. Therefore, if we observe strong Rayleigh waves on the geophone components, but weak Rayleigh waves on the magnetometer-derived rotational components, we may deduce that the axis of rotation is close to that of the ambient magnetic field.

What is required then is a model that provides an expectation of the total rad/sec of rotation for a certain total of m/sec of particle velocity, for the different types of seismic waves (P, S, surface). We may also use the phase of the transverse geophone as a model for the phase to expect on the yaw component (Igel et al., b).

The objective function would try to find the model of rotations that match the recorded magnetometer data, and would also have a regularization term that attempts to maximize the rotational amplitudes. The regularization term would be constrained by the amplitudes of the geophone data. The inversion would effectively attempt to recreate the rotations missing from the ICM recording.

ACKNOWLEDGEMENTS

This work was done in conjunction with the Scripp's Marine EM lab, and I would like to thank Prof. Kerry Key, Prof. Steven Constable and their students for all the work they did in bringing the Silver Lake field experiment to fruition. I also thank the sponsors of the Seafloor Electromagnetic Methods Consortium. Dr. Shuki Ronen rode his motorcycle all the way down California to volunteer his assistance and experience in running field surveys. The rotations sensors used in the field experiment were donated to us by Geokinetics, and I thank John Archer and Patrycjusz Bachelda for preparing the sensors for our use. The Silver Lake survey was funded in part by the Stanford School of Earth Science Mcgee-Levorsen research grant.

Chapter 3

Wave-mode separation with translations and rotations

The previous chapter discussed various ways to record rotational data. In this chapter, I show how to use combined multicomponent translational and rotational data to identify and separate particular wave modes, including P, S, Rayleigh and Love waves. I develop a polarization filter in the continuous wavelet domain in order to identify and subsequently separate shear and surface wave modes from P wave modes. The method does not rely on spatial continuity of events, and can therefore be applied to spatially aliased data. I apply the method to a 2D 6C dataset acquired by Chevron near Kettleman in California, which included collocated 3C geophones and 3C electrokinetic "R2" rotation sensors.

INTRODUCTION

The simplest model available for representing the Earth is the acoustic model, and this representation has served the seismic industry for most of its existence. In the acoustic model, the data are P-wave reflections from interfaces in the Earth where P impedance varies. Surface waves are an elastic phenomena that occurs on interfaces between media, and are not supported by the acoustic wave-propagation model. Neither are shear waves. Furthermore, surface waves do not contain information about the deep subsurface where resources are to be found. There are existing processing flows for converted shear waves (i.e., P waves that were converted to S waves at the reflectors)

and for shear sources, but these methods assume that the shear reflections can be separated from the rest of the data. Therefore, in conventional seismic processing, surface waves and shear waves appearing on the vertical component are considered to be noise, and must be removed from the data prior to the standard seismic processing steps that consider only P waves. P waves also provide information on Vp/Vs ratio, and this is done in practice via AVO analysis (Ostrander, 1984). AVO, however, still treats surface waves as noise.

Seismic land data is a case in point, where the suppression of surface waves (i.e., ground roll in industry parlance) generated by the seismic source and recovery of broadband P-wave reflections are critical to the subsurface image derived from these data.

One of the original approaches to ground roll suppression was the stack-array method (Anstey, 1986; Morse and Hildebrandt, 1989), which used a summation of source and receiver arrays to preferentially damp surface waves. While robust, the method is more practical for 2D acquisition than for large 3D surveys. Furthermore, large receiver arrays can compromise resolution, both horizontal and also vertical as a result of statics.

With single sensors, industry-standard methods are filtering in the $f-k$ or $\tau-p$ domains, where the combination of moveout and frequency of various waves can be identified. These methods, however, rely on adequate spatial sampling, and are unlikely to work well where this requirement is not met. Since surface waves are inherently slower to propagate than P waves,surveys would need to be designed with shorter receiver intervals to satisfy the spatial sampling requirements not of the data, but of the source-generated noise. While dense spatial sampling may be feasible in the survey inline direction, it is not generally practical in the crossline direction.

Another example of data containing more wave modes than expected is the case of Vz noise in ocean-bottom seismic (OBS) acquisition. In OBS, a hydrophone coupled to the water records the P waves at the water bottom, while a 3C geophone coupled to the ground records both P waves and all other wave modes. The expectation is that only P waves will appear on the vertical geophone, and thus the vertical geophone and the hydrophone data can be combined to separate the upgoing from the downgoing wavefield (Barr and Sanders, 1989; Schalkwijk et al., 2003). The separated upgoing and downgoing data can then be used to generate a subsurface image based on joint

linearized waveform inversion of these two wavefields with minimal crosstalk (Wong et al., 2015).

However, in some receiver stations in OBS surveys, events with a moveout slower than P waves appear on the vertical geophone component. These events have the same moveout as shear waves on the horizontal geophone components. The direct explanation is that the vertical geophone is recording some shear-induced vertical motion. Whatever the cause for the shear energy is, it appears as coherent noise on the vertical geophone component. The so-called "Vz noise" may contaminate the combined hydrophone and geophone data. In addition to degrading the image, this can lead to errors in estimation of the source wavelet, and consequently to inaccurate estimations of medium velocity.

One method of removing the coherent Vz noise is match filtering (Zhou et al., 2011; Craft and Paffenholz, 2007). A $\tau - p$ transform is applied to the vertical geophone and hydrophone receiver gathers, followed by a continuous wavelet transform. The hydrophone represents the true model of P-wave arrivals, Therefore a matching filter is then applied to the transformed vertical geophone gather to match the events in the transformed hydrophone gather.

Edme et al. (2014) use a match filtering methodology for removal of ground roll in multicomponent land data. The radial geophone and rotational pitch components are taken as a model for the ground roll noise, which is then removed from the vertical geophone using match filtering.

The advantage of match filtering vs traditional methods is that they do not, in principle, rely on spatial sampling for their success. However, they do rely on having a model of the coherent noise recorded on a particular data component.

Another class of methods to suppress surface waves is polarization filtering of 3C geophone data, where the relative phases of arrivals on each component are taken into account to identify wave modes. In general, the basic premise of these methods is that different wave modes have distinct polarization patterns. For example, body waves tend to have a linear polarization, while the fundamental mode of surface waves have elliptical polarization. These polarizations can be seen by crossplotting vertical and horizontal data traces.

An advantage of polarization filtering is that it operates solely along the time axis

on a trace by trace basis, and therefore has no dependence on spatial sampling. Since polarization filtering does not rely on spatial continuity, it is unnecessary to apply statics corrections to the data before applying polarization filtering. These attributes make polarization filtering more applicable in 3D surveys, where the crossline direction is usually badly sampled. This filtering method enables the survey design to focus on sampling the signal rather than the noise.

Vidale (1986) applied a Hilbert transform to a 3C geophone trace to calculate the analytic signal. An eigenvalue decomposition (EVD) is applied to the covariance matrix of the analytic signal of each 3C time sample. The eigenvectors are then used to determine the type of polarization present at each time sample. Kendall et al. (2005) applied a similar process, but used Singular Value Decomposition (SVD). They combine neighbouring traces when calculating the instantaneous polarization to increase the signal to (ambient) noise ratio. de Meersman et al. (2006) improve on the identification of polarizations in data with strong isotropic noise, by introducing a noise-weighted multistation approach. Diallo et al. (2006) first apply a Continuous Wavelet Transform (CWT) to the data, and observe the analytic signal in the transformed domain to identify and attenuate frequency-dependent polarizations. Donno et al. (2008) exploit velocity, frequency and polarization characteristics to extend the dimensionality of the data, and thus improve the ability to separate between seismic wave modes based on these characteristics.

SVD and CWT are mathematical tools that can be applied to any data series. In particular, they can be applied to 6C data comprising 3C geophone and 3C rotation sensor data. The resulting polarization vectors indicate not only linear polarization, but also rotational polarization.

I posit that rotational motion is a better indicator of wave modes than are elliptical/linear particle motions, since rotations are medium strains (eq. 1.4), whereas particle displacements are not. Particularly, when considering the different nature of the rotational strains induced by P waves versus shear or surface waves, I would expect to see significant differences in the ratio of translations vs rotations generated by each wave mode. For example, I would expect that for the fundamental mode of a Rayleigh wave, which generates elliptical ground motion and therefore rotational strains, we would see a higher amplitude of rotations per the same total translations than for a P wave which generates mostly linear particle motion and less rotational

strains.

Wave modes may also be differentiated by their frequency bands. One mechanism that can account for this effect is intrinsic attenuation resulting from rock properties. This affects shear waves and surface waves more than it does P waves as a result of the shorter wavelengths that shear and surface waves have. Also, Bale and Stewart (2002) have shown that shear-wave attenuation is stronger than P-wave attenuation. Additionally, scattering caused by the strong heterogeneities typical in the near surface cause an effective attenuation, which will also have a greater effect on the slower shear and surface waves.

Using the singular value decomposition of the continuous wavelet transform of multicomponent translational and rotational data, I combine multiple polarization attributes by which wave modes may be separated. My method differs from the existing polarization analysis methods in that I do not assume an a priori model for the polarization of a particular wave mode. Instead, I learn the polarization of a wave mode from the data themselves.

I apply the method to a field dataset that has both rotational and translational components, and show that it is effective at separating ground-roll and shear waves from the data.

Continuous wavelet transform

The continuous wavelet transform is defined as (Daubechies, 1990):

$$G\left(a,b;g(t),\psi(t)\right)=\int_{-\infty}^{\infty}g(t)\frac{1}{\sqrt{a}}\psi^{*}\left(\frac{t-b}{a}\right)dt, \tag{3.1}$$

where $g(t)$ is the input signal of a particular data component, $\psi(t)$ is a mother wavelet, ψ^{*} is a daughter wavelet, which is the complex conjugate of the mother wavelet stretched by scale a and time-shifted by b. I use the Morlet wavelet as a mother wavelet,

$$\psi(t)=e^{i\omega_0 t}e^{-t^2/2}, \tag{3.2}$$

where ω_0 is frequency.

The continuous wavelet transform effectively shows how correlated a time series

is with a particular daughter wavelet. Since the correlations are done in running time windows (shifted by b), the transform retains the time axis of the data and yet decomposes it to wavelet scales, which are in essence similar to frequency. The result is similar to a Fourier transform. I use the time-frequency decomposition to identify wave modes of particular frequencies that appear at particular times in the data.

Singular value decomposition in the continuous wavelet domain

Singular Value Decomposition (SVD) is based on a linear-algebra theory which states that a rectangular $m \times m$ matrix $\mathbf{D}$ can be decomposed into the product of three matrices - an orthogonal $m \times m$ matrix $\mathbf{U}$, a diagonal $m \times n$ matrix $\mathbf{\Sigma}$, and the transpose of an orthogonal $n \times n$ matrix $\mathbf{V}$:

$$\mathbf{D} = \mathbf{U}\mathbf{\Sigma}\mathbf{V}^T. \tag{3.3}$$

The columns of $\mathbf{U}$ are the orthonormal eigenvectors of $\mathbf{DD^T}$, the columns of $\mathbf{V}$ are the orthonormal eigenvectors of $\mathbf{D^TD}$, and $\mathbf{\Sigma}$ is a diagonal matrix containing the square roots of eigenvalues from $\mathbf{U}$ or $\mathbf{V}$ in descending order.

SVD identifies and orders the dimensions along which the data exhibit the most variation. Since I am dealing with multicomponent time-series data, I refer to these dimensions as polarizations inherent to the input signal. The orthogonal matrix $\mathbf{V}$ effectively contains the polarization vectors of the signal that is present in the data $\mathbf{D}$. The diagonal matrix $\mathbf{\Sigma}$ contains the singular values, which act as a scaling of the polarization vectors. I transpose and multiply the matrix $\mathbf{V}$ by the singular value matrix $\mathbf{\Sigma}$, to obtain the scaled polarization vectors:

$$\mathbf{S} = \mathbf{\Sigma}\mathbf{V}^T. \tag{3.4}$$

To clarify to concept of polarizations in a multicomponent signal, I present the following simple example: Table 3.1 shows three simple datasets, each containing a (very short) time series of two-component data. For dataset 1, the scaled singular vectors (eq. 3.4) are shown in Figure 3.1(a). In this dataset, all the energy is present on the first component, therefore there is only one singular vector aligned along the

first components' axis. The signal is "polarized" along component 1. In dataset 2, all the energy is on the second component, therefore in Figure 3.1(b) we see that signal is polarized only along component 2.

In dataset 3, most of the energy is on component 1, but some energy is present on component 2. Consequently, in Figure 3.1(c), we see that the first singular vector ('S1') indicates that the bulk of the signal is polarized mostly along component 1. The second, smaller polarization vector ('S2') shows that the weaker, orthogonal energy in the signal is polarized mostly along component 2. The signals on the two components in dataset 3 are not orthogonal, but the two polarization vectors are, and both have some projection on each data component axis.

DATA1		Component 1	Component 2
	sample 1	1	0
	sample 2	-0.2	0
DATA2			
	sample 1	0	0.2
	sample 2	0	0.6
DATA3			
	sample 1	1	0.2
	sample 2	-0.2	0.6

Table 3.1: Example two-component input data for SVD.

Polarization template matching

As mentioned before, many existing polarization filtering methods rely on some model of the expected polarization of wave modes on the data components. My approach is to derive the polarization directly from the data. This requires manual picking of an event containing what is obviously an undesired wave mode (In chapter 4 I discuss automation of this selection process).

I either select one multicomponent trace containing the undesired wave mode event, or I move out and stack several traces containing the event to increase SNR. I select the time window from the multicomponent trace that contains a representative sample of the undesired wave mode. I apply CWT (eq. 3.1) to this time window, generating an $N_t \times N_a \times N_c$ cube as shown in Figure 3.2(a), where N_t is the number of

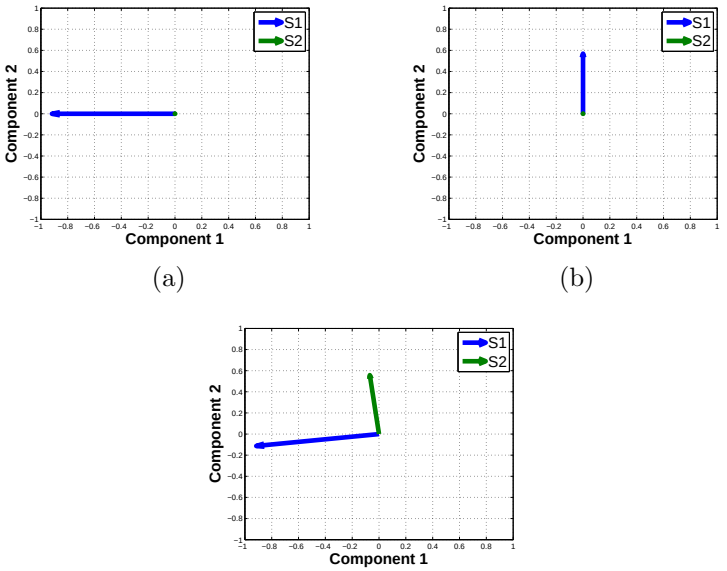

Figure 3.1: The scaled singular vectors (eq. 3.4) of the two-component input data shown in table 3.1. a) data 1. b) data 2. c) data 3. 'S1' and 'S2' indicate the 1st and 2nd singular vectors. [**NR**] chap3/. svec-data1,svec-data2,svec-data3

samples in the time window, N_a is the number of wavelet scales and N_c is the number of data components,

For each time-slice we have a $N_a \times N_c$ matrix. I further subdivide this matrix along the wavelet-scale axis using a sliding window. The data matrix $\mathbf{D}$ to which I apply SVD (eq. 3.3) is then a $N_{a_w} \times N_c$ matrix. I then calculate the polarization vectors for each wavelet-scale window using eq. 3.4, and select only the first polarization vector, as shown in Figures 3.2(b), 3.2(c) and 3.2(d). I then stack the polarization vectors along the time-window N_t to increase SNR, and arrive at the template polarization, as shown in Figure 3.2(e). Since the wavelet scales of the CWT are related to frequency, this polarization template represents the frequency-dependent polarization of the undesired wave mode:

$$\mathbf{S}^{\text{temp}}(\vec{a}) = \mathbf{\Sigma}(\vec{a})\mathbf{V}^T(\vec{a}). \tag{3.5}$$

After determining the polarization template, I now search for similar polarizations in the entire dataset. I run a CWT on the entire multicomponent dataset, generating a data cube $\mathbf{D}(\vec{x}, t, \vec{c}, \vec{a})$, where $\vec{x}$ is trace offset, t is time, $\vec{c}$ is the data component and $\vec{a}$ is the wavelet scale. For each trace offset, each time and each wavelet-scale

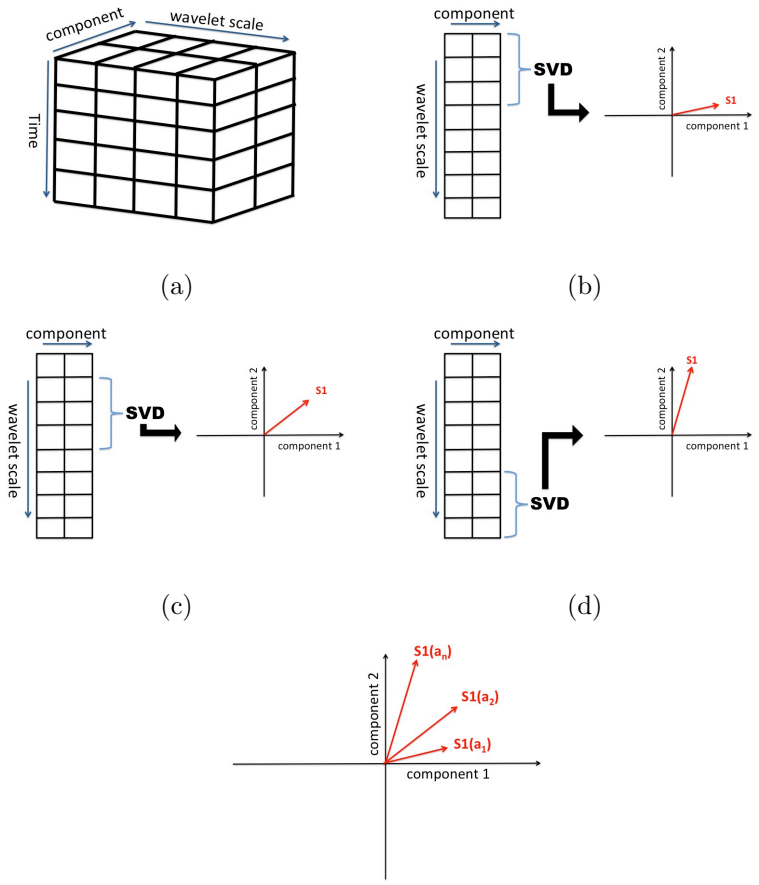

Figure 3.2: a) The cube of data resulting from CWT applied to a single two-component trace, comprising the time axis, the component axis and the wavelet scale axis. b) Application of SVD to a window of wavelet scales of one time slice of the data cube in (a) provides the polarization of the data within that particular wavelet scale range. Since there are two data components, there are two orthogonal polarization vectors (eq. 3.4). The red arrow shows the first polarization vector. c) SVD applied to the next wavelet scale window. d) SVD applied to the last wavelet scale window. e) The wavelet-scale (frequency) dependent polarization template. [**NR**] chap3/. CWT-data-cube,svd-win1,svd-win2,svd-win3,svd-temp

window, I apply an SVD transform to the matrix $\mathbf{D}(\vec{x} = \vec{x}^{\,\prime}, t = t^{\prime}, \vec{c}, \vec{a} = \vec{a}^{\,\prime})$, in which the columns are the data components $\vec{c}$, and the rows are the wavelet scales within $\vec{a}^{\,\prime}$. I then scan the transformed data cube along the offset, time and wavelet-scale axes, searching for where the first polarization vector is similar to the undesired wave mode's polarization template (eq. 3.5). Where I find energy in the offset-time-wavelet scale space for which the first polarization vector is similar to the first polarization vector of the template in eq. 3.5, I attenuate that first polarization vector. I then transform the attenuated data back to the time domain by pre-multiplying by the matrix $\mathbf{U}$, and performing an inverse CWT.

The reasoning for attenuating just the first polarization vector is that it contains most of the energy in $\mathbf{D}(\vec{x} = \vec{x}^{\,\prime}, t = t^{\prime}, \vec{c}, \vec{a} = \vec{a}^{\,\prime})$. Therefore, attenuating the first polarization vector where it is similar to a template of a dominant, undesired wave-mode's polarization should remove most of the energy attributed to that same wave mode at the current offset/time/wavelet-scale in the data. The identification of where and when the data are dominated by undesired wave modes is by human interpretation.

The similarity measure I use is based on the angular difference between the first polarization vector at the current position and wavelet scale in the data $S_1^{\text{curr}}(\vec{x} = \vec{x}^{\,\prime}, t = t^{\prime}, \vec{a} = \vec{a}^{\,\prime})$ and the first polarization vector of the template $S_1^{\text{temp}}(\vec{a})$:

$$\alpha = \cos^{-1}\left(\frac{S_1^{\text{temp}} \cdot S_1^{\text{curr}}}{|S_1^{\text{temp}}|\,|S_1^{\text{curr}}|}\right). \tag{3.6}$$

Attenuation is done by applying a weighting function only to the first singular value of $\mathbf{\Sigma}$ in equation 3.3. The weighting is a function of the similarity of the first polarization vector at $(\vec{x} = \vec{x}^{\,\prime}, t = t^{\prime}, \vec{a} = \vec{a}^{\,\prime})$ to the template polarization vector. It is equal to 1 minus the cosine of the angular difference between the template and current polarization vectors in equation 3.6:

$$w_1 = 1 - \cos^2\left(\frac{\alpha}{\alpha_{\max}}\frac{\pi}{2}\right), \tag{3.7}$$

where $\alpha_{\max}$ is a user-defined parameter which determines the largest angular difference for which the current and the template polarizations are considered to be sufficiently similar. If the angular difference is greater than $\alpha_{\max}$, the weight is set to 1 and the

data are not attenuated. I do not have an a priori method of defining the best $\alpha_{\max}$ parameter for a given dataset, except to say that if it is too big then we may attenuate the data we are interested in retaining, and if it is too small then we will not remove the undesired wave modes. I arrived at the results presented in the following sections by testing several values for $\alpha_{\max}$.

Formally, the weighting is a diagonal matrix $\mathbf{W}$ of the same dimensions as the $\mathbf{\Sigma}$ matrix (i.e., $N_{a_w} \times N_c$). Since I wish to attenuate just the first polarization vector, all the values of the diagonal are 1 except for the first element, which will be in the range $[0, 1]$:

$$\mathbf{W} = \begin{pmatrix} w_1 & 0 & . & 0 \\ 0 & w_2 = 1 & . & 0 \\ . & . & . & 0 \\ 0 & 0 & 0 & w_{N_c} = 1 \end{pmatrix} \tag{3.8}$$

The greater the similarity between the first polarization vector of any sample in the data to the first polarization vector of the template, the lower the value of the first element w_1 on the diagonal of $\mathbf{W}$. Conceivably, the other weights could also be less than 1 if we wish to attenuate the other polarization vectors.

The data are reconstructed with the weighting applied to the first singular vector as:

$$\mathbf{D}(\vec{x} = \vec{x}^{\,\prime}, t = t^{\,\prime}, \vec{c}, \vec{a} = \vec{a}^{\,\prime}) = \mathbf{U}\mathbf{W}\mathbf{\Sigma}\mathbf{V}^T. \tag{3.9}$$

An inverse CWT is then applied to the reconstructed data. Since the method operates independently on each trace and does not rely on any additional spatial considerations, it is effectively insensitive to spatial aliasing in the data.

THE KETTLEMAN SIX-COMPONENT SURVEY

The 2D Kettleman survey was performed by Chevron in December of 2012, and comprised four types of sources:

1. Accelerated weight-drop

2. Vibroseis

3. Dynamite charge at 25 m depth ($\frac{1}{2}$ kg)

4. Dynamite charge at 50 m depth ($\frac{1}{2}$ kg)

There were also multiple types of receivers:

1. 3C GS-One 10 Hz geophones buried at 1 m depth

2. 3C GS-32 10 Hz geophones buried at 3 m depth

3. 3C MEMS Accelerometers on the surface (DSU)

4. 3C Rotation sensors on the surface

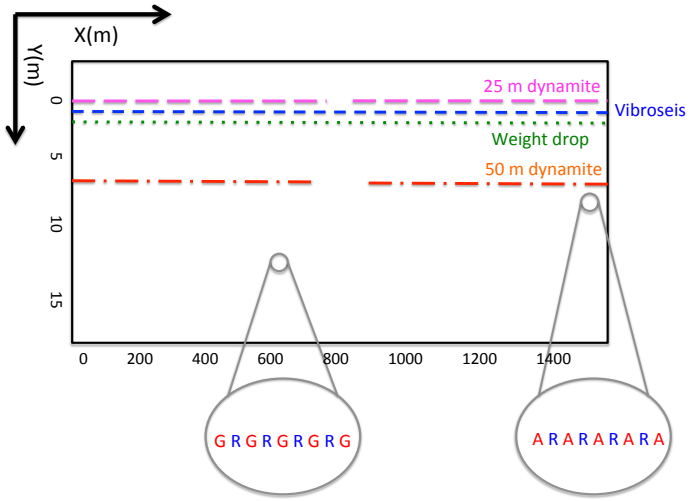

Figure 3.3: Map view of the geometry of the Kettleman survey. Five accelerometers (marked with 'A') were positioned on the surface along the survey's inline azimuth at the end of the shot line, with a 2 meter interval. Five geophones (marked with 'G') were buried near the center of the shot line, also spaced at 2 meter intervals inline. 'R2' rotation sensors (marked with 'R') were placed on the surface in between the accelerometer positions and also in between the geophone positions. There were 241 accelerated weight drop shots, 60 vibroseis shots, 57 of the 25 m depth dynamite shots and 54 of the 50 m depth dynamite shots. [**NR**] chap3/. kettleman-geom-nr

The acquisition geometry is shown in Figure 3.3. The shot line length was 1.6 km long. At one end of the shot line there were five 3C linear accelerometers, which were closely spaced at a 2.1 m interval inline. In between the accelerometers in the inline direction there were four 3C elecrokinetic rotation sensors. The rotational

components were aligned to coincide with the direction of the linear components, so that the positive sense of rotations around the vertical, radial and transverse axes was according to the right-hand rule.

The following figures show the 6C receiver gather for the four source types at one receiver station. Figures 3.4(a)-3.4(f) are accelerated weight-drop data. The weight-drop shots were repeated 6 times at each station, and diversity stacking was applied to the repeated gathers to increase SNR (Gimlin and Smith, 1980). Figures 3.5(a)-3.5(f) are the correlated vibroseis data, Figures 3.6(a)-3.6(f) are 25 m depth dynamite data, and Figures 3.7(a)-3.7(f) are 50 m depth dynamite data. All data are clipped at 93% (i.e., 93rd percentile of absolute amplitude) to enable a comparison between components while still representing the dominance of the surface wave energy compared to the body-wave reflections.

The strong ground roll in the accelerated weight-drop data is not aliased due to a very small shot interval of 6.25 m. All other sources were shot with a 25 m shot interval, and therefore exhibit significant aliasing of the ground roll. The best reflection signal appears on the dynamite data, as it excites less ground roll than surface sources.

However, note how the rotation-sensor data for the dynamite sources in Figures 3.6(d)-3.6(f) and Figures 3.7(d)-3.7(f) have a very low signal to noise ratio as compared to the rotation data generated by the surface sources in Figures 3.4(d)-3.4(f) and Figures 3.5(d)-3.5(f). The reason for this is that most of the strong, rotational signal is generated by surface waves. The buried dynamite sources generate weaker surface waves than surface sources, and as a result of the noise floor level of the electrokinetic rotation sensors, the rotational signal dives into the noise level at shorter offsets. This low SNR would make any multicomponent analysis involving rotational data difficult.

Figures 3.8(a) and 3.8(c) are the pitch component acquired by the rotation sensor for the vibroseis and dynamite sources, respectively. Figures 3.8(b) and 3.8(d) are the pitch component calculated by differencing the two vertical accelerometers adjacent to the rotation sensor (in the inline direction). Note how the pitch component derived from the differencing has a better signal to noise ratio than the rotation-sensor at larger offsets. I therefore opted to use vertical geophone-differencing (eq. 2.4) rather than rely on the pitch rotation sensor data in order to have higher quality rotational

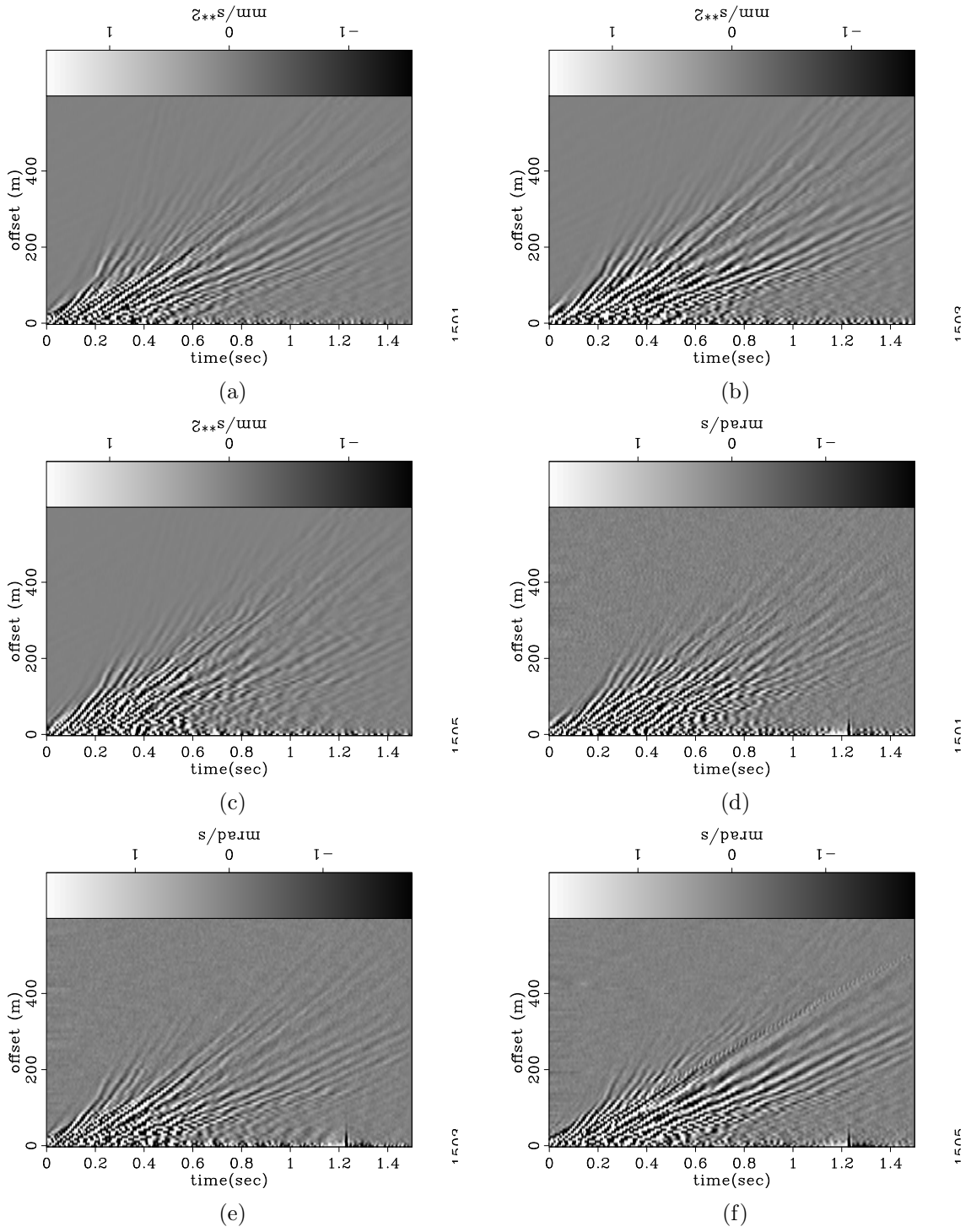

Figure 3.4: 6C receiver gather of the accelerated weight-drop source, clipped at the 93rd percentile. Shot spacing was 6.25 m. Components are: (a) vertical, (b) radial, (c) transverse, (d) yaw, (e) roll, (f) pitch. Six shots were executed at each station, and then diversity stacking was applied to increase the signal to noise ratio. The data observable in these sections at this clip level consist entirely of various Rayleigh wave modes, which are not aliased due to the very close shot spacing. [**ER**]
chap3/. 302a,302b,302c,302d,302e,302f

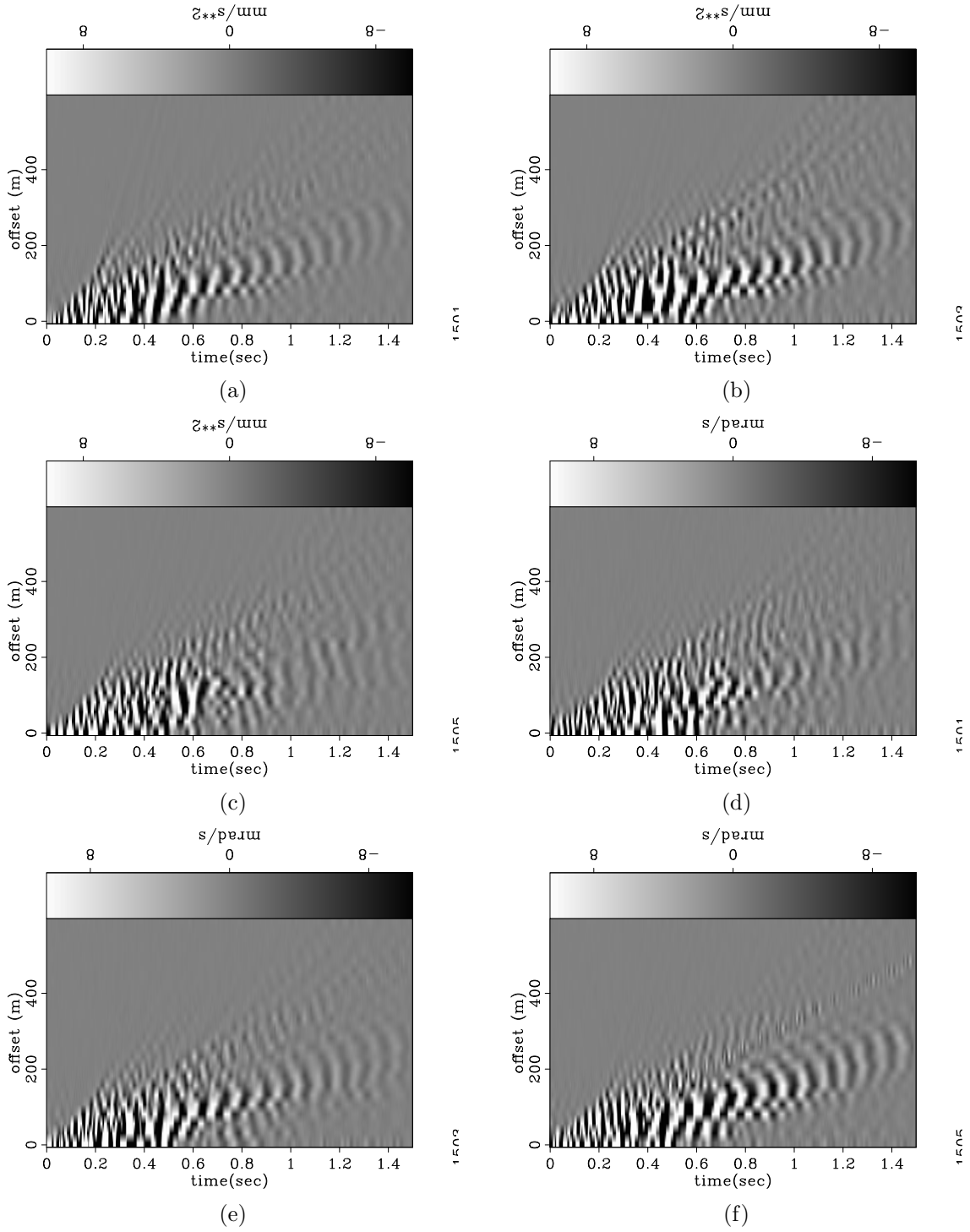

Figure 3.5: 6C receiver gather of the vibroseis source, clipped at the 93rd percentile. Components are: (a) vertical, (b) radial, (c) transverse, (d) yaw, (e) roll, (f) pitch. Shot spacing was 25 m, and so the various Rayleigh wave modes are aliased. Some P-wave reflections are visible at early times on the vertical component. [**ER**]
chap3/. 303a,303b,303c,303d,303e,303f

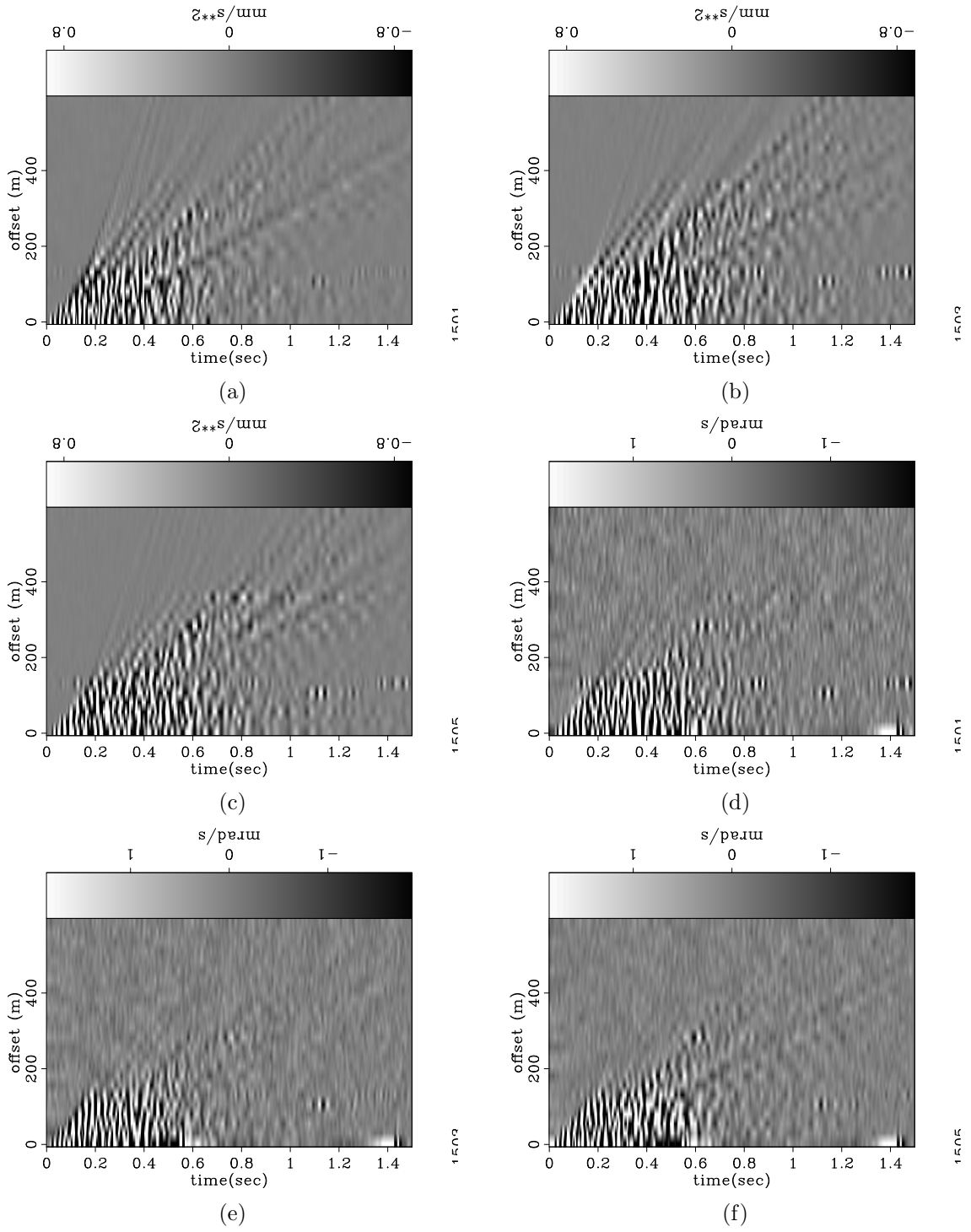

Figure 3.6: 6C receiver gather of the 25 m depth dynamite source, clipped at the 93rd percentile. Shot spacing was 25 m. Components are: (a) vertical, (b) radial, (c) transverse, (d) yaw, (e) roll, (f) pitch. Compared to the accelerated weight drop and vibroseis surface sources, the amount of ground roll in these data is much lower, though aliasing is still very significant. Some reflections are visible at early times from offset 200 m and on. Note how the signal to noise ratio of the rotation-sensor data is low in (d), (e) and (f). [**ER**] chap3/. 304a,304b,304c,304d,304e,304f

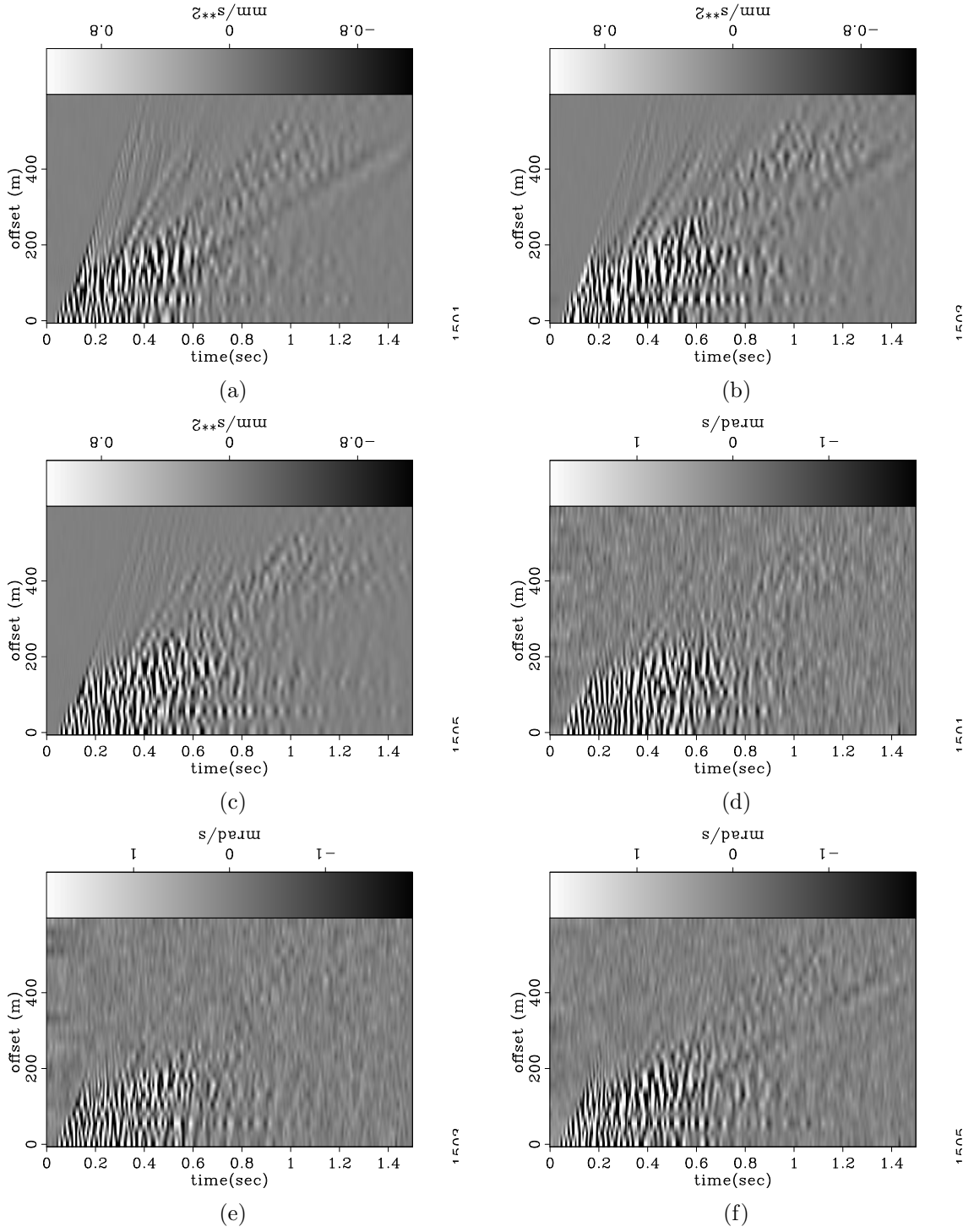

Figure 3.7: 6C receiver gather of the 50 m depth dynamite source, clipped at the 93rd percentile. Shot spacing was 25 m. Components are: (a) vertical, (b) radial, (c) transverse, (d) yaw, (e) roll, (f) pitch. Reflection data are more visible in these sections vs the 25 m depth dynamite source. Note the low-frequency arrival starting from $t = 0.35$ s at offset=200 m, which appears to be shear-induced energy. Again, note the low signal to noise ratio for the rotational data in (d), (e) and (f). [**ER**]
chap3/. 305a,305b,305c,305d,305e,305f

pitch data.

Unfortunately, there were no accelerometers placed in the crossline direction, therefore I was not able to similarly calculate the roll or the yaw rotational components by geophone differencing as in equation 2.4.

DISPERSIVE SURFACE WAVE MODES IN KETTLEMAN DATA

In order to gain a better insight into the observed data, I perform a Radon transform on the accelerated weight-drop source data, which is helpful in identifying frequency dispersion of surface waves. The receiver gathers of these data are well sampled spatially (source spacing was 6.25 m) and therefore are not aliased, facilitating the Radon transform.

The data for the vertical, radial and pitch receiver components are shown in Figures 3.9(a), 3.9(c) and 3.9(e). Note that I have muted out the body wave arrivals, and the remaining data comprise surface waves with a maximum velocity of 600 m/s. I have also applied a circular spreading correction to gain the surface wave data at later arrival times.

The corresponding data in the Radon (ω - p) domain for each of the receiver components are shown in Figures 3.9(b), 3.9(d) and 3.9(f). In the vertical component dispersion image in Figure 3.9(b), a separation of two surface wave modes modes is clearly visible:

1. a slower, low frequency mode, propagating at 220 - 350 m/s and having frequencies between 5 - 15 Hz.

2. a faster, high frequency mode, propagating at 350 - 500 m/s and having frequencies between 16 - 26 Hz.

These surface wave modes are sometimes termed the"fundamental" and the 1st higher mode. For the radial and pitch components in Figures 3.9(d) and 3.9(f) the same two modes are visible, but the slower mode is stronger than the faster mode.

The transverse and yaw receiver components are shown in Figures 3.10(a) and 3.10(c). Their respective Radon-domain dispersion images are in Figures 3.10(b)

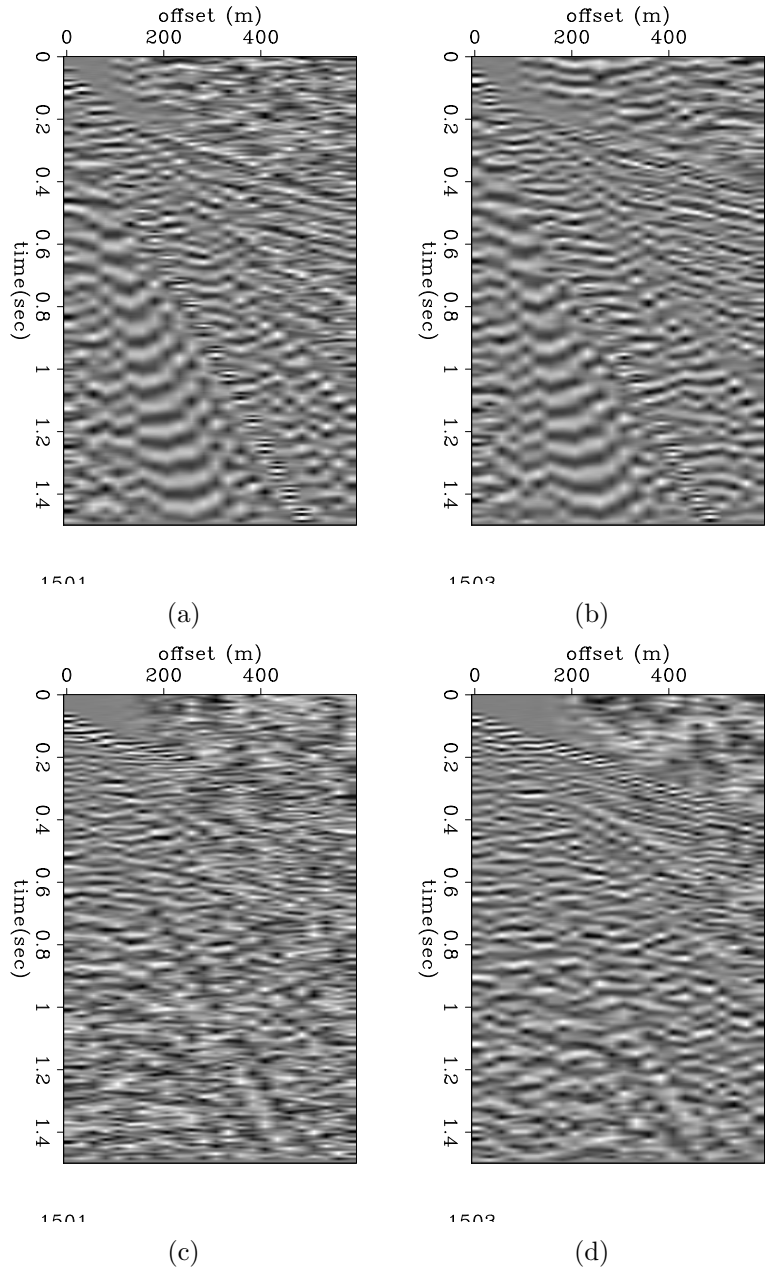

Figure 3.8: Comparison of pitch component acquired by rotation sensor and pitch calculated by differencing adjacent geophones. (a) Rotation sensor pitch for vibroseis source. (b) Geophone-differencing pitch for vibroseis source. (c) Rotation sensor pitch for 50 m depth dynamite source. (d) Geophone-differencing pitch for 50 m depth dynamite source. Note that for both source types, the signal to noise ratio of the pitch derived from geophone differencing is much higher at larger offsets than the pitch measured by the rotation sensor. AGC with a window size of $t = 0.2$ s has been applied to the data for display. [**ER**] chap3/. 306a,306b,306c,306d

and 3.10(d). The transverse component's dispersion image is rather noisy, however I discern the same slower and faster wave modes as for the other data components, with the faster mode being dominant. For the yaw component, the faster wave mode is clearly dominant, and very little of the slower mode is recorded.

Particle motion analysis

Slow surface wave mode

Since the slow surface wave mode appears at frequencies of 5 - 15 Hz, I applied a frequency filter within this range to the data before generating the following figures in this section. Figure 3.11(a) is a wiggle plot of the slow surface wave mode after application of linear moveout (LMO) and AGC for display purposes. The black wiggles are the vertical component, while the red are the radial. The vertical component is delayed compared to the radial. Figure 3.11(b) shows the cross-correlation near zero time-lag for the vertical and radial components, and a consistent 90^o phase shift can be observed for all traces. Figure 3.11(c) shows the phase delay between the vertical and radial components over frequency for the slow ground roll wave mode. Observe that the 90^o phase shift is constant for the frequencies of this slow ground roll.

Figures 3.13(a) and 3.13(e) show the vertical and radial components of one trace of the slow surface wave, and the corresponding hodogram. The red part of the line is the trailing end of the hodogram. Note that the hodogram indicates retrograde particle motion, which is in agreement with the standard model for the fundamental mode of Rayleigh waves where velocity increases with depth in the near surface.

Figures 3.11(d), 3.11(e) and 3.11(f) are the wiggles, correlation lags and phase delays for the vertical and pitch components of the slow surface wave, where the black wiggles are the vertical and the blue are pitch. The phase delay seems to be consistently between 90^o and 45^o degrees. However, in figures 3.11(g), 3.11(h) and 3.11(i), we see that the radial and pitch components are almost completely in phase.

For the transverse (purple) vs the yaw (green) components in Figures 3.11(j), 3.11(k) and 3.11(l), the phase delay appears to be inconsistent between traces and along the frequency axis, going between 90^o and 180^o.

The additional hodograms in Figures 3.13(f), 3.13(g) and 3.13(h) plot rotational vs translational motion, and so, unlike Figure 3.13(e), it is difficult to achieve an intuitive

understanding of the particle motion from them and label them into known categories (e.g., "fundamental mode"). These figures effectively show the same information as in Figures 3.12(f), 3.12(i) and 3.12(l) with respect to the phase delay between components.

Fast surface wave mode

Since the fast surface wave mode appears at frequencies of 16 - 26 Hz, I applied a frequency filter within this range to the data before generating the following figures in this section. Figures 3.12(a), 3.12(b) and 3.12(c) are the wiggle plot, correlation lags and phase delays for the vertical vs the radial component, where the black wiggles are the vertical, and the red are radial. In contrast to the phase delays of these two components for slow surface wave mode, for the fast mode the delay is at most 45^o, and is not as consistent along frequencies.

The particle motion for the fast surface wave mode is retrograde, as can be seen in Figure 3.14(e). Boue et al. (2016) provide a discussion of the theoretical connection between the particle motion sense of the vertical and horizontal components and the velocity model. For some velocity profiles, the 1st higher surface wave mode may have prograde particle motion, however that is not the case here, indicating that the shear velocity structure in Kettleman is a relatively smooth, simple increase with depth.

The phase delays of the vertical vs the pitch component and of the radial vs the pitch component are consistently at 45^o. However, the most significant difference between the slow and the fast surface wave modes can be seen from the comparison of the transverse vs the yaw components. Figures 3.12(k) and 3.12(l) show that the phase delay is close to zero, although not consistently for all traces and frequencies. The same in-phase behaviour of the transverse and yaw can be seen from the trace in Figure 3.14(d) and the hodogram in Figure 3.14(h).

Igel et al. (b) observe a similar direct correlation between the transverse and the yaw components of the Love wave arrivals on a record of the magnitude 8.1 Tokachi-Oki earthquake which occured on September 25th, 2003. The seismic energy from the earthquake was recorded by a large ring laser in Wetzel, Germany, which could only record vertical rotations (yaw), and by a nearby three-component accelerometer. If we consider that Love waves generate horizontal partical motions, we may deduce from the rotation vector in equation 1.5 that a corresponding vertical rotational strain should be observed as well. Assuming the receiver components are oriented so that

the Love wave appears only on the transverse u_y component, we have:

$$\begin{pmatrix} R_x \\ R_y \\ R_z \end{pmatrix} = \frac{1}{2}\nabla \times \begin{pmatrix} 0 \\ u_y \\ 0 \end{pmatrix} = \begin{pmatrix} 0 \\ 0 \\ \frac{1}{2}\frac{\partial u_y}{\partial x} \end{pmatrix} \tag{3.10}$$

Therefore, the fact that we see the transverse and yaw components having the same phase is an indication that at least some of the energy of the faster surface wave mode in these data is the result of a Love wave. The extra information from the rotational yaw component enables a seismic wave-mode determination.

POLARIZATION IN THE CONTINUOUS WAVELET DOMAIN

The objective is to separate wave modes in the data using all components. There are desirable wave modes which we term "signal", and undesirable ones which we call "shot-generated noise". Most commonly in seismic data, the wave modes of interest are the P-wave reflections, as these provide information about the subsurface at depth. Surface waves and shear induced energy appearing on the vertical component are considered to be noise, as they obscure the P-wave reflections.

Figures 3.15(a)-3.15(d) are vertical component receiver gathers for the four source types, after application of NMO to flatten the P-wave reflections. In this display, events that are not close to being flat are considered to be noise, and they prevent us from observing the flattened P waves.

Note the strong ground roll in Figures 3.15(a) and 3.15(b), which prevents us from observing the near-offset reflections (a common issue in seismic land data). It would not be possible to use filters that rely on spatial sampling to remove the ground roll from the vibroseis data because they are aliased. A low-pass filter or an inner mute could be applied to remove all the aliased energy. However, that would result in a significant attenuation of the reflection signal as well as of the noise.

The 50 m depth dynamite source data in Figure 3.15(d) has the best reflection signal. However, observe the non-flat lower frequency arrival starting at $t = 0.3$ s

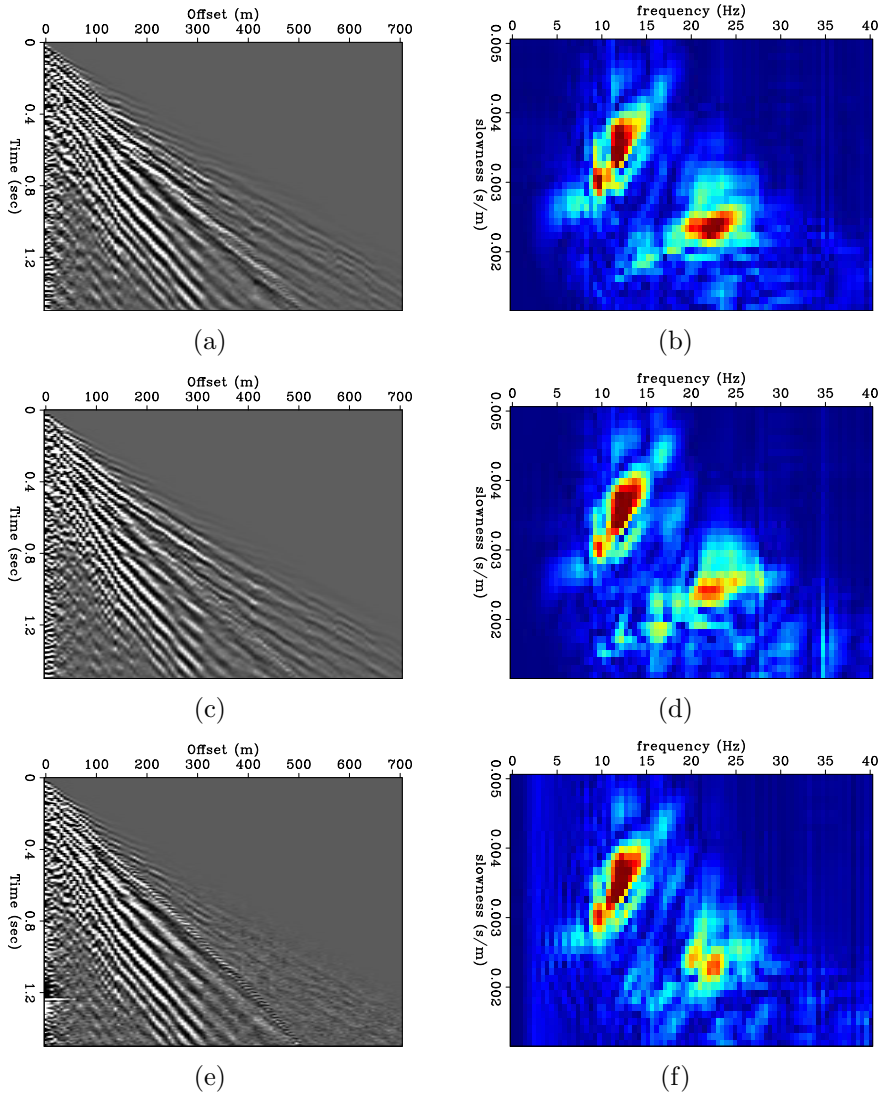

Figure 3.9: Accelerated weight drop source receiver gather at station 335. Mute has been applied to remove the body waves, and circular spreading to gain the later arrival energy. (a) Vertical accelerometer. (b) Vertical accelerometer in Radon domain. (c) Radial accelerometer. (d) Radial accelerometer in Radon domain. (e) Pitch rotation sensor. (f) Pitch rotation sensor in Radon domain. Two distinct wave modes appear on each receiver component: a slower, lower frequency mode, and a faster, higher frequency mode. Note that on the radial and pitch components, the slower surface wave mode is dominant. [**ER**] chap3/. 320a,320b,320c,320d,320e,320f

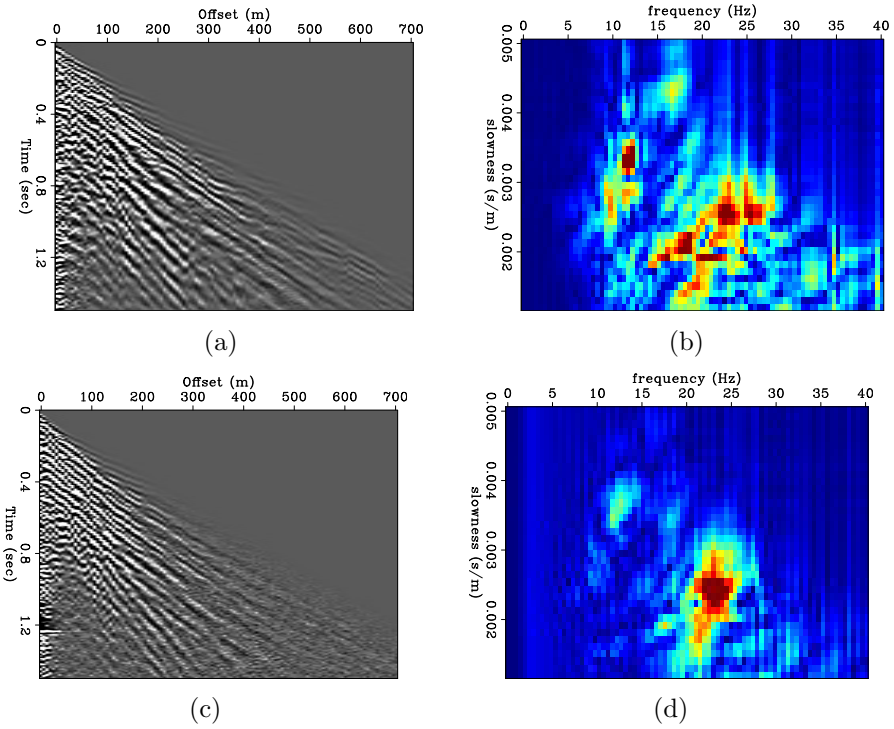

Figure 3.10: Accelerated weight drop source receiver gather at station 335. Mute has been applied to remove the body waves, and circular spreading to gain the later arrival energy. (a) Transverse accelerometer. (b) Transverse accelerometer in Radon domain. (c) Yaw rotation sensor. (d) Yaw rotation sensor in Radon domain. The dispersion image of the transverse component is noisy, but two surface wave modes can still be identified, with the faster mode being dominant. On the yaw component the faster surface wave mode is clearly dominant. [**ER**] chap3/. 321a,321b,321c,321d

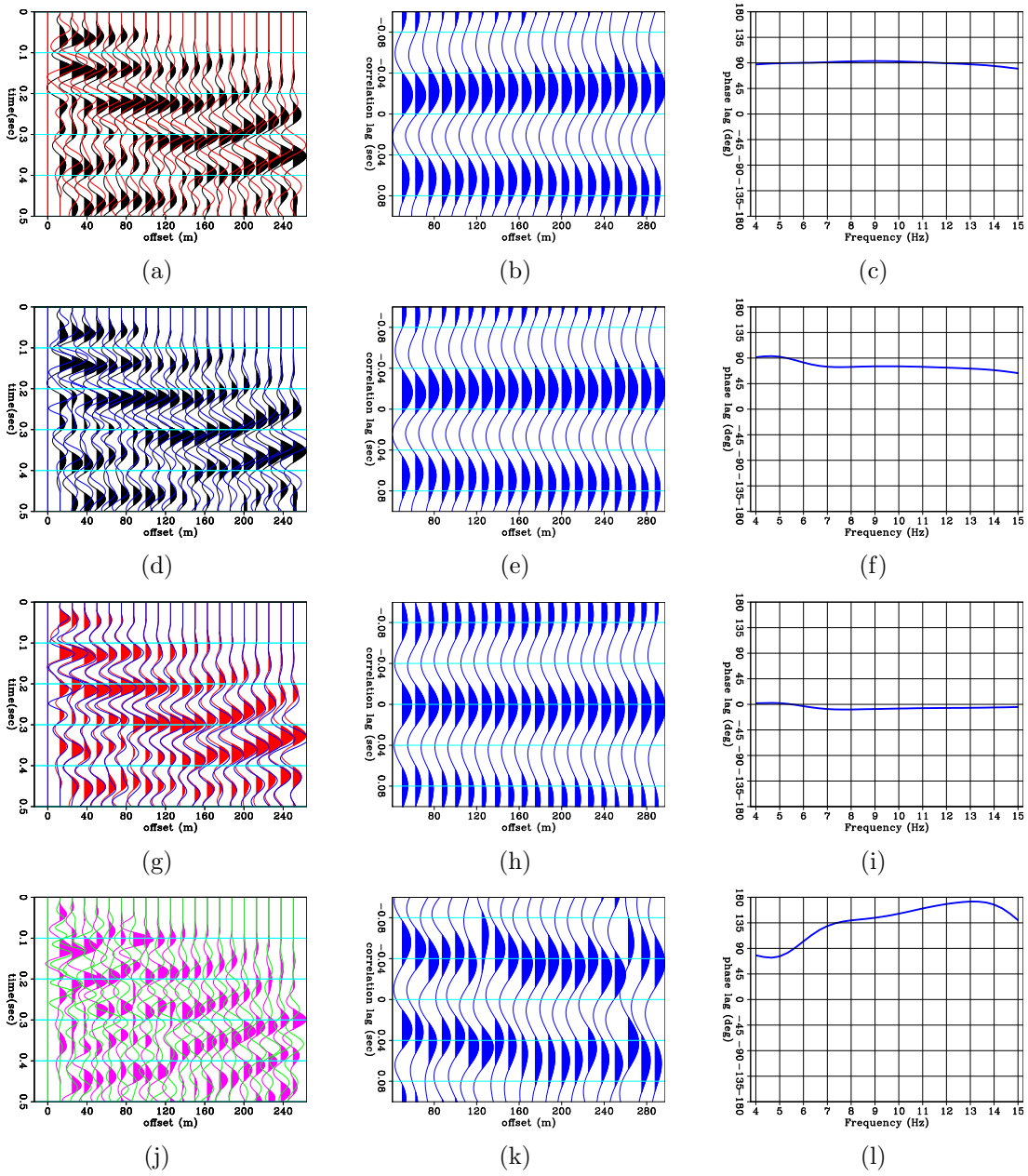

Figure 3.11: Comparison of receiver gather data components after linear moveout and AGC (left column), their correlation (center column) and their average phase difference (right column) for the slower surface wave mode. (a)-(c): Vertical (black) vs Radial (red). (d)-(f): Vertical (black) vs Pitch (blue). (g)-(i): Radial (red) vs Pitch (blue). (j)-(l): Transverse (purple) vs Yaw (green). The radial and pitch components are in phase. The vertical component lags behind the radial and pitch by 90^o. The transverse component lags behind the yaw by 90^o-180^o. [**ER**] chap3/. 322a,322b,322c,322d,322e,322f,322g,322h,322i,322j,322k,322l

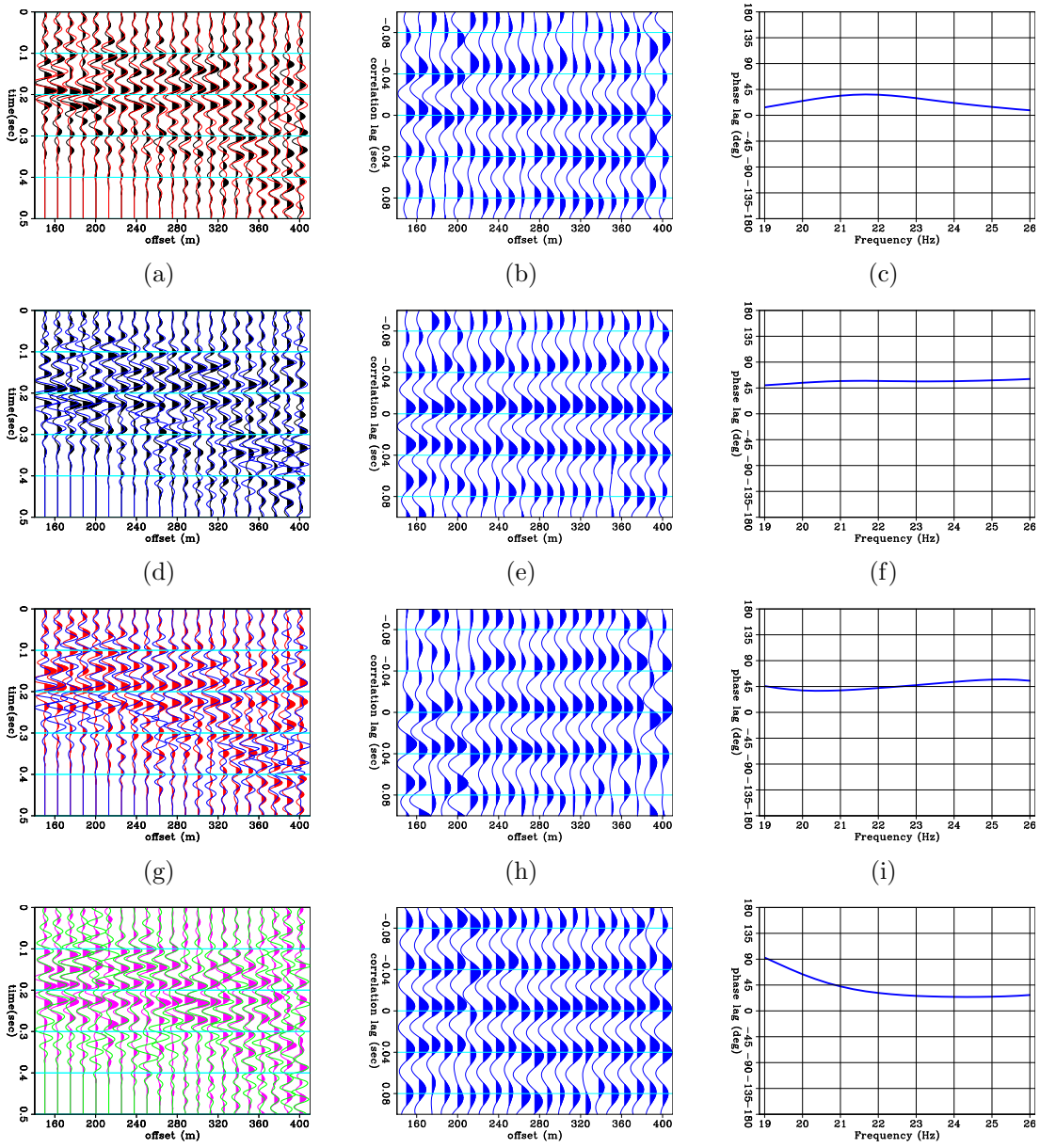

Figure 3.12: Comparison of receiver gather data components after linear moveout and AGC (left column), their correlation (center column) and their average phase difference (right column) for the faster surface wave mode. (a)-(c): Vertical (black) vs Radial (red). (d)-(f): Vertical (black) vs Pitch (blue). (g)-(i): Radial (red) vs Pitch (blue). (j)-(l): Transverse (purple) vs Yaw (green). The vertical and radial components are mostly in phase, and both lag behind the pitch by about 45^o. The transverse and yaw components are almost in phase for frequency range 21 - 26 Hz. [**ER**] chap3/. 323a,323b,323c,323d,323e,323f,323g,323h,323i,323j,323k,323l

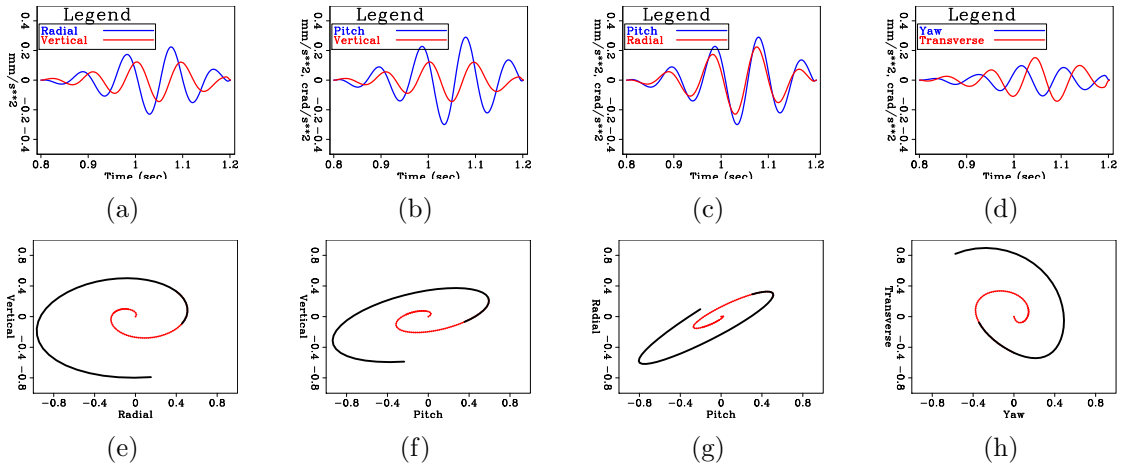

Figure 3.13: Data components for the slow ground roll wave mode for the trace at offset 210 m and their hodograms. (a),(e) Vertical vs Radial. (b),(f) Vertical vs Pitch. (c),(g) Radial vs Pitch. (d),(h) Transverse vs Yaw. The hodograms start from the dashed red line and progress to the solid black line. [**ER**]

chap3/. 324a,324b,324c,324d,324e,324f,324g,324h

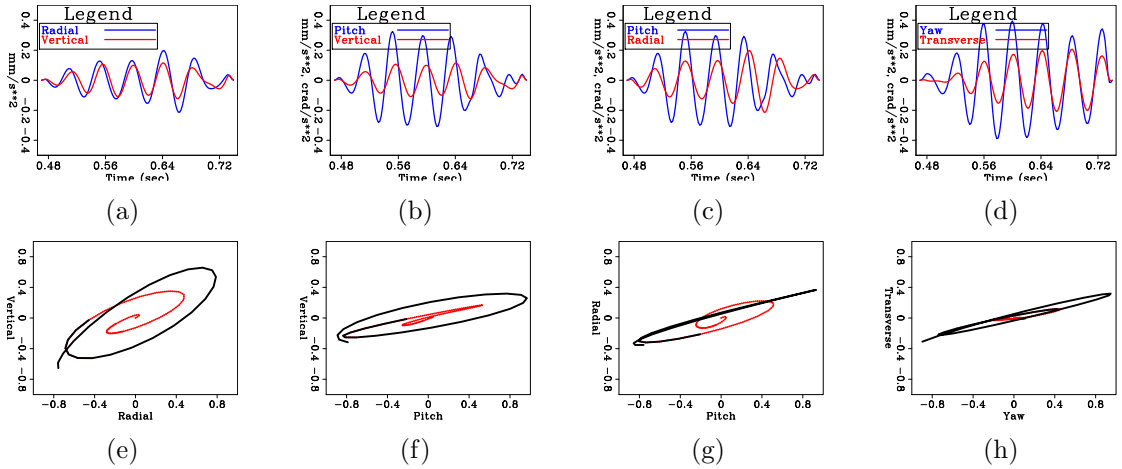

Figure 3.14: Data components for the fast ground roll wave mode for the trace at offset 210 m and their hodograms. (a),(e) Vertical vs Radial. (b),(f) Vertical vs Pitch. (c),(g) Radial vs Pitch. (d),(h) Transverse vs Yaw. The hodograms start from the dashed red line and progress to the solid black line. [**ER**]

chap3/. 325a,325b,325c,325d,325e,325f,325g,325h

at offset=200 m and ending at $t = 0.5$ s at offset=400 m. Judging by the frequency content and moveout of this event in the receiver gather, I think it is a result of shear-wave energy scattering off an anomaly in the near surface and generating surface waves. Regardless of the mechanism by which this shear-like event is generated, it is visible on all components in Figures 3.7(a)-3.7(f) and, like the ground roll for the surface sources, it obscures the P-wave reflections. I therefore target this particular shear arrival for removal from the 50 m depth dynamite data.

Filtering of a shear wave from the 50 m depth dynamite data

Figure 3.16(g) is the vertical geophone receiver gather for the 50 m depth dynamite source at receiver station 335. The shear-induced surface wave arrival that appears to have slower moveout than the moved-out P waves is circled.

My intent was to remove the surface wave using all six available data components (vertical, radial, transverse, yaw, roll and pitch). I do not, however, have reliable rotation-sensor data for the yaw and roll components. Therefore, for the analysis that follows I used only three components out of the available six: the vertical, radial and pitch. Since the survey was 2D, with the shot line running parallel and very close to the receiver line (Figure 3.3), most of the coherent seismic energy should appear on these components.

Figures 3.16(a), 3.16(c) and 3.16(d) are the vertical, radial and pitch component traces from the 50 m depth dynamite source at offset 280 m. The pitch component was derived by vertical-geophone differencing, which produced data with a better SNR than the pitch rotation sensor. Figures 3.16(b), 3.16(d) and 3.16(e) are the absolute values of CWT coefficients (eq. 3.1) of the respective three components of the trace. AGC has been applied to Figures 3.16(b), 3.16(d) and 3.16(e) to balance the amplitudes in the display and enable the viewer to see the weaker P-wave contribution. The frequency decreases by powers of two for every scale, starting from scale 0. For wavelet scale 0 the corresponding frequency is 128 Hz, and at wavelet scale 8 the corresponding frequency is 0.5 Hz. Observe that between $t = 0.2$ s and $t = 0.3$ s there are P wave reflections, and that these reflections correspond to lower wavelet scales (higher frequencies) in the continuous wavelet domain of all the components. At $t = 0.4$ s there is a shear-induced arrival, which appears in the wavelet domain as

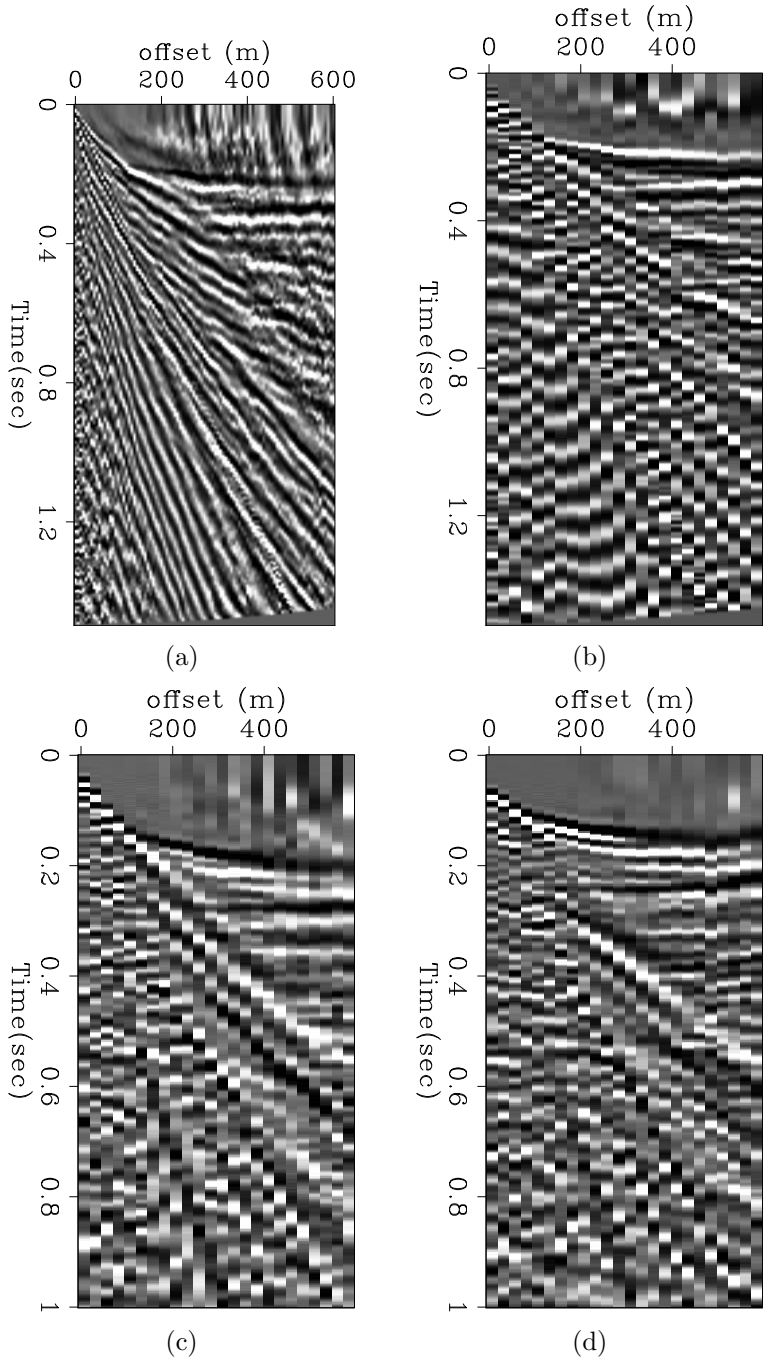

Figure 3.15: Receiver gathers of the vertical geophone component of the 4 source types in the Kettleman survey, after NMO with velocity $v = 1700$m/s. (a) Accelerated weight drop. (b) Vibroseis source. (c) Dynamite charge at 25 m depth. (d) Dynamite charge at 50 m depth. Source (a) was acquired with 6.25 m shot spacing, while (b), (c) and (d) were done with 25 m shot spacing. Observe the generally higher quality reflections acquired with the dynamite sources. The two surface sources (a) and (b) generate much more ground roll. AGC with a window size of $t = 0.2$ s has been applied to the data for display. [**ER**] chap3/. 307a,307b,307c,307d

a higher scale feature (lower frequency). However, this feature is more significant on the vertical and radial components than on the pitch component, where it is barely visible.

These two distinguishing attributes of the shear arrival: lower frequency and different appearance in the wavelet domain of the various data components, are what I use to identify and attenuate it.

Figure 3.17(a) shows the time slice of the CWT of the three data components of the same trace, at time $t = 0.22$ s where there are P-wave reflections. I apply SVD to this time slice as described in equation 3.3, and display the 1st, 2nd and 3rd scaled polarization vectors as in equation 3.4 in Figures 3.17(b), 3.17(c) and 3.17(d), respectively. Each row in these figures represents one polarization vector. Note the pattern visible for the first polarization vectors, which indicates that the energy at this time has both high frequency and lower frequency polarization.

Figure 3.18(a) shows the time slice of the CWT of the three data components at time $t = 0.42$ s, which is the shear-arrival time. The 1st, 2nd and 3rd scaled polarization vectors are shown in Figures 3.18(b), 3.18(c) and 3.18(d), respectively. For this arrival, the first polarization vectors in Figure 3.18(b) show a very different pattern compared to Figure 3.17(b), and indicate that at this arrival's time the polarization is largely on the lower frequencies and on the vertical and radial components.

The shear arrival's 2nd polarization vectors in Figure 3.18(c), however, have a wider frequency band than the 1st polarization vector in Figure 3.18(b), and it resembles more the 1st polarization vectors of the P-wave reflections in Figure 3.17(b). This indicates what can already be seen from the data in Figure 3.15(d): the shear arrival is obscuring the P reflections. The 2nd polarization vector reveals the underlying energy. I set the template polarization $\mathbf{S}_{\text{temp}}(a)$ to be Figure 3.18(b), and it is this polarization that I search for in the data on a trace by trace basis.

Figure 3.19 shows the set of scalar weights which are applied to the first polarization vectors of the CWT of the multicomponent trace (the w_1 element in eq. 3.8). Note how the higher scales (lower frequencies) are preferentially damped. However, note that this is not simply a weighting down of low frequencies. The weighting function depends on the similarity of the first polarization vectors at each time and at each frequency to the template polarization in Figure 3.18(b). Where there is a

similarity, the lower frequencies are preferentially weighted down.

Figures 3.20(a), 3.20(b) and 3.20(c) are the vertical, radial and pitch components before application of the polarization filtering, while Figures 3.20(d), 3.20(e) and 3.20(f) are the same components after application of the polarization filtering. Note that the shear-induced arrival that I targeted for removal has indeed been attenuated, and the P-wave reflection signal which was hidden below it has been enhanced. The P-wave reflections appear continuous.

Note also that I used only one time window of one trace to determine the polarization template of this shear energy, and yet after applying the filtering based on that polarization template to the entire dataset the shear energy has been attenuated everywhere and for all components.

Figure 3.21(a) is again the input vertical component of the 50 m depth dynamite receiver gather at station 335, while Figure 3.21(d) is the same gather in frequency-wavenumber domain. Figure 3.21(b) shows the vertical component after the polarization filtering, while Figure 3.21(e) shows the frequency-wavenumber spectra of these data. Compare this to a low-cut filter, where the pass band was 25 Hz - 60 Hz, shown in Figure 3.21(c). There is a an improvement in continuity of the P-wave reflections, but the shear energy is still apparent. The resolution of the P reflections, however, has been degraded because of the simple frequency filter. Comparing Figures 3.21(e) and 3.21(f), we see that unlike standard frequency filtering, the polarization filtering has not performed a wholesale removal of the low frequencies.

Filtering of a shear wave from the 25 m depth dynamite data

The data from the 25 m depth dynamite shots in Figure 3.22(a) is similar to the 50 m depth shots in Figure 3.20(a), except that there is strong, coherent, low-frequency ground roll visible, propagating at approximately air-speed velocity. There is an arrival similar to the shear-induced surface wave arrival on the 50 m depth shot data, which for the 25 m depth shots is more prominent and has a linear moveout.

I used a time window from one trace of each of these arrivals to calculate the polarization templates of these wave modes. I then applied the polarization filtering method to target and attenuate these wave modes. The results can be seen when comparing Figures 3.22(a), 3.22(b) and 3.22(c) to Figures 3.22(d), 3.22(e) and 3.22(f).

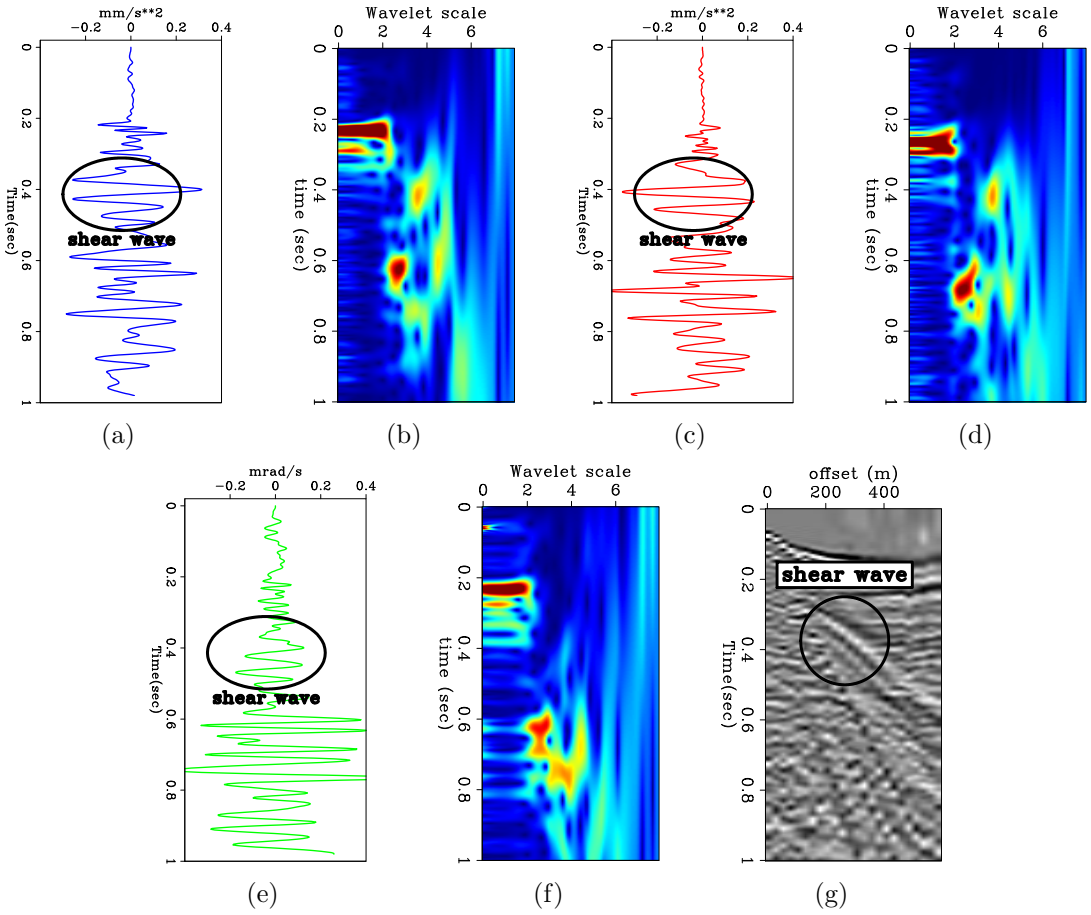

Figure 3.16: (g) Vertical geophone component of 50 m depth dynamite data after NMO. (a) Trace of the vertical component at offset=280 m. (b) Absolute values of the continuous wavelet transform coefficients for vertical component. (c) Trace of the radial component at offset=280 m. (d) Absolute values of the continuous wavelet transform coefficients for radial component. (e) Trace of the pitch component at offset=280 m. (f) Absolute values of the continuous wavelet transform coefficients for pitch component. AGC has been applied to (b), (d) and (f) to enable a more equalized view of the wavelet coefficients over the time and scale axes (without AGC, the units are |mm/s| /scale). The wavelet scale is dyadic, beginning from a frequency of 128 Hz at wavelet scale 0 down to 0.5 Hz at wavelet scale 8. Up until $t = 0.32$ s, the data contain P reflections, while between $t = 0.32$ s and $t = 0.52$ s there is a shear-wave arrival. The lower frequency of the shear arrival can be discerned at $t = 0.4$ s, for wavelet scale=3.8. [**ER**] chap3/. 308b,308c,308d,308e,308f,308g,308a

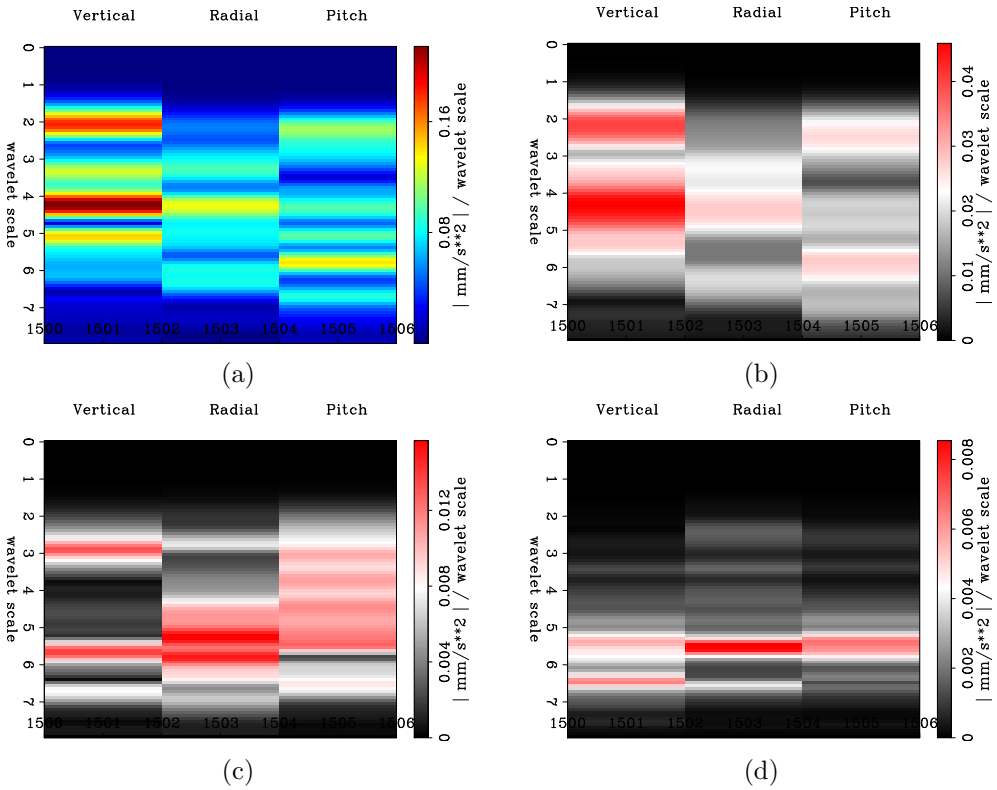

Figure 3.17: A 3C time slice of the continuous wavelet transform of the trace at offset 280 m at $t = 0.22$ s where a P-wave reflection is visible, and the corresponding absolute values of the CWT polarization vector-set for this time slice, scaled by their respective singular values (eq. 3.4). (a) Continuous wavelet time slice. (b) 1st, (c) 2nd, and (d) 3rd polarization vectors. [**ER**] chap3/. 309a,309b,309c,309d

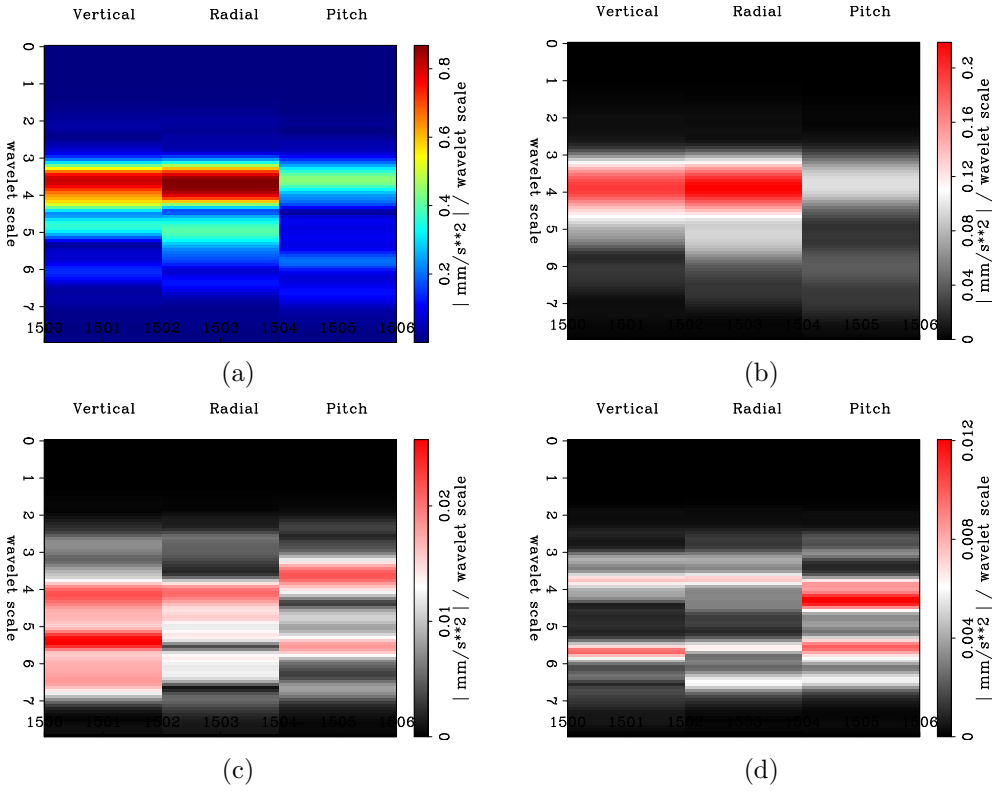

Figure 3.18: A 3C time slice of the continuous wavelet transform of the trace at offset 280 m at $t = 0.42$ s where shear-wave energy dominates, and the corresponding absolute values of the CWT polarization vector-set for this time slice, scaled by their respective singular values (eq. 3.4). (a) Continuous wavelet time slice. (b) 1st, (c) 2nd, and (d) 3rd polarization vectors. Note that the 2nd polarization vectors at (c) have a wider frequency band than the 1st polarization vectors at (b), and are more similar to the 1st polarization vectors at 3.17(b), indicating that the dominant shear-wave energy in (b) is overlaying weaker P-wave reflection energy. [**ER**]
chap3/. 310a,310b,310c,310d

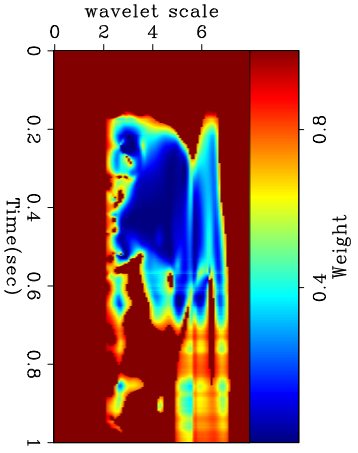

Figure 3.19: The set of scalar w_1 weights (eq. 3.8) applied to the first polarization vector of the data in the wavelet domain to attenuate the shear wave mode appearing at ($x = 280$m, $t = 0.4$s) in Figure 3.16(a). [**ER**]
chap3/. 311

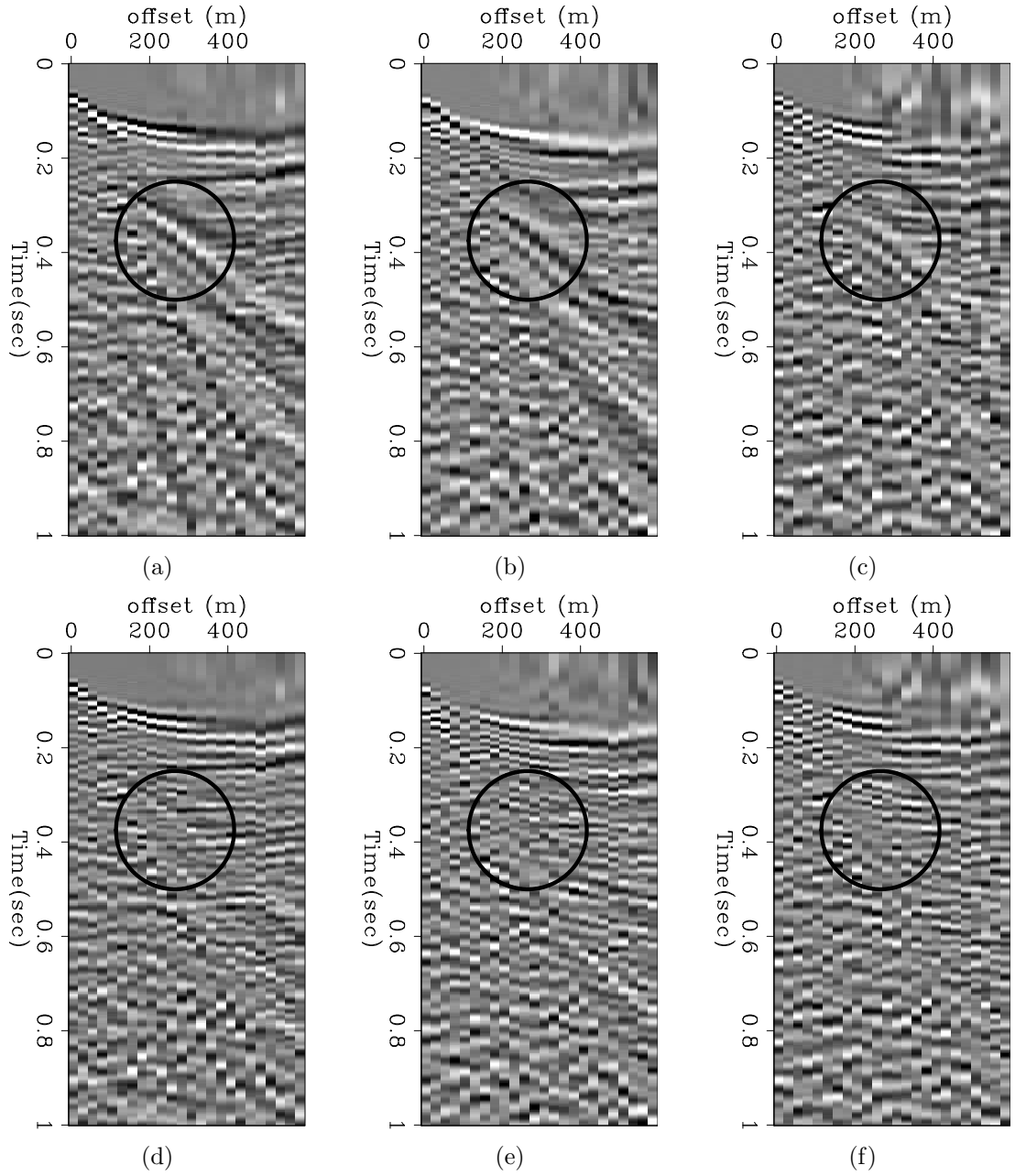

Figure 3.20: Receiver gather of 50 m depth dynamite source before (top row) and after (bottom row) polarization filter to attenuate the shear arrival at (t,x) = (0.4 s, 300 m). (a) Vertical component. (b) Radial component. (c) Pitch component. (d) Vertical component. (e) Radial component. (f) Pitch component. Data are shown after NMO with velocity $v = 1700$ m/s to flatten the P-wave reflections. AGC with a window size of $t = 0.2$ s has been applied for display purposes. Observe that the circled shear-induced event has been attenuated, and that the underlying P-wave reflections are visible after filtering. The filter has killed the noise and the P-wave data have survived. [**ER**] chap3/. 312a,312b,312c,312d,312e,312f

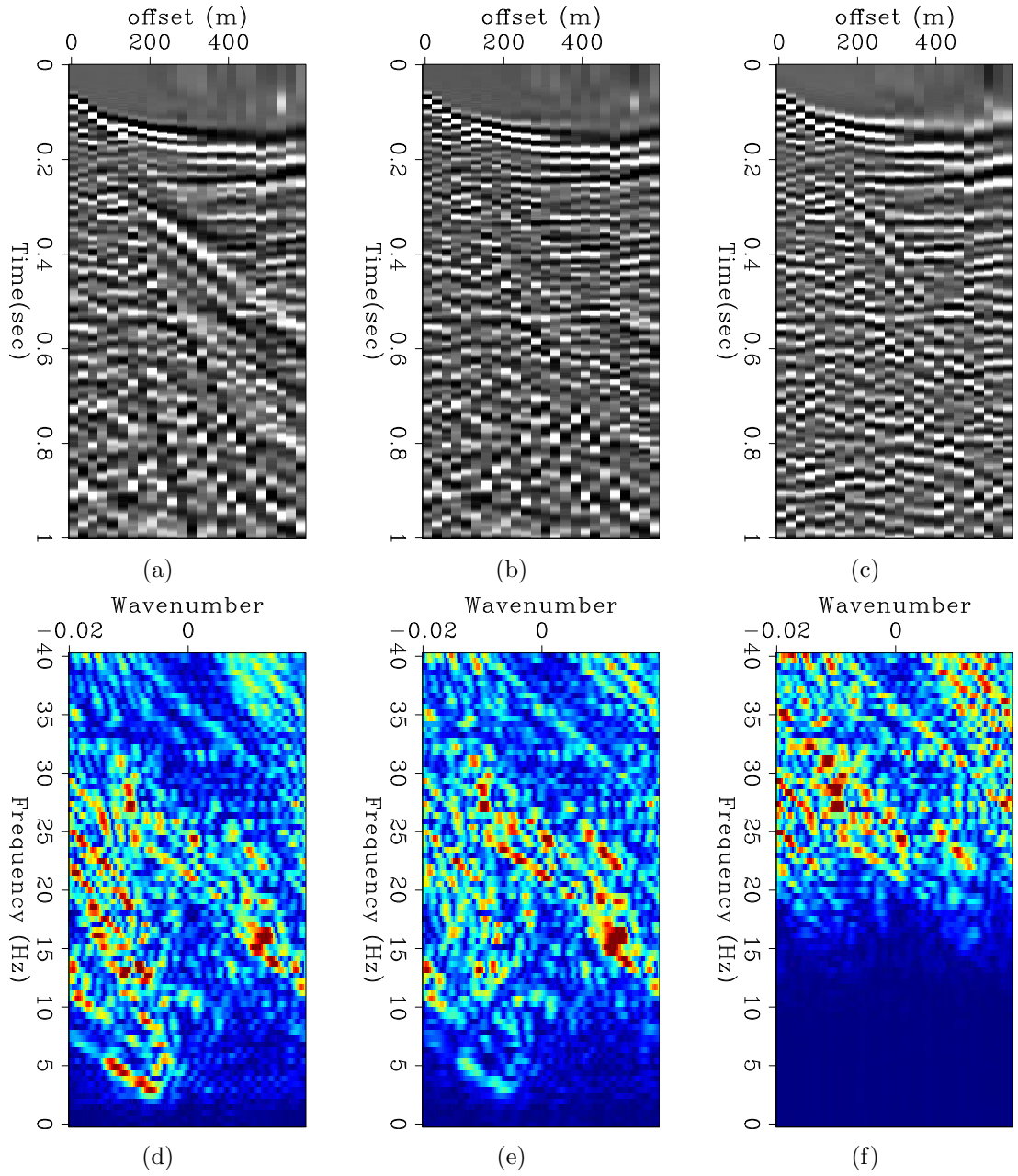

Figure 3.21: A comparison of the filtering results using continuous wavelet polarization filter versus a low-cut filter on the 50 m depth dynamite receiver gather at station 335. (a) Vertical component. (b) Vertical component after application of continuous wavelet polarization filter. (c) Vertical component after application of a low-cut filter, where the pass band was 25 Hz - 60 Hz. (d) Vertical component (a) in frequency-wavenumber domain. (e) Vertical component (b) in the frequency-wavenumber domain. (f) Vertical component (c) in the frequency-wavenumber domain. AGC was applied to the data prior to FK transform. Observe how in (b) and (e), the polarization filtering does not impartially remove low frequencies, unlike the low-cut filter in (c) and (f), and therefore there is no reduction in the spectral resolution of the data. [**ER**] chap3/. 313a,313b,313c,313d,313e,313f

Note how both of the targeted wave modes have been mostly removed, although the shear-induced wave is still obscuring some of the P-wave reflections. The slow ground roll has been removed despite being spatially aliased.

Filtering of aliased ground roll from the vibroseis data

The vibroseis data contain strong, aliased ground roll, which are much stronger than the P reflections at near offsets. Figures 3.23(a), 3.23(b) and 3.23(c) are the vertical, radial and pitch components after NMO and before application of the CWT polarization filtering. A slow Rayleigh wave mode propagating at around 250 m/s is visible beginning from $t = 0.2$ s and ending at $t = 0.8$ s at offset 400 m. There is a faster Rayleigh wave mode propagating at about 400 m/s, and yet another, more dispersive and faster mode propagating at 600 m/s. Since NMO has been applied, the P-wave reflections are flat, and it is obvious that they are dominated by the ground roll at nearer offsets and later times.

To estimate the polarization template for the slow Rayleigh wave mode, I took a time-window from four traces containing this slow Rayleigh wave mode around $t = 0.6$ s. For the two faster Rayleigh modes, I selected a representative time window from a single trace where these modes were dominant. I then applied the same polarization filtering method as for the dynamite data, comparing the first polarization vector of each time sample (in the CWT domain) to the template polarization, and weighing it down by its similarity to the template.

Figures 3.23(d), 3.23(e) and 3.23(f) are the vertical, radial and pitch components after application of the polarization filtering. Observe how the various Rayleigh wavemodes have been attenuated. In the area indicated by the top circle, the horizontal P arrivals are now visible from underneath the ground-roll cone. As before, the targeted wave modes (the "noise") have been attenuated on all data components.

The targeting of the aliased, slow ground roll also more visible in the frequency-wavenumber domain, as can be seen by comparing Figures 3.24(c) and 3.24(d). Observe how the aliased high-wavenumber energy relating to the slow ground roll has been removed. Consequently, the P wavenumbers are more dominant in the filtered F-K domain in Figure 3.24(d). These figures show the advantage that polarization filtering has over standard frequency-wavenumber filters. An F-K filter would have

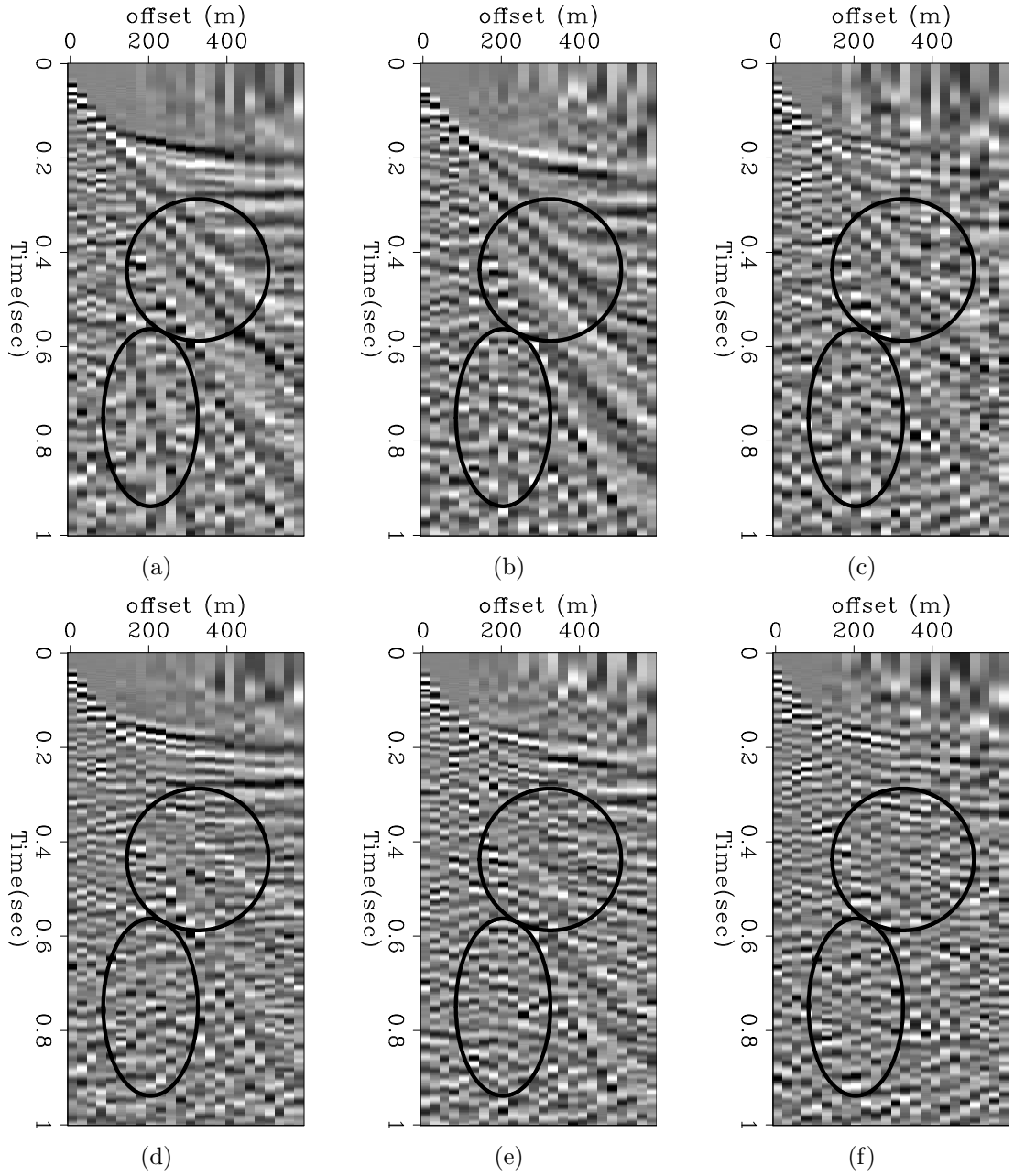

Figure 3.22: Receiver gather of 25 m depth dynamite source before (top row) and after (bottom row) polarization filter to attenuate shear and ground roll energy. (a) Vertical component. (b) Radial component. (c) Pitch component. (d) Vertical component. (e) Radial component. (f) Pitch component. Data are shown after NMO with velocity $v = 1700$ m/s to flatten the P-wave reflections. AGC with a window size of $t = 0.2$ s has been applied for display purposes. The shear-induced energy and the spatially-aliased ground roll have been mostly attenuated, and the underlying P-wave reflections in the top circle are visible after filtering. In the top circle, we can see that the filter has killed the noise and the P-wave data have survived. [**ER**]
chap3/. 314a,314b,314c,314d,314e,314f

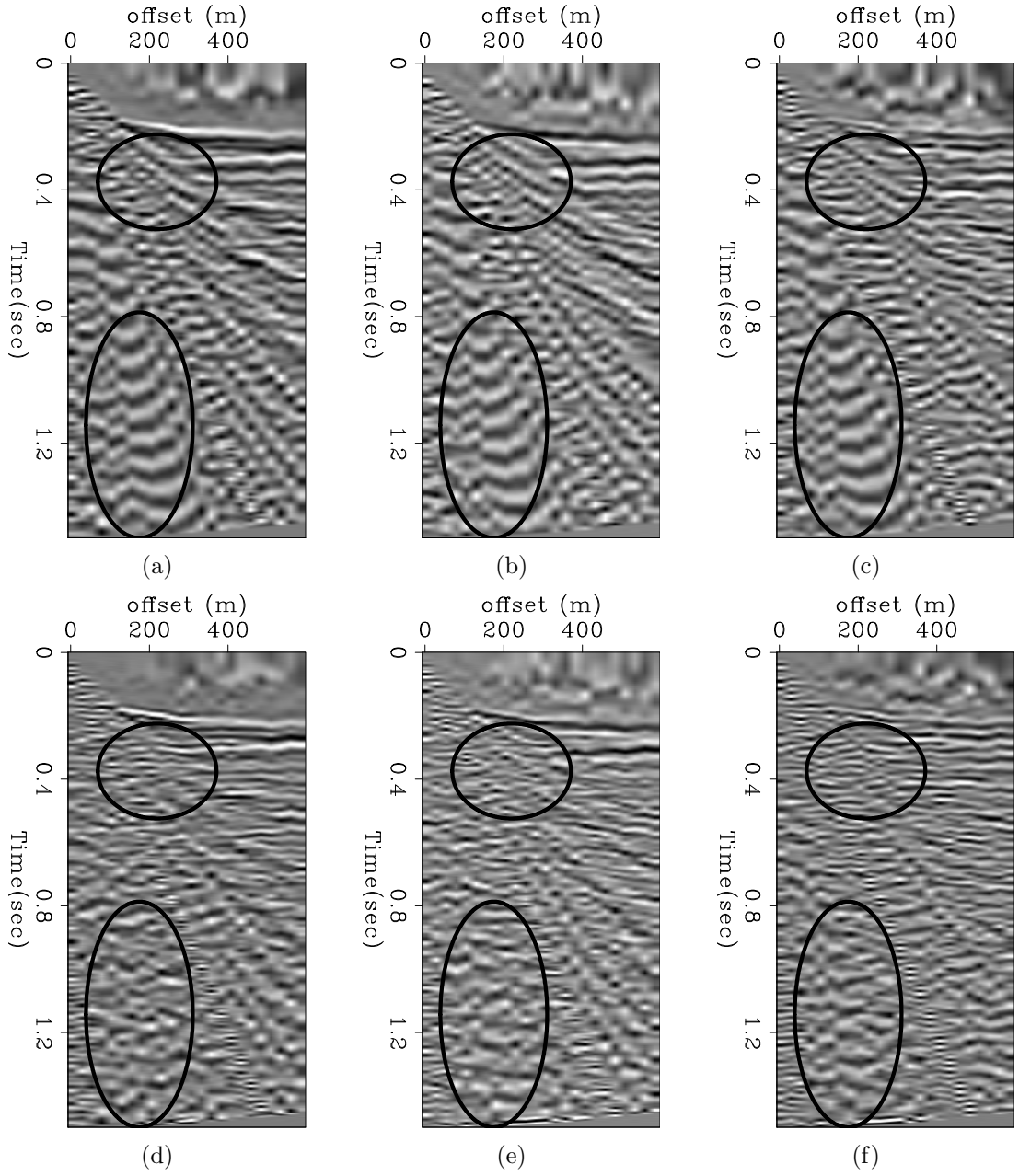

Figure 3.23: Receiver gather of vibroseis source before (top row) and after (bottom row) polarization filter to remove ground-roll energy. (a) Vertical component. (b) Radial component. (c) Pitch component. (d) Vertical component. (e) Radial component. (f) Pitch component. Data are shown after NMO with velocity $v = 1620$ m/s to flatten the P-wave reflections. AGC with a window size of $t = 0.2$ s has been applied for display purposes. The spatially aliased ground-roll energy in the bottom circle has been attenuated, though no coherent P-wave energy is visible underneath the noise. In the top circle, flat P-wave reflections are visible after filtering. [**ER**]
chap3/. 315a,315b,315c,315d,315e,315f

had difficulty in separating signal from noise because of the aliasing.

Advantage of using the rotational pitch component

To have a fair apples-to-apples comparison of the polarization template matching method for different data components, it is necessary to compare using the same number of components. This is due to the angular-difference based similarity measure between the template polarization vector and the data polarization vector at every sample (eq. 3.6). A different number of components means a different number of dimensions in the SVD polarization space. A polarization template vector calculated by applying SVD to 2-component data will have 2 elements, while a vector derived from 3-component data will have 3 elements.

The implication of the number of components on the region of the SVD polarization space which would be attenuated is shown in Figures 3.25(a) to 3.25(c). Figure 3.25(a) shows the volume in 3D space for which all vectors have a particular angular difference from the 3D template polarization vector, indicated by the blue arrow. The volume described has a cone shape. Figure 3.25(b) shows the 2D slice within which all vectors have a particular angular difference from the projection of the 3D template polarization vector onto one of the 2D planes, indicated by the red arrow. This area is a slice on the 2D plane, and it would be the result of using only 2 data components. Projecting this slice onto the 3D space, as is shown in Figure 3.25(c), we see that the resulting volume does not look like the cone for the case of 3D, but rather like a wedge. Therefore, the angular difference between two vectors in 3D is more restrictive than for 2D (geometrically, a "cone" versus a "wedge"), and will affect the similarity measure and the corresponding damping weights. In order to properly compare between polarization template matching for 2 vs 3 data components, the weights for the 3-component case would need to be designed as shown in 3.25(c).

The reliable components from the Kettleman survey are the vertical, radial and transverse translational components, and the pitch rotational component. In order to demonstrate the additional wave-mode identification capability introduced by the pitch component, I compare the polarization filtering results using the vertical, radial and pitch components with those obtained using the vertical, radial and transverse components.

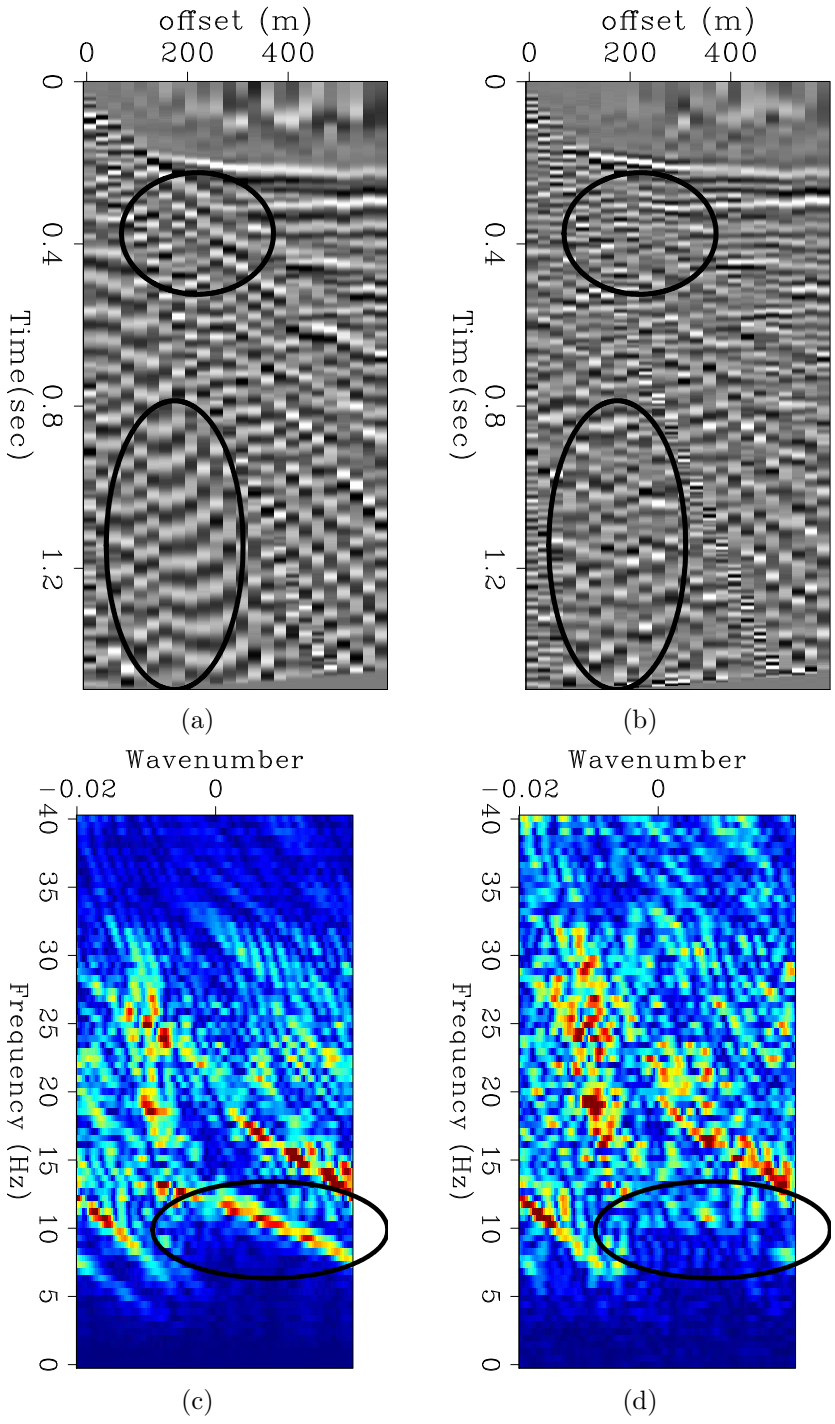

Figure 3.24: Comparison of the vertical component receiver gather before and after polarization filtering to remove ground-roll energy in the frequency wavenumber domain. (a) Vertical component before filtering. (b) Vertical component after filtering. (c) Vertical component in the F-K domain before filtering. (d) Vertical component in the F-K domain after filtering. AGC was applied prior to FK transform. Note the circled aliased energy that is removed in (d) vs (c). This energy corresponds to the ground roll indicated in the bottom circle in (a) and (b) The broadband, low-wavenumber P reflection energy is more dominant in (b). A standard frequency-wavenumber filter would have had difficulty in separating signal from noise because of the aliasing. [**ER**] chap3/. 316a,316b,316c,316d

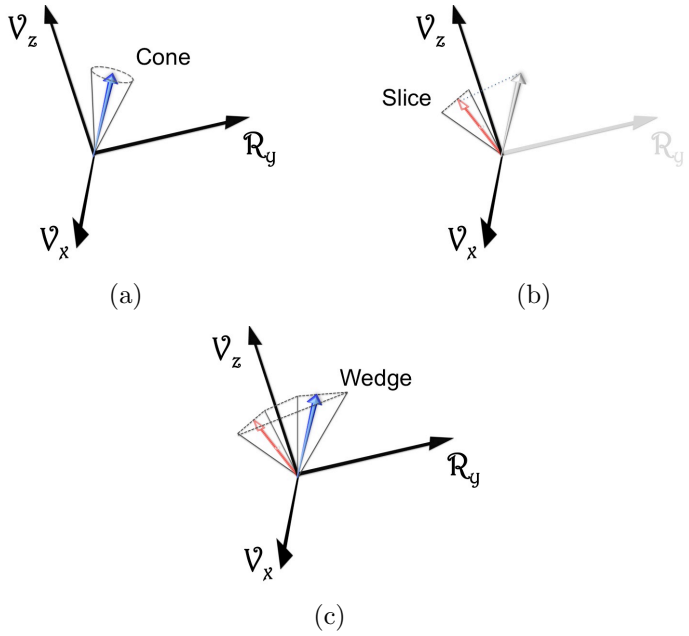

Figure 3.25: Illustration of the differences between designing the damping weights (eq. 3.7) in the SVD polarization space for 3 components versus 2 components. The axes represent the polarization unit vectors, while the blue arrow indicates the template polarization vector in the 3D space. The red arrow indicates the projection of the template polarization onto one of the 2D planes. (a) The conical shape of the volume in the 3D SVD space that would be damped using the angle-based similarity measure (eq. 3.6) if 3 data components were used. (b) The slice of the 2D SVD space that would be damped using the angle-based similarity measure if only 2 data components were used. (c) The projection of the damped 2D SVD space to the 3D SVD space, which is a wedge-shaped volume rather than a conical one as for 3D damping. The angular difference between two vectors in 3D is more restrictive than for 2D and will affect the similarity measure and the corresponding damping weights. To compare the polarization template matching for different data components, it is therefore necessary to always compare using the same number of components. [**NR**] chap3/. 3D-weight,2D-weight,2D-weight-proj

Pitch vs transverse comparison for 25 m depth dynamite source

Figures 3.26(a), 3.26(b), 3.26(c) and 3.26(d) are the input receiver gathers of the vertical, radial, transverse, and pitch components of the 25 m depth dynamite source. The black circles indicate the shear-induced and Rayleigh wave modes that I am targeting for removal.

Figures 3.26(e) and 3.26(g) are the vertical and radial components after filtering based on the polarization vectors derived from the vertical, radial and pitch components. The circles indicate the attenuated shear wave and ground roll energy. Figures 3.26(f) and 3.26(h) are the vertical and radial components after filtering based on the polarization vectors derived from the vertical, radial and transverse components.

Comparing Figures 3.26(e) and 3.26(f), I observe that the shear wave indicated by the top circle is better attenuated when using the pitch component vs using the transverse. The flattened P waves are more continuous in Figure 3.26(e) vs Figure 3.26(f). Additionally, the aliased ground roll indicated by the bottom circle is still present in Figure 3.26(f). The same observations hold for the comparison of the attenuation of these undesired wave modes on the radial component in Figures 3.26(g) and 3.26(h).

The pitch component of this gather contains more of the coherent energy of the shear and ground roll arrivals than does the transverse, and therefore using the pitch instead of the transverse component in the polarization analysis enables a better identification and separation of these wave modes.

Pitch vs transverse comparison for vibroseis source

I now compare the polarization filtering results of the slow (250 m/s) Rayleigh wave mode in the vibroseis data using the vertical, radial and pitch components with those obtained using the vertical, radial and transverse components. Figures 3.27(a), 3.27(b), 3.27(c) and 3.27(d) are the input receiver gathers of the vertical, radial, transverse, and pitch components of the vibroseis source. The slow, aliased ground roll is circled. I use only the slow ground roll's polarization template, targeting it for removal.

Figures 3.27(e) and 3.27(g) are the vertical and radial components after filtering

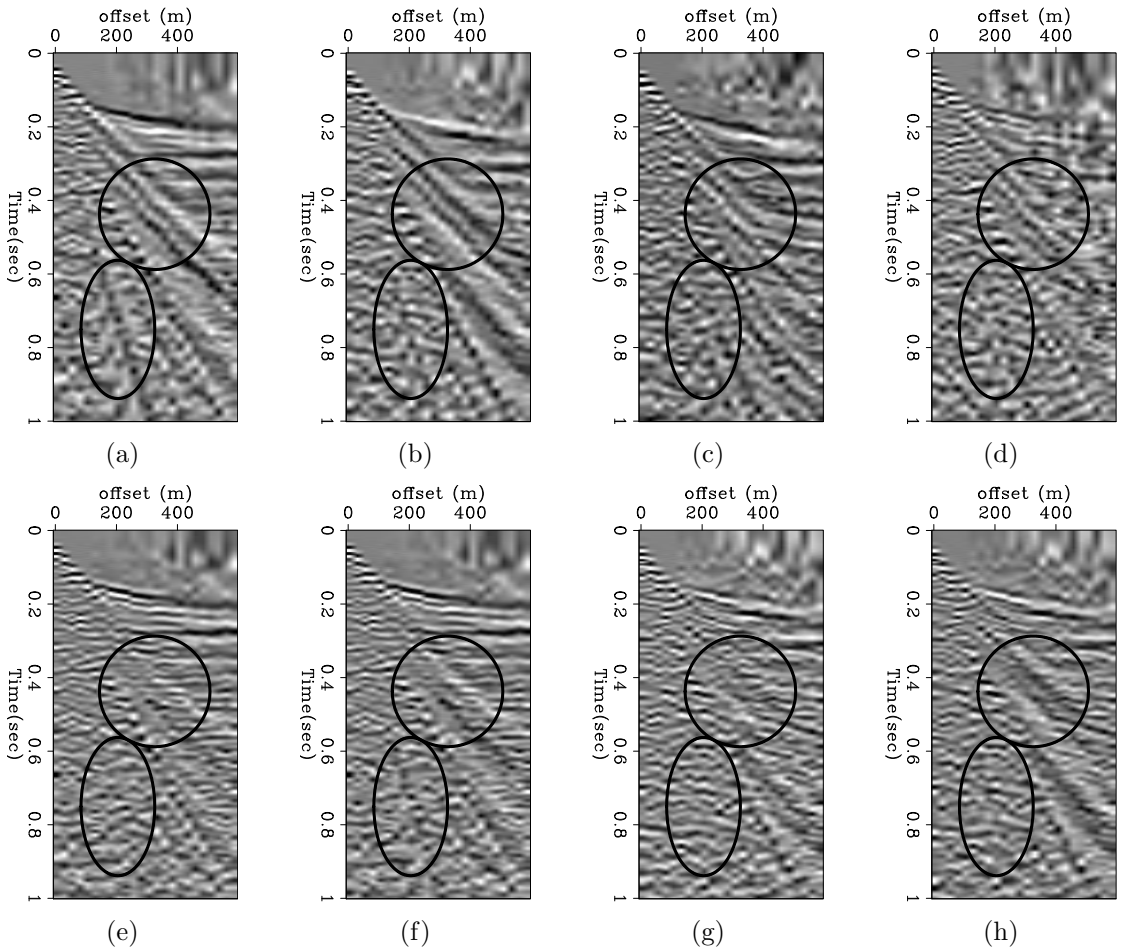

Figure 3.26: Comparison of polarization filtering of the shear-induced and ground roll energy in the 25 m depth dynamite receiver gathers, when using the vertical (V_z), radial (V_x) and pitch (R_y) components as inputs vs when using the vertical (V_z), radial (V_x) and transverse (V_y) components as inputs. (a) The input vertical (V_z) component. (b) The input radial (V_x) component. (c) The input transverse (V_y) component. (d) The input pitch (R_y) component. (e) Vertical component after filtering using V_z, V_x, R_y components. (f) Vertical component after filtering using V_z, V_x, V_y components. (g) Radial component after filtering using V_z, V_x, R_y components. (h) Radial component after filtering using V_z, V_x, V_y components. Data are shown after NMO with velocity $v = 1700$ m/s to flatten the P-wave reflections. AGC with a window size of $t = 0.2$ s has been applied for display purposes. Comparing (e) to (f) and (g) to (h), I observe that the shear-induced energy and particularly the spatially-aliased ground roll at $t = 0.6$ s are better attenuated when using the pitch rotational component, which contains more coherent energy of these wave modes than does the transverse component. [**ER**] chap3/. 317a,317b,317c,317d,317e,317f,317g,317h

based on the polarization vectors derived from the vertical, radial and pitch components. The circles indicate where the ground roll energy has been attenuated. Figures 3.27(f) and 3.27(h) are the vertical and radial components after filtering based on the polarization vectors derived from the vertical, radial and transverse components.

Comparing Figures 3.27(e) and 3.27(f), I observe that the aliased ground roll is better attenuated when using the pitch component vs using the transverse. Additionally, the aliased ground roll indicated by the circle has not been removed in Figure 3.27(f). The same observations hold for the comparison of the attenuation of the slow ground roll on the radial component in Figures 3.27(g) and 3.27(h).

The pitch component of this gather contains more of the coherent energy of the slow ground roll than does the transverse. This is consistent with the 2D geometry of the survey, and with the expected deformations and particle translations that a Rayleigh wave should have as it propagates in the survey's inline direction. We should expect the Rayleigh wave initiated at the source point to propagate outwards and generate vertical and radial motions, but very little transverse motion. The Rayleigh wave should also induce a rotational deformation around the transverse axis, i.e., pitch rotations, as shown in Figure 1.10(a). Therefore using the pitch instead of the transverse component in the polarization analysis enables a better separation capability of the slow Rayleigh wave mode.

Pitch vs transverse comparison for the 50 m depth dynamite source

Figures 3.28(a), 3.28(b), 3.28(c) and 3.28(d) are the input receiver gathers of the vertical, radial, transverse, and pitch components of the 50 m depth dynamite source. The black circle indicates the shear-induced wave mode that I am targeting for removal.

Figures 3.28(e) and 3.28(g) are the vertical and radial components after filtering based on the polarization vectors derived from the vertical, radial and pitch components. The circle indicates the attenuated shear-induced wave. Figures 3.28(f) and 3.28(h) are the vertical and radial components after filtering based on the polarization vectors derived from the vertical, radial and transverse components.

Comparing Figure 3.28(e) with Figure 3.28(f), and Figure 3.28(g) with Figure 3.28(h), I observe that the shear wave is attenuated equally well using either the pitch or the transverse components. The shear wave is similarly dominant on both

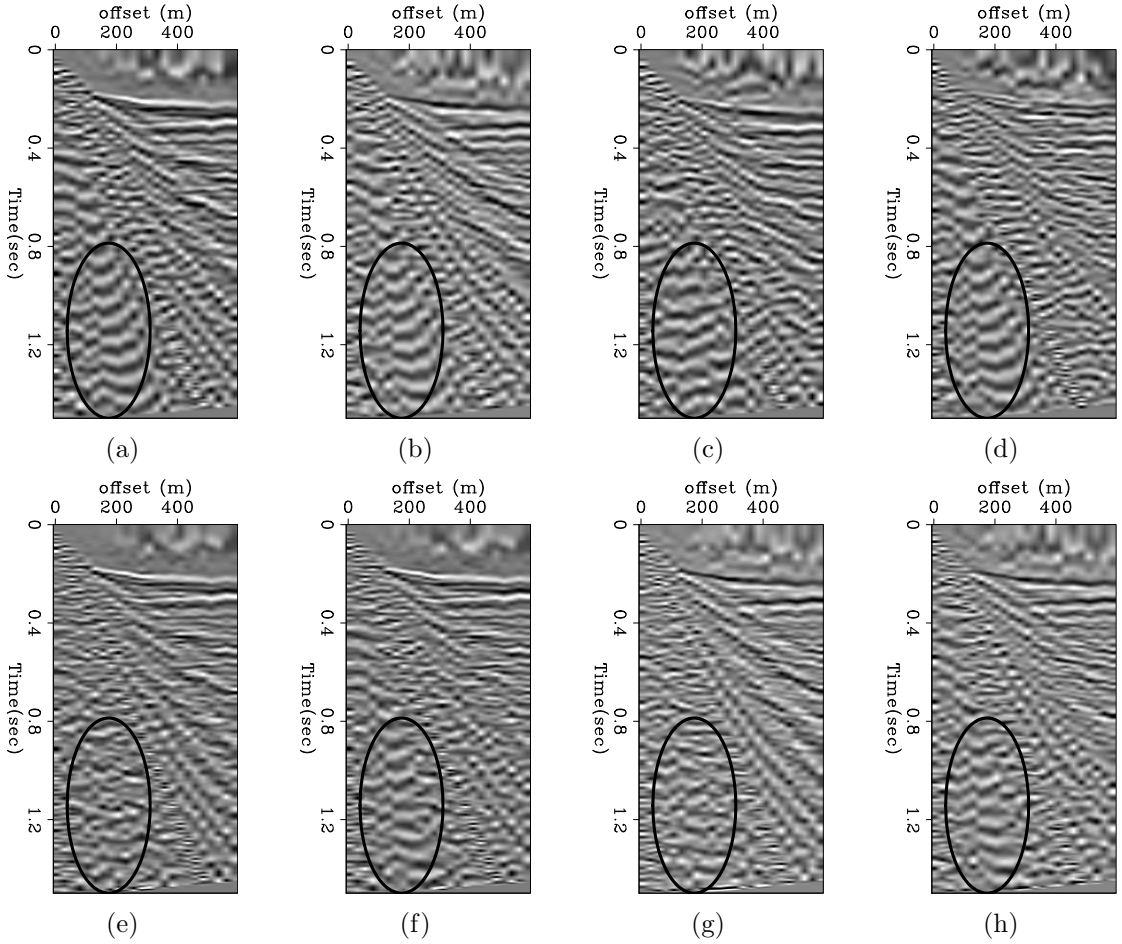

Figure 3.27: Comparison of polarization filtering of the slow (250 m/s) ground roll in the vibroseis receiver gathers, when using the vertical (V_z), radial (V_x) and pitch (R_y) components as inputs vs. when using the vertical (V_z), radial (V_x) and tranverse (V_y) components as inputs. (a) The input vertical (V_z) component. (b) The input radial (V_x) component. (c) The input transverse (V_y) component. (d) The input pitch (R_y) component. (e) Vertical component after filtering using V_z, V_x, R_y components. (f) Vertical component after filtering using V_z, V_x, V_y components. (g) Radial component after filtering using V_z, V_x, R_y components. (h) Radial component after filtering using V_z, V_x, V_y components. Data are shown after NMO with velocity $v = 1700$ m/s to flatten the P-wave reflections. AGC with a window size of $t = 0.2$ s has been applied for display purposes. Comparing (e) to (f) and (g) to (h), I observe that the spatially-aliased ground roll (circled) is better attenuated when using the pitch rotational component, which contains more coherent energy of the ground roll than does the transverse component. [**ER**] chap3/. 318a,318b,318c,318d,318e,318f,318g,318h

the input pitch (Figure 3.28(d)) and the input transverse (Figure 3.28(c)) components, and therefore both of them provide similar information to the polarization analysis.

DISCUSSION

Throughout this chapter I've referred to the method of wave-mode separation essentially as a data adaptive filtering. However, note that particular wave modes are being targeted, and the method attenuates only the targeted wave modes. This would not work if the method was not able to identify them.

The continuous wavelet domain enables an identification of wave modes based on their multicomponent spectral polarization vectors at each frequency, while retaining the temporal sense of the data. Therefore, the filtering is done in a very targeted manner, exactly where it is needed in time and space.

Rotations, being medium strains, are an indication of wave mode. Combining measured rotations with measured translations provides better discrimination between wave modes than using medium translations alone. For some wave modes, the rotational components provide additional identification capability by providing another orthogonal data axis in the SVD polarization space along which to identify those wave-mode's polarizations. The polarization analysis I show would welcome the use of as many independent data components as possible, since the more information we have available about each wave mode, the more orthogonal data axes will be in the SVD polarization space, the more we will be able to identify and separate between waves with different polarizations.

I've shown that the method is reasonably successful in attenuating particular, coherent source-generated wave modes (shear, Rayleigh) which obscure other weaker wave modes of interest (P-wave reflections). Like all polarization filtering methods, the method has no spatial sampling requirements, and will work on spatially aliased data.

However, the connection between wave modes and polarization of data components is not obvious. I do not provide an analytic model for determing how each wave mode should appear on any given component at any particular offset or azimuth. Instead, I effectively use an approach more similar to a data science method: the polarizations are learned from the data. This requires, however, a manual picking of

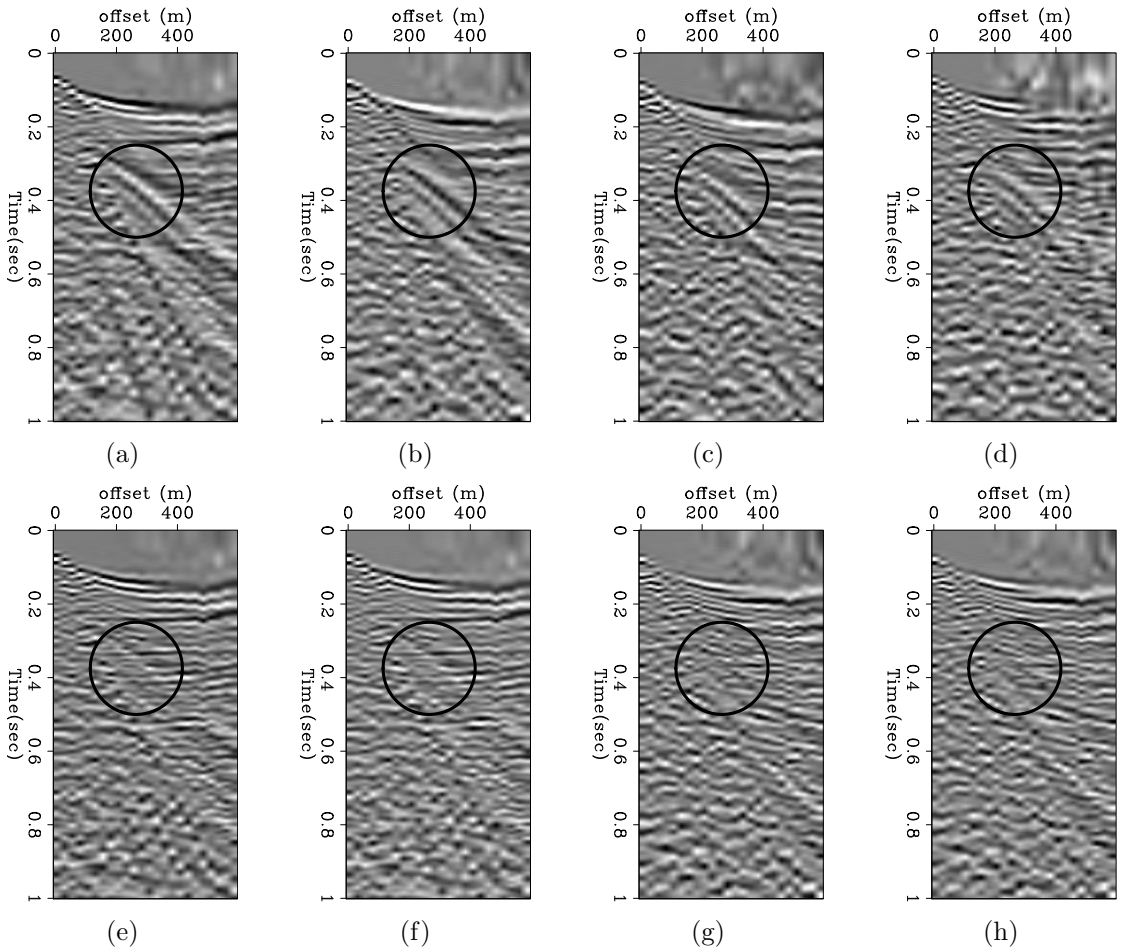

Figure 3.28: Comparison of polarization filtering of the shear-induced wave mode in the 50 m depth dynamite receiver gathers, when using the vertical (V_z), radial (V_x) and pitch (R_y) components as inputs vs when using the vertical (V_z), radial (V_x) and pitch (V_y) components as inputs. (a) The input vertical (V_z) component. (b) The input radial (V_x) component. (c) The input transverse (V_y) component. (d) The input pitch (R_y) component. (e) Vertical component after filtering using V_z, V_x, R_y components. (f) Vertical component after filtering using V_z, V_x, V_y components. (g) Radial component after filtering using V_z, V_x, R_y components. (h) Radial component after filtering using V_z, V_x, V_y components. Data are shown after NMO with velocity $v = 1700$ m/s to flatten the P-wave reflections. AGC with a window size of $t = 0.2$ s has been applied for display purposes. Comparing to (e) to (f) and (g) to (h), I observe that there are no significant differences between the filtering results with the pitch component vs the results using the transverse component, since the shear-induced wave mode is similarly apparent on both of these input receiver components. [**ER**] chap3/. 319a,319b,319c,319d,319e,319f,319g,319h

a dominant undesired wave mode visible in the data. Furthermore, the polarization of a particular wave mode can vary with time, offset or even with orientation of the data components. Therefore the polarization template selected for an undesired wave mode at a particular position in the data may not be similar to the same wave mode appearing at other positions in the data.

A more comprehensive method of identifying wave modes would be to classify the polarizations of all wave modes present in massive amounts of 3D seismic data, using a machine learning approach. I discuss the use of machine learning to automatically identify wave modes based using their continuous-wavelet polarizations in the following chapter.

ACKNOWLEDGEMENTS

I thank Chevron for releasing the Kettleman dataset and permitting me to publish it, and particularly Ranjan Dash for preparing the data for my use. The rotation sensors were provided by Geokinetics. I also thank Robert Brune for getting me interested in rotational seismic data, and having ongoing discussions with me on the subject. Bob also helped Chevron to include rotation sensors in the Kettleman survey, personally insuring that the sensors were wired and deployed correctly, and also wrote some of the survey logs which proved invaluable in processing the dataset.

Chapter 4

Automatic wave mode identification using machine learning

The previous chapter dealt with separating wave modes in a seismic gather, particularly surface waves, as based on a polarization template of a representative arrival of those wave modes. However, the polarization of any wave mode may depend on offset, azimuth or even on receiver coupling. Rather than manually selecting particular arrivals and targeting them for removal, a method that can automatically identify particular wave modes in large seismic datasets is required.

Manual interpretation of seismic data is slow and subjective, changing from one interpreter to another according to their experience and talent. I have opted to use a machine learning method in order to identify wave modes in multicomponent seismic data. The advantage of machine learning algorithms is that they may be used to automate many time-consuming manual tasks, making them an attractive prospect for the processing of large 3D seismic datasets.

INTRODUCTION

Machine learning algorithms are nothing new to geophyical exploration, and have been used for several geophysical processing applications. For example, Ronen et al.

(1994) and Zhao and Ramachandran (2013) use neural networks to derive a functional relationship between various attributes of seismic data and well-log properties. Kuzma and Rector (2005) train a support vector machine algorithm to approximate the results produced by a non-linear AVO inversion. Zhao et al. (2014) use support vector machines for lithofacies classification based on the waveforms of migrated seismic data from a shale play. They also use well-log data to complement the training of the support vector machines. Huang and Yang (2015) use neural networks to execute seismic velocity picking on semblance data. In this chapter, I use a support vector machine algorithm to identify ground roll on multicomponent data comprising both translational and rotational components.

In addition to reflections, seismic data include many other seismic responses that are either unwanted or unneeded, resulting in recorded data containing many different wave modes. In the case of land acquisitions, high-amplitude ground roll noise may obscure signal, degrading overall data quality. Ground roll can be spatially aliased and may be dispersive, resulting in non-linear moveout. Moreover, it is notoriously difficult to model with generality, making ground roll noise removal a tedious task in data processing and a challenge in survey design.

In chapter 3, I showed how to apply a filter that attenuates the first polarization vector of the data that have polarization signatures similar to a selected ground roll polarization template. However, this methodology requires manual picking of events on the data gather in order to define the polarization template. Moreover, there was an underlying assumption of stationarity of the wave modes along offset. There is no assurance that the polarization signature of a certain wave mode at a particular offset in the data will be similar at other offsets.

To automate and generalize the process of identifying wave modes in the data I use support vector machines (SVM), a machine learning algorithm designed to classify data vectors based on a training set of previously-supplied classifications. In chapter 3 I transformed multicomponent translational and rotational seismic data from the Kettleman field survey to the continuous wavelet domain, and then applied singular value decomposition to the transformed data. In this chapter, I manually classify gathers of a multicomponent receiver gather based on wave modes that I observe in the data. I the train the SVM on the continuous-wavelet polarization vectors of the classified training data, teaching it to identify the polarization vectors of a particular

wave mode from all other modes in the data. I then test the SVM's capability to classify wave modes on test data, where the various wave modes are clearly visible and the success of the classification can be properly gauged.

Though I judge the performance of the SVM classification based on a visual inspection of the spatial continuity of wave modes in the classified seismic gathers, I wish to emphasize that the classification method I describe does not rely on spatial sampling parameters, but rather only on multicomponent traces from single stations. Therefore, the method will work on spatially-aliased data, which in turn means that it can be used to reduce constraints of survey design.

PREPARING DATA FEATURES FOR MACHINE LEARNING

Support Vector Machines (SVM)

The polarization vectors obtained after applying a continuous wavelet transform (CWT) and singular value decomposition (SVD) as in equations 3.1 and 3.4 are used as input for classifying the different wave modes. From there, I treat the polarization vectors as "feature vectors", i.e., the training and testing data for a classification problem.

SVMs are a supervised learning algorithm that have been shown to perform well in a variety of settings, and are often considered one of the best "out of the box" classifiers. I used the Python library Scikit Learn to implement the SVM.

To train the classifier, I build a training dataset of N sample pairs, $(\mathbf{x_1}, y_1), (\mathbf{x_2}, y_2), \cdots, (\mathbf{x_N}, y_N)$. The $\mathbf{x_i}$ are vectors containing real numbers in the range $[0, 1]$, which represent the normalized polarization-vector values. The y_i are binary class labels and are equal to either 0 or 1, indicating to which wave mode class the polarization vector belongs, for example, whether the dominant wave mode is a surface or a body wave.

The support vector classifier determines the optimal hyperplane separating the two classes in the features space. If we define a hyperplane $f(x)$ by the following:

$$f(x) = x^T\beta + \beta_0 = 0, \tag{4.1}$$

where β is a unit vector with the length of the polarization vectors and β_0 a constant, the classification rule induced by $f(x)$ can be expressed as:

$$G(x) = \text{sign}[x^T\beta + \beta_0]. \tag{4.2}$$

A slack parameter $\xi = (\xi_1, \xi_2, \cdots, \xi_N)$ is used to account for the fact that the samples are not perfectly separable. With these notations, the support vector classifier for the nonseparable case is commonly expressed as:

$$\min_{\beta,\beta_0} \|\beta\| \quad \text{subject to} \begin{cases} y_i({x_i}^T\beta + \beta_0) \geq 1 - \xi_i\,, \ \forall i \\ \xi_i \geq 0, \ \forall i \quad \text{and} \quad \sum \xi_i \leq K. \end{cases} \tag{4.3}$$

By bounding the sum $\sum \xi_i$, we bound the total proportional amount by which predictions fall on the wrong side of their margin. Misclassifications occur when $\xi_i > 1$, so bounding $\sum \xi_i$ at a value K bounds the total number of training misclassifications at K.

However, the described support vector classifier is limited to finding linear boundaries in the input feature space. To achieve better training-class separation, we can remap the feature space to a higher dimensional space using preconditioning. Linear boundaries in the higher-dimensional space translate to nonlinear boundaries in the original space, thereby making the problem more flexible. Once the remapping basis functions $h_m(x)$, $m = 1, \cdots, M$ are selected, the procedure is the same as before. We fit the support vector classifier using input features $h(x_i) = (h_1(x_i), h_2(x_i), \cdots, h_M(x_i))$, $i = 1, \cdots, N$, and produce the (nonlinear) function $\hat{f}(x) = h(x)^T\hat{\beta} + \hat{\beta}_0$. The classifier is $\hat{G}(x) = \text{sign}[\hat{f}(x)]$ as before.

Hastie et al. (2005) show that we need not specify the transformation $h(x)$ at all, but require only knowledge of the following kernel function:

$$K(x, x') = \langle h(x), h(x') \rangle, \tag{4.4}$$

that computes the inner products in the transformed space. For particular choices of h, these inner products can be computed very cheaply. Three popular choices for K

in the SVM literature are shown in the following:

$$d^{\text{th}}\text{—Degree polynomial:} \quad K(x,x') = (1+\langle x,x'\rangle)^d, \tag{4.5}$$

$$\text{Radial basis:} \quad K(x,x') = \exp(-\gamma\|x-x'\|^2), \tag{4.6}$$

$$\text{Neural network:} \quad K(x,x') = \tanh(\kappa_1\langle x,x'\rangle + \kappa_2). \tag{4.7}$$

In this chapter, I use the radial basis kernel function for the classification. A more complete overview of the implementation of support vector machines can be found in Hastie et al. (2005).

SVM TRAINING AND TESTING WITH KETTLEMAN DATA

The 2D Kettleman survey was acquired by Chevron near Kettleman, California. It comprised multiple types of sources and multiple types of receivers, both on the surface and at depth. The shot line length was 1.6 km long. The seismic sources used were a vibroseis, an accelerated weight-drop, and buried dynamite charges at 25 m and at 50 m depth. At one end of the shot line there were five 3 component (3C) linear accelerometers, which were closely spaced at a 2.1 m interval inline. Additionally, near the center of the shot line there were two adjacent 3C geophones buried at 1 m depth, spaced at a 2 m interval inline. The survey also included 3C rotation sensors, which were placed in between the accelerometers and geophones, in the inline direction.

The survey geometry is shown in Figure 3.3, Figures 4.1(a)-4.1(f) show the receiver gathers at station 335 shot with the vibroseis source. Figure 4.1(a) is the vertical component, Figure 4.1(b) is the radial, Figure 4.1(c) is the transverse, Figure 4.1(d) is the yaw, Figure 4.1(e) is the roll, and Figure 4.1(f) is the pitch component. AGC has been applied for display.

Note that the signal to noise ratio of the rotation sensor data in Figures 4.1(d) and 4.1(e) is very low for offsets greater than 300 m. The same is true for the pitch component of the rotation sensor. Therefore, I derived the pitch component in Figure 4.1(f) by differencing the adjacent vertical accelerometers at station 335, as shown in equations 2.4. Since the receivers were arrayed only in the inline direction, I could not derive rotational data for the roll and yaw components as I did for the pitch

component. Consequently, the analysis here initially includes only the vertical, radial and transverse translational components, and the pitch rotational component derived by geophone-differencing for which the signal to noise ratio is sufficient.

The P body-wave reflections are visible at earlier times and longer offsets, but most of the gather is dominated by various modes of surface waves, which is typical to land data. There is a very slow Rayleigh wave mode propagating at around 250 m/s, and a faster mode propagating at 400 m/s, which are both labeled on Figure 4.1(a). Henceforth, I will refer to these wave modes as "slow" and "fast" ground roll. There is yet another, faster mode, propagating at 600 m/s - 700 m/s, which is not part of the analysis here.

The wave modes we are mostly interested in acquiring in exploration seismology are the P-wave reflections, since they contain information about the deep subsurface where our imaging targets are. Surface waves can be much stronger than the P-wave reflections on a seismic gather, and therefore obscure the reflections. Therefore, standard seismic processing requires that the surface waves (e.g. "ground-roll") be removed. However, as a first step, the unwanted energy must be identified. For large volumes of 3D seismic data, it would be extremely advantageous to have a machine learning algorithm automatically identify all the source-generated noise in the data.

SVM training data for classification of surface waves

In order to separate the surface waves from the body waves, I train an SVM classifier on the data from receiver station 335, shown in Figures 4.1(a) to 4.1(f). I decompose the training data into scaled continuous-wavelet polarization vectors by applying CWT followed by SVD, as in equations 3.1 and 3.4.

I start the analysis using only the vertical, radial and pitch components, since these seem to contain most of the coherent energy in the data. Since I am using three data components, for each offset and each time sample I obtain three polarization vectors. I use only the first polarization vector as the input feature vector for the SVM classification, since most of the energy is contained within the first vector.

As an example of a what the feature vectors look like, I select the trace at offset 180 m from Figures 4.1(a), 4.1(b) and 4.1(f), i.e., the vertical, radial and pitch components. After application of CWT and SVD, the normalized feature vectors

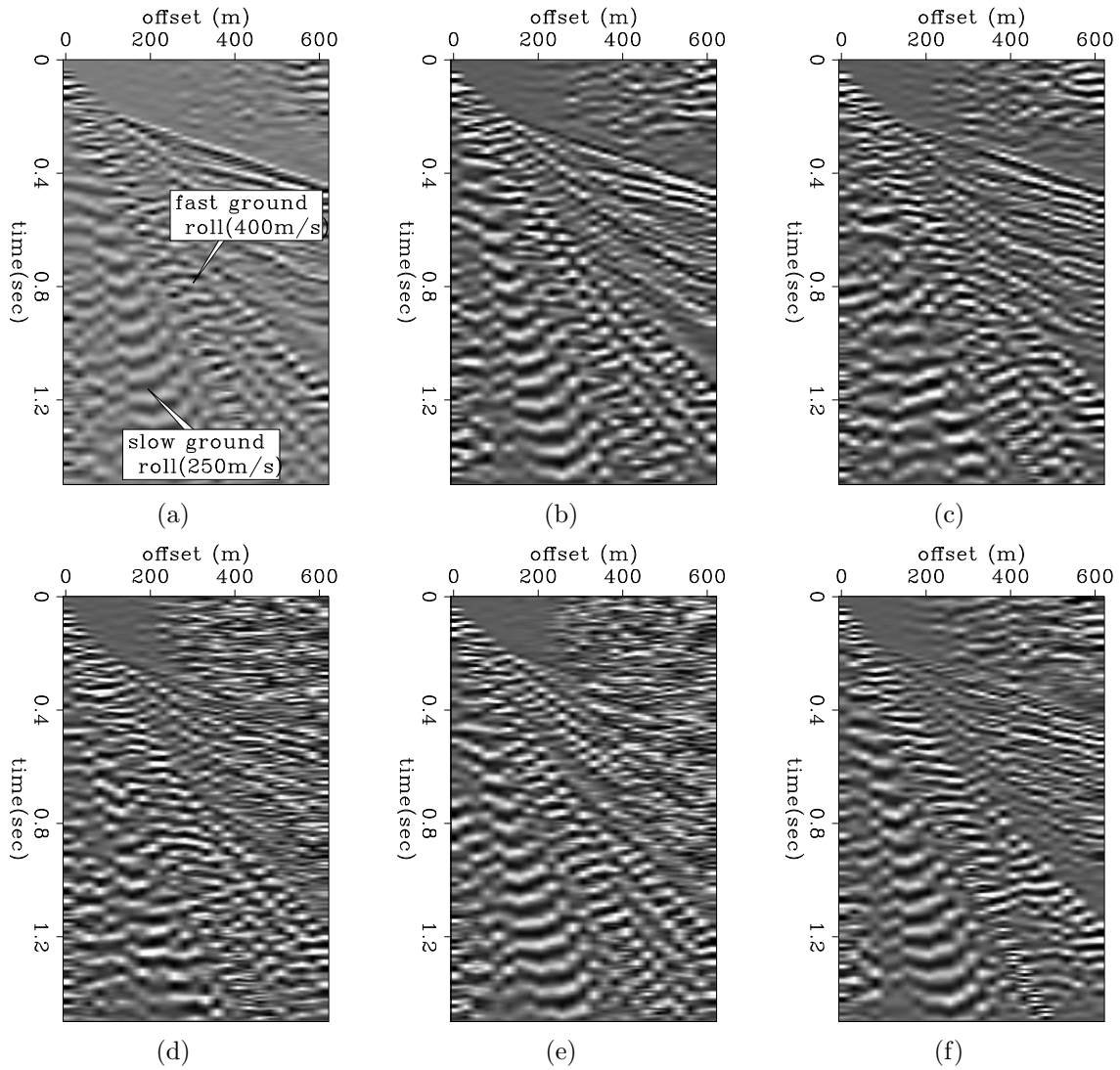

Figure 4.1: Receiver gathers at station 335 for the vibroseis source. a) Vertical accelerometer component. b) Radial accelerometer component. c) Transverse accelerometer component. d) Yaw rotation-sensor component e) Roll rotation-sensor component f) Pitch component derived from differencing two adjacent inline vertical accelerometers. AGC has been applied for display. Note the various types of surface wave modes present, as annotated on (a), but are recorded on all components. The yaw and the roll rotation-sensor components have very low SNR at increasing offsets, and therefore I did not use them in the analysis presented here. [**ER**] chap4/. 401a,401b,401c,401d,401e,401f

for the multicomponent trace at offset 180 m are illustrated in Figure 4.2(a). In this figure, the continuous-wavelet polarization vector coefficients are renamed as "feature vectors". At earlier times, which correspond mainly to P-wave reflection energy, the maxima of the feature vectors are at lower values of feature index. At later times, which correspond to surface-wave energy, the maxima of the feature vectors are at higher values of feature index.

Figure 4.2(b) represents the same feature vectors for the trace at offset 180 m. The feature vectors corresponding to the slow ground roll are color-coded in red, and the feature vectors of all other wave modes in this trace are color coded in blue. We can see a very clear distinction between the slow ground roll and the other types of wave modes in the feature space, which is indicative of the different seismic signatures that the wave modes have in the multicomponent data. When I train the SVM classifier, it is similar to manually color-coding the feature vectors by the wave modes they represent, as is shown in Figure 4.2(b).

In order to train the classifier, I label the training data manually by selecting particular wave modes in the data from receiver station 335. The selection was done using a linear mute function that windowed only the ground-roll energy. Figures 4.3(a), 4.3(b) and 4.3(c) illustrate which regions were labeled as slow ground roll, fast ground roll and total ground roll. For each of these selected wave modes, I trained an SVM classifier using the aforementioned polarization feature vectors as input. The ground roll is labeled as "Class 1", while all the other wave modes are labeled as "Class 0".

I then test the SVM's classification capability on the same training data. The classification results obtained on the training data are illustrated in Figures 4.3(d), 4.3(e) and 4.3(f). They are highly similar to the hand-picked labels, indicating that the classifiers fit the training data well, with a low training error.

SVM classification of surface waves on test data

Testing on other receiver stations

After validating that the classification works on the training dataset, I tested the previously trained classifiers on test data from other receiver stations for the same vibroseis source type.

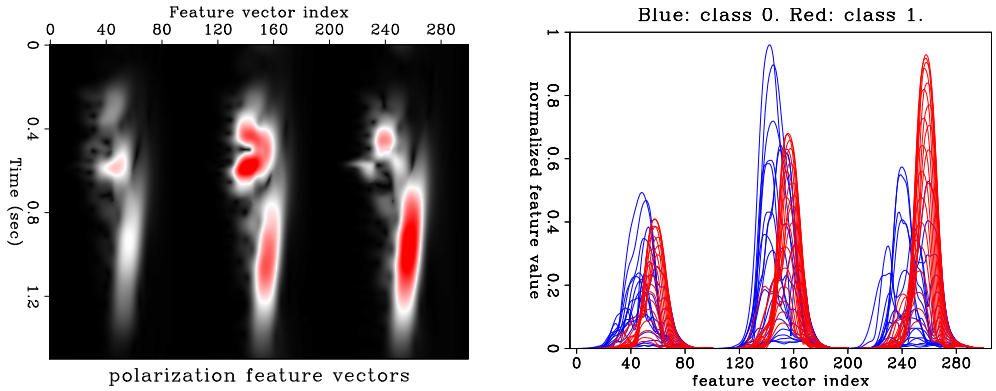

(a) (b)

Figure 4.2: The training data at receiver station 335 for the SVM. a) Feature vectors for each time sample for the multicomponent trace at offset 180m. b) The same feature vectors color coded by their respective classification, 'Class 1' being the slow ground roll mode and 'Class 0' representing everything else. Note the differences between the feature vectors of each class. These feature vectors and their respective labels indicating the wave mode are the input to the SVM training. [**ER**] chap4/. Vib65-st335-3ct-features-V1-off180a,Vib65-st335-3ct-features-V1-off180b

Stations 336 and 337 are adjacent to stations 335 (the training data station) near the end of the shot line, and therefore the data at these receiver stations should be similar to the training data. This similarity between the data at the different stations enables us to estimate how well the classifier identifies the ground roll wave mode on these test data.

Figure 4.4(g) is the vertical component at station 336. Figures 4.4(a), 4.4(c) and 4.4(e) are the classified slow ground roll, fast ground roll and combined slow+fast ground roll wave modes at this station, respectively. Figures 4.4(b), 4.4(d) and 4.4(f) are the complementary data, i.e., the input data minus the data classified as ground roll. While Figures 4.4(a), 4.4(c) and 4.4(e) show what the SVM has classified as 'Class 1', Figures 4.4(b), 4.4(d) and 4.4(f) show what it has classified as 'Class 0'.

Recall that this classification is done using the classification generated by training the SVM on the labeled vertical, radial and pitch components at station 335. Observe that the classifier has managed to identify the ground roll in these test data relatively well, and, more importantly, it does not misclassify the body wave energy as ground roll in any one of the cases shown.

The classification seems to be better when both ground roll modes are combined,

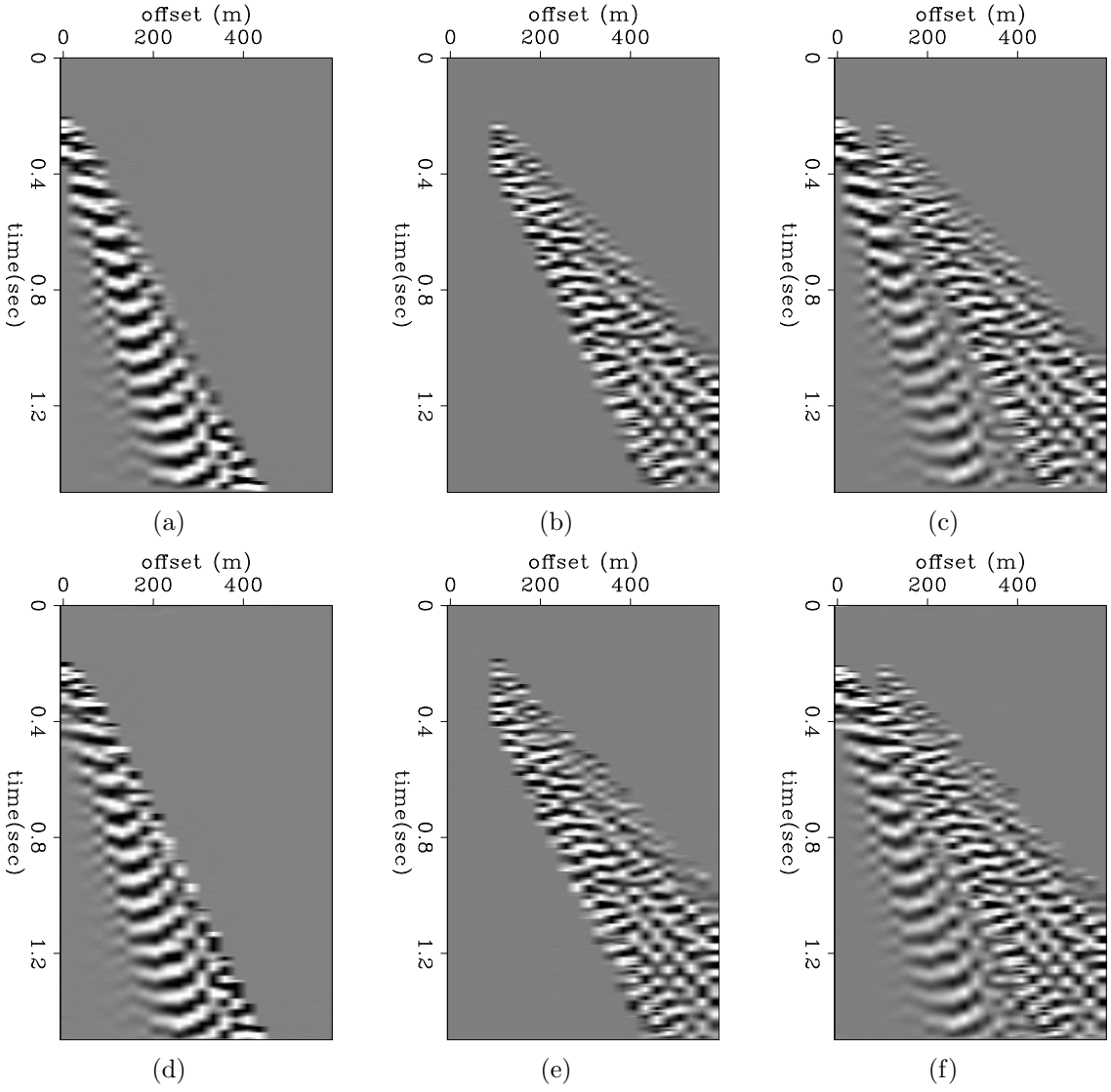

Figure 4.3: SVM training data at station 335, and testing results on the same training data, for the vibroseis source. Only the vertical component is shown, although the training data comprised the vertical, radial and pitch components. a) Slow ground roll mode training data. b) Fast ground roll mode training data. c) Slow+fast ground roll modes training data. d) Testing classification of slow ground roll mode on training data. e) Testing classification of fast ground roll mode on training data. f) Testing classification of slow+fast ground roll modes on training data. [**ER**] chap4/. 403a,403b,403c,403d,403e,403f

as shown in Figure 4.4(e) and 4.4(f). It seems that it is more difficult for the classifier to differentiate between the two types of ground roll (slow vs fast) than between the ground roll and body waves. I attribute this to the fact that there is more similarity between the polarizations of the two ground roll modes than between the polarizations of either ground roll mode and the body waves.

Figure 4.5(g) is the vertical component at station 337. The same conclusions for the classification results at station 336 can be drawn for the classification results for station 337, shown in Figures 4.5(a) to 4.5(f).

Station 191 is about 1 km away from station 335. At station 191 there were geophones installed, rather than accelerometers as at stations 335,336 and 337. Furthermore, the geophones were buried at 1 meter depth, whereas at stations 335,336 and 337 the accelerometers were on the surface.

Figure 4.6(g) is the vertical component at station 191. Figures 4.6(a), 4.6(c) and 4.6(e) are the classified slow ground roll, fast ground roll and combined slow+fast ground roll wave modes at station 191, respectively. Figures 4.6(b), 4.6(d) and 4.6(f) are the complementary data, i.e., the input data minus data classified as ground roll.

The classifier seems to have more difficulty differentiating between the slow and the fast ground roll modes at this station. Additionally, it has misclassified a small portion of the body wave energy as ground roll, as can be seen on the left Figure 4.6(e) at $t = 0.4$ s. However, by and large the classification does enable the identification of ground roll energy, despite the acquisitional differences between the data at station 191 vs station 335, on which I trained the SVM.

Testing on other source types

The next test I did was on the same station that provided the training data (335), but for alternate seismic source types. Figures 4.7(a), 4.7(b) and 4.7(c) are again the receiver gather of the vertical component at training station 335, training classification of the slow+fast ground roll ('Class 1'), and the training of the body waves ('Class 0') for these training data, respectively.

Figure 4.7(d) is the receiver gather of the vertical component at station 335 for

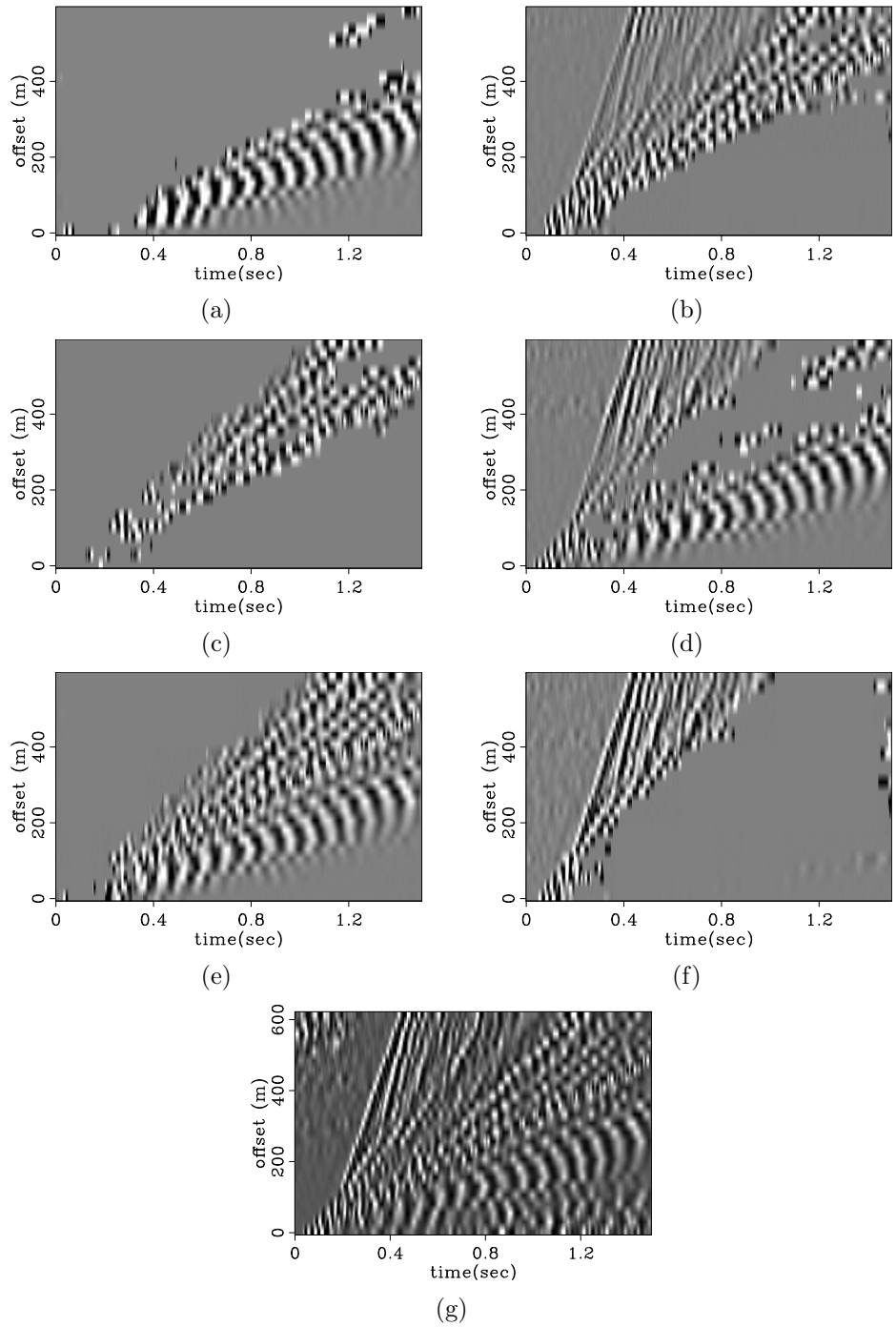

Figure 4.4: SVM classification of surface wave modes on test data at station 336, for the vibroseis source. Only the vertical component receiver gather is shown, although the training and test data comprised the vertical, radial and pitch components. g): Input vertical component at station 336. a): classification of slow ground roll mode. b): Complementary data to (a) (i.e., (g) - (a)). c): classification of fast ground roll mode. d): Complementary data to (c) (i.e., (g) - (c)). e): classification of slow+fast ground roll. f): Complementary data to (e) (i.e., (g) - (e)). [**ER**] chap4/. 404a,404b,404c,404d,404e,404f,404g

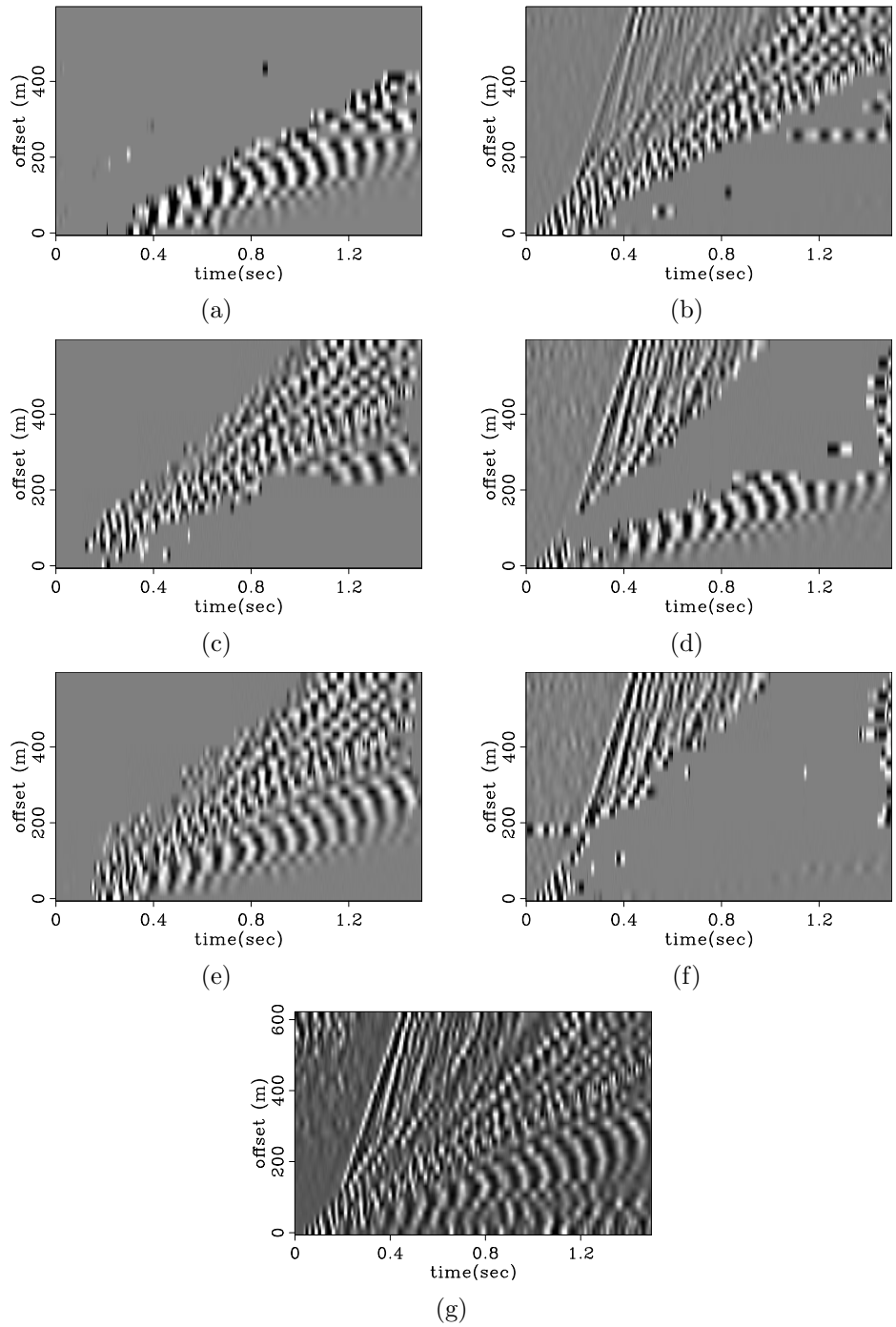

Figure 4.5: SVM classification of surface wave modes on test data at station 337, for the vibroseis source. Only the vertical component receiver gather is shown, although the training and test data comprised the vertical, radial and pitch components. g): Input vertical component at station 337. a): classification of slow ground roll mode. b): Complementary data to (a) (i.e., (g) - (a)). c): classification of fast ground roll mode. d): Complementary data to (c) (i.e., (g) - (c)). e): classification of slow+fast ground roll. f): Complementary data to (e) (i.e., (g) - (e)). [**ER**] chap4/. 405a,405b,405c,405d,405e,405f,405g

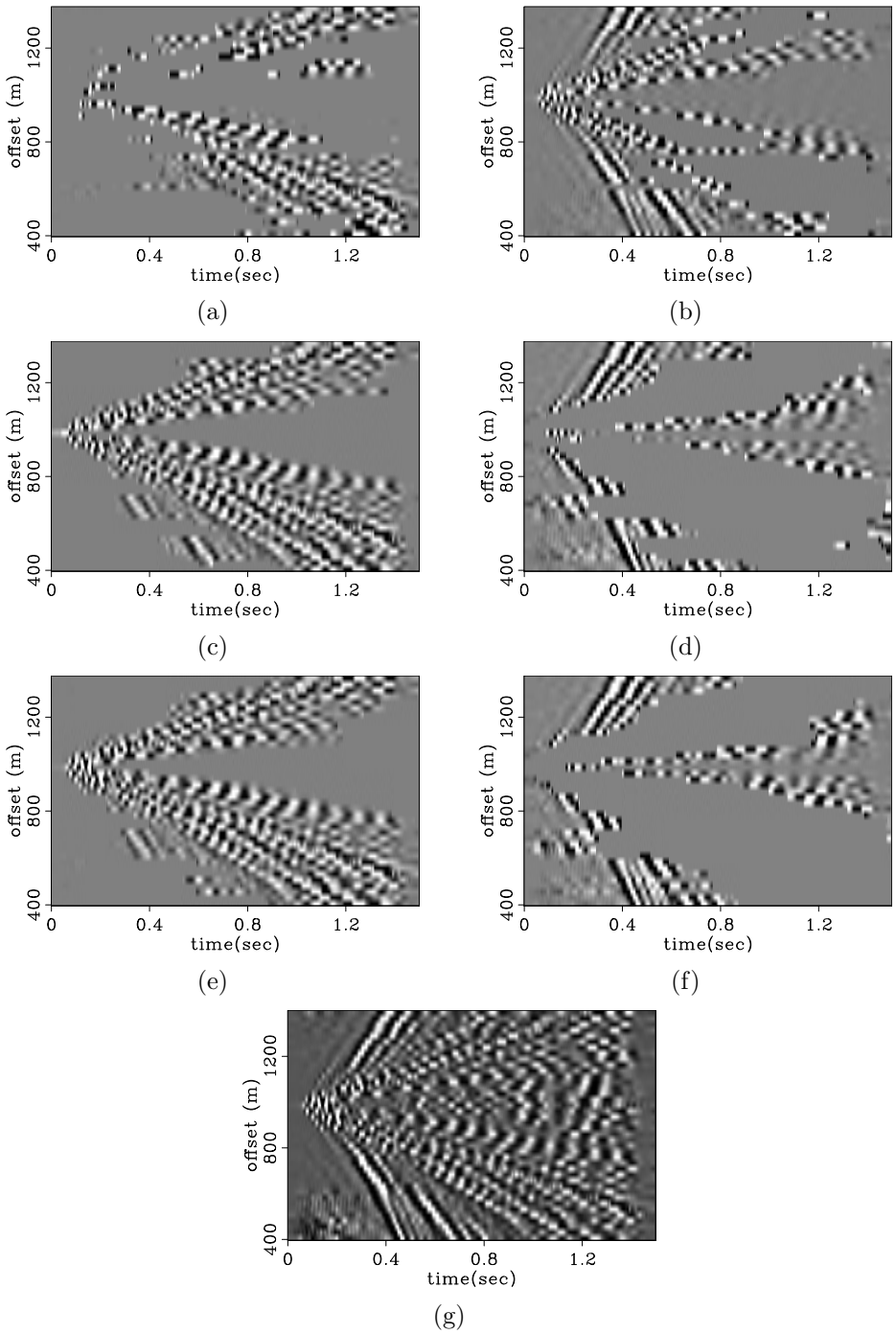

Figure 4.6: SVM classification of surface wave modes on test data at station 191, for the vibroseis source. Only the vertical component receiver gather is shown, although the training and test data comprised the vertical, radial and pitch components. g): Input vertical component at station 191. a): classification of slow ground roll mode. b): Complementary data to (a) (i.e., (g) - (a)). c): classification of fast ground roll mode. d): Complementary data to (c) (i.e., (g) - (c)). e): classification of slow+fast ground roll. f): Complementary data to (e) (i.e., (g) - (e)). [**ER**] chap4/. 406a,406b,406c,406d,406e,406f,406g

an accelerated weight-drop source. Note that the sampling for this source type was much denser than the vibroseis source. The ground roll wave modes visible in this gather are similar to those in Figure 4.7(a), however they are not aliased. Figure 4.7(e) shows the SVM's classification of the slow+fast ground roll modes ('Class 1') for the accelerated weight drop data, after training on the vibroseis data. Figure 4.7(f) shows the complementary data ('Class 0'), which is the input data at 4.7(e) minus the data classified as ground roll in Figure 4.7(f). Despite the fact that the source type is different, the classification is able to correctly classify the ground roll in this gather. Figure 4.7(e) is remarkably similar to Figure 4.7(b), albeit with a better sampling.

Both the vibroseis and the accelerated weight-drop source were on the surface. Figure 4.7(g) is the receiver gather at station 335, but for a dynamite source buried at 25 m depth. The ground roll energy has a different appearance in this gather. Figure 4.7(h) is the SVM classification of the slow+fast ground roll wave mode ('Class 1') for the dynamite source, after training on the vibroseis data. Figure 4.7(i) shows the complementary data ('Class 0'), which is the input data at 4.7(g) minus the data classified as ground roll in Figure 4.7(h). Note that the energy classified as ground roll does indeed seem to have the same linear moveout as the ground roll in the vibroseis gather. The classifier even picks up on a portion of a faster surface wave mode that does not appear in the vibroseis data.

In both test cases shown in Figures 4.7(e) to 4.7(g) and 4.7(h) to 4.7(i), there is no misclassification of the body wave energy as ground roll.

Comparison of different components used in SVM classification

So far I have shown the SVM classification results using the vertical, radial and pitch components. I now compare the classification results using varying numbers and types of components used in the training and classification.

Figure 4.8(a) shows the feature vectors derived from the trace at offset 180m at training station 335, for the vertical and radial components. The feature vectors in red are from a time window where ground roll is dominant, and the feature vectors in blue are from the rest of the trace. In Figure 4.8(b), I have added the transverse

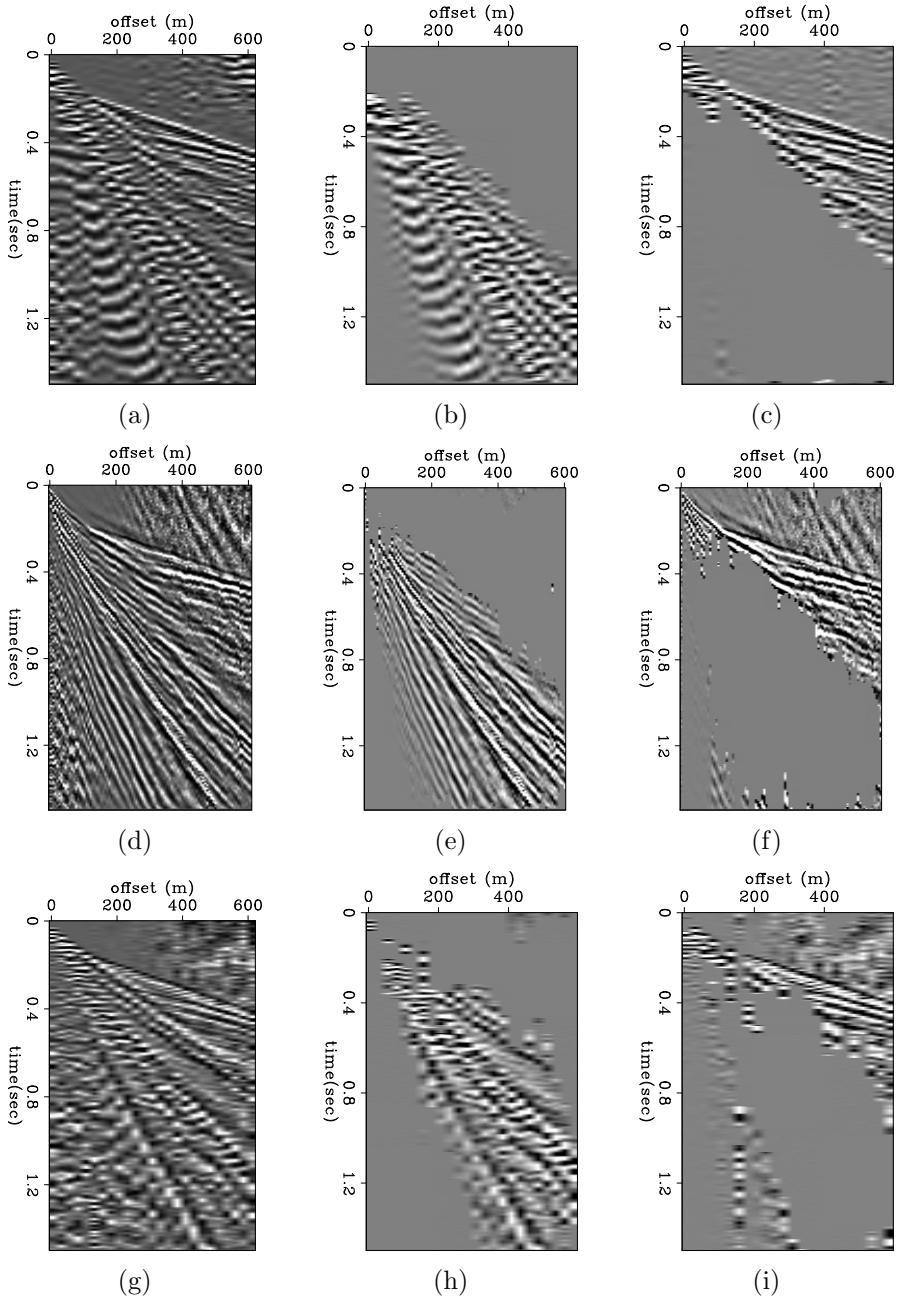

Figure 4.7: SVM classification of surface wave modes at station 335, for different seismic source types. Only the vertical is shown, although the training and test data comprised the vertical, radial and pitch. a) Vertical of vibroseis source. b) The portion slow+fast ground roll mode labeled as class 1 from the vibroseis source data used to train the SVM. c) The complementary data containing body waves labeled as class 0 from the vibroseis source data used to train the SVM. d) Vertical of accelerated weight-drop source. e) classification of slow+fast ground roll mode for the accelerated weight-drop source using the SVM trained on the vibroseis data. f) classification of the complementary data for the accelerated weight-drop source using the SVM trained on the vibroseis data. g) Vertical of dynamite source. h) classification of slow+fast ground roll mode for the dynamite source using the SVM trained on the vibroseis data. i) classification of the complementary data for the dynamite source using the SVM trained on the vibroseis data. [**ER**]

chap4/. 407a,407b,407c,407d,407e,407f,407g,407h,407i

component to the feature vectors. Observe how now the feature vector is longer, and there is another indication for the difference between the wave-mode classes. The same can be said for the addition of the pitch component to the feature vectors in Figure 4.8(c).

Adding independent components to the feature vectors should improve the classification capability of the SVM. Figure 4.9(a) shows the classification of the slow+fast ground roll modes at station 191, where the training was done on 4 components of station 335: the vertical, radial, transverse and pitch components. Figure 4.9(d) shows the complementary data, i.e., what has not been classified as either slow or fast ground roll. Note that in Figure 4.9(a), the SVM has indeed managed to identify the ground roll, and there is only slight misclassification of the body wave energy as ground roll. The top of Figure 4.9(d) shows continuous body waves.

In Figure 4.9(b), only the vertical, radial and transverse components were used for training the SVM, and more of the body wave energy has been misclassified as ground roll. This can be seen in the complementary data in Figure 4.9(e) as a slight discontinuity in the classified body waves on the left of the figure at $t = 0.4$ s. For Figures 4.9(c) and 4.9(f), only the vertical and radial components were used for training the SVM. We observe that using only two components, even more of the body wave energy has been misclassified as ground roll. The SVM indeed performs better when the input feature vectors contain more information regarding the two classes we expect it to differentiate between.

Wave-mode classification using pitch vs using transverse component

I now test whether one set of components is better for identifying a wave mode than another set of components. Particularly, I compare using the transverse component in the classification vs using the rotational pitch component. Figure 4.10(a) is the vertical geophone receiver gather, showing the classification of the slow ground roll mode at test station 336, where the training was done on the vertical, radial and pitch components of station 335. Compare this figure to the classification result shown in Figure 4.10(b), where the training was done on the vertical, radial and transverse components of station 335.

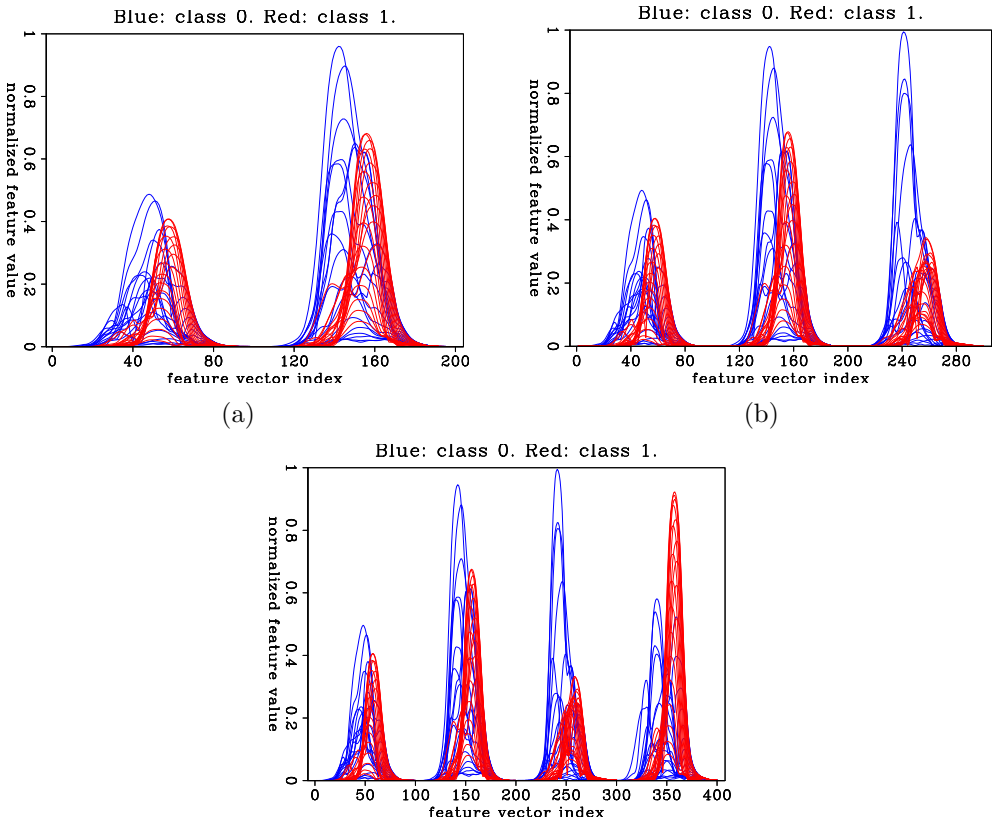

Figure 4.8: The input training feature vectors at training station 335 for trace at offset 180m, for a varying number of components used in the training. The classification is color-coded. The slow ground roll mode is 'Class 1' (red) and everything else is 'Class 0' (blue). a) Vertical and radial components. b) Vertical, radial and transverse components. c) Vertical, radial, transverse and pitch components. The more components used, the longer is the feature vector, and more differences can be discerned between the feature vectors of the two wave modes. [**ER**] chap4/. 408a,408b,408c

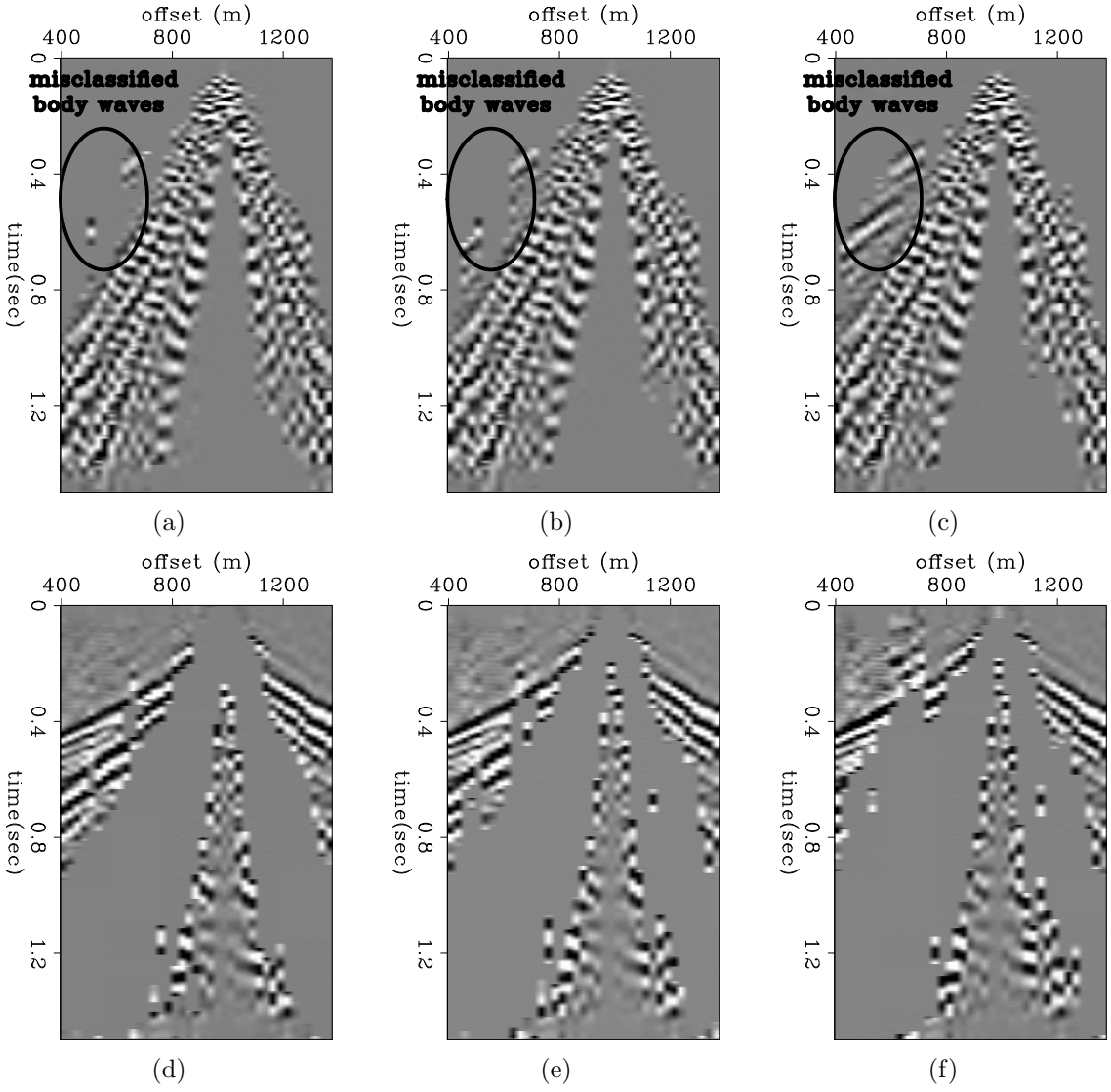

Figure 4.9: SVM classification of surface wave modes at testing station 191, for a varying number of receiver components used in training the SVM at station 335. a) Classification of slow+fast ground roll using vertical, radial, transverse and pitch components; b) using vertical, radial and transverse components; c) using only vertical and radial components. d,e,f) The complementary data to (a), (b) and (c), which are classified as body waves. For this receiver gather, adding more components in the SVM training improves the classification of the surface waves vs the P waves. [**ER**]
chap4/. 409a,409b,409c,409d,409e,409f

I observe that using the vertical, radial and transverse component in the training and classification of the slow ground roll mode has produced a better classification result than when using the vertical, radial and pitch components. There seems to be less misclassified energy in Figure 4.10(b) vs Figure 4.10(a).

A Similar conclusion can be reached for the classification results of the fast ground roll mode shown in Figure 4.10(c) vs Figure 4.10(d). Again, in Figure 4.10(d), where I used the vertical, radial and transverse components, the classification of the fast ground roll mode seems to be more complete than when using the vertical, radial and pitch components as shown in Figure 4.10(c).

I make a similar comparison for the receiver gather at test station 191. Figure 4.11(a) is the vertical geophone receiver gather, showing the classification of the slow ground roll mode at test station 191, where the training was done on the vertical, radial and pitch components of station 335. It seems that the SVM has misclassified most of the fast ground roll as slow ground roll, and has missed out on a large part of the actual slow ground roll. Figure 4.11(b) shows the classification of the slow ground roll at station 191 where the training was done on the vertical, radial and transverse components of the training station 335. Although there is a fair bit of misclassification of the fast ground roll as slow ground roll, compared to Figure 4.11(a) we can see that at least the slow ground roll has been identified.

Figure 4.11(c) is the vertical geophone receiver gather, showing the classification of the fast ground roll mode at test station 191, where the training was done on the vertical, radial and pitch components of station 335. Note that both the fast and the slow ground roll have been classified as fast ground roll, including some of the body-wave energy. However, when using the vertical, radial and transverse components in the training, the classification results of the fast ground roll wave mode is better, as shown in Figure 4.11(d). However, there is still some misclassification of the body-wave energy as fast ground roll.

DISCUSSION

Standard seismic processing may utilize some known attributes of ground roll to identify it. For example, ground roll have a much slower moveout than body waves in shot or receiver gather domains. Additionally, in multicomponent data the elliptical

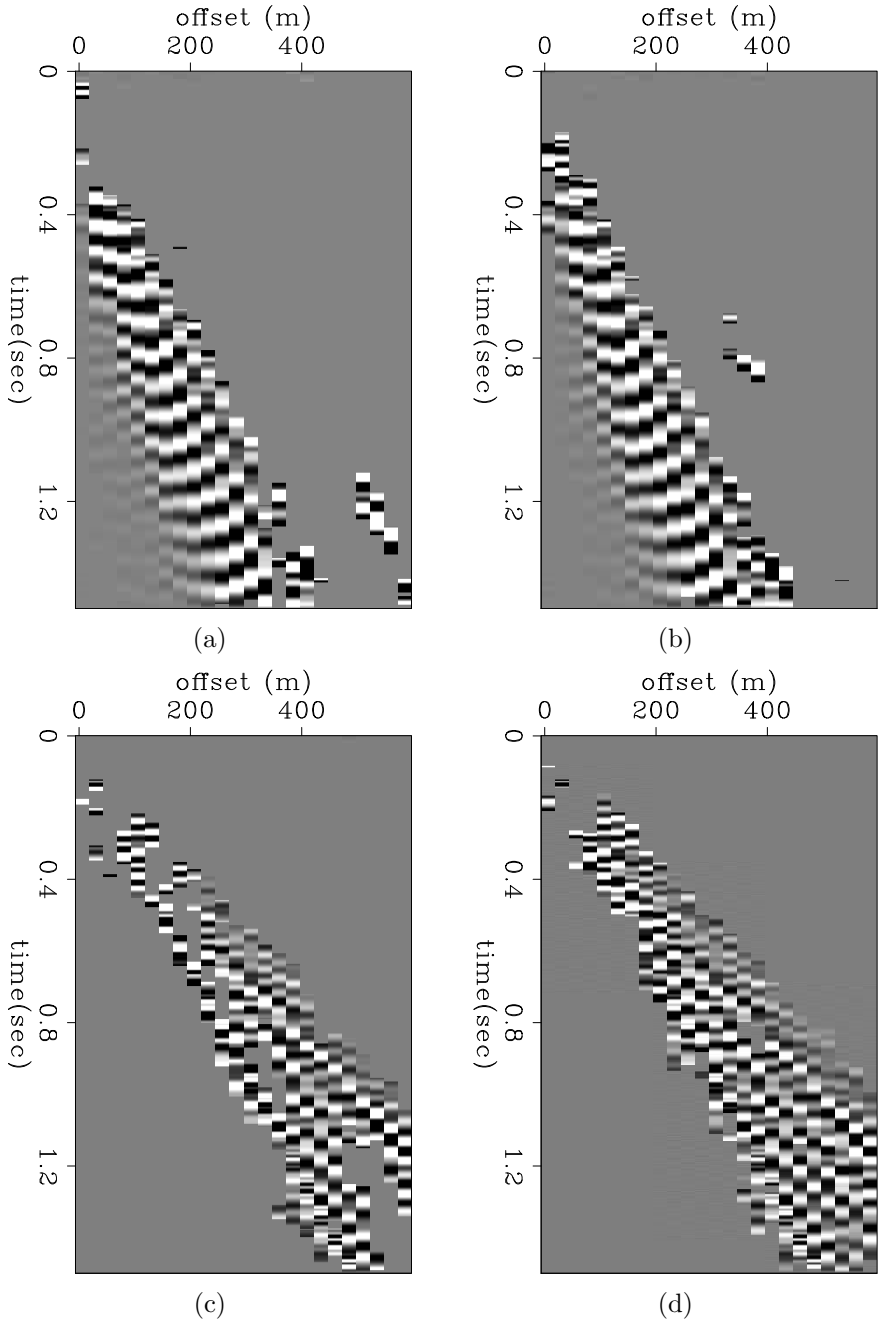

Figure 4.10: SVM classification of slow vs fast ground roll modes at testing station 336, for different components used in training the SVM at station 335. a) Classification of slow ground roll using vertical, radial and pitch components; b) using vertical, radial and transverse components. c) Classification of fast ground roll using vertical, radial and pitch components; d) using only vertical and radial and transverse components. For this receiver gather, the SVM does a better job differentiating between the slow and fast ground roll modes when using the transverse component rather than the pitch. [**ER**] chap4/. 410a,410b,410c,410d

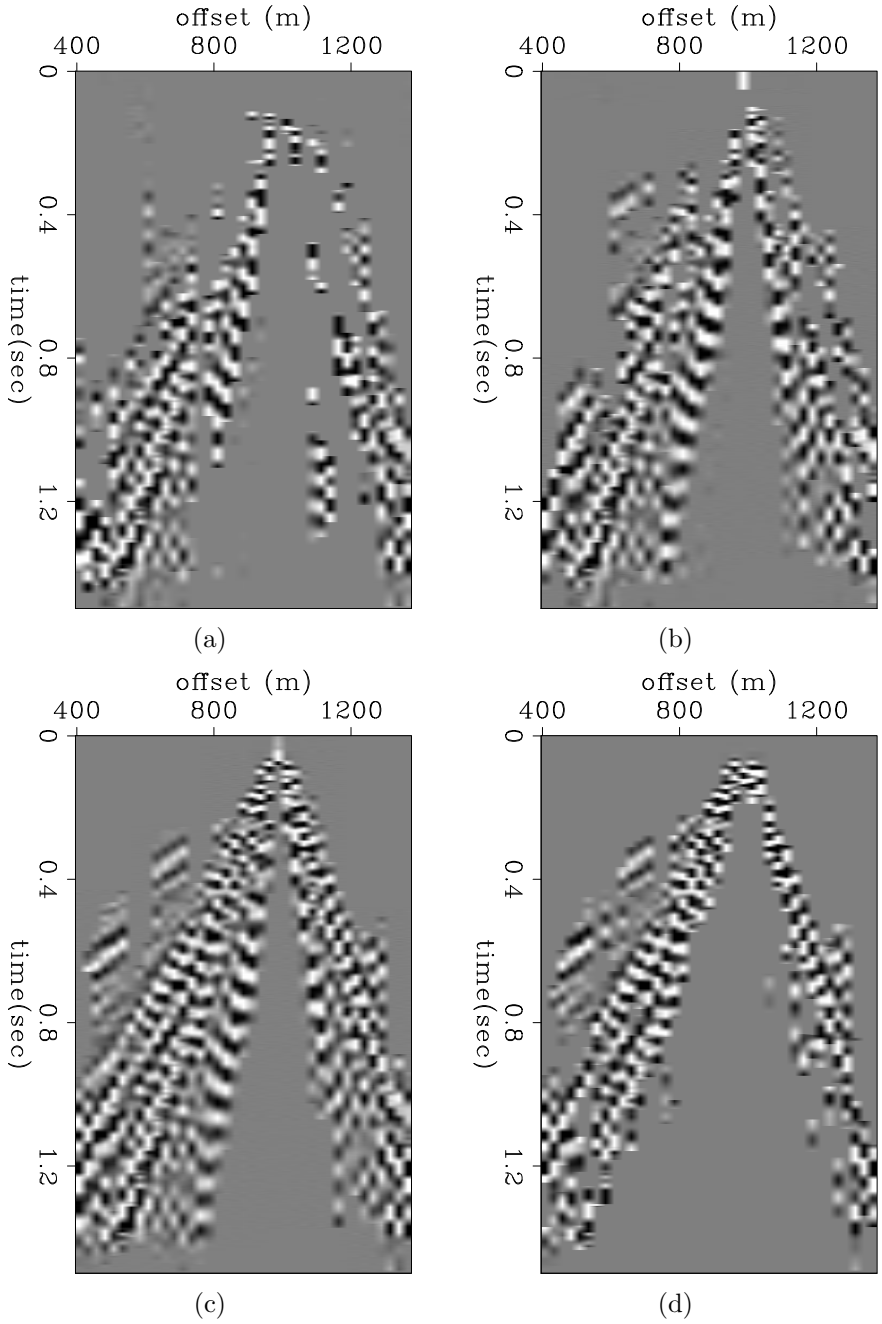

Figure 4.11: SVM classification of slow vs fast ground roll modes at testing station 191, for different components used in training the SVM at station 335. a) Classification of slow ground roll using vertical, radial and pitch components; b) using vertical, radial and transverse components. c) Classification of fast ground roll using vertical, radial and pitch components; d) using only vertical and radial and transverse components. For this receiver gather, the SVM does a better job differentiating between the slow and fast ground roll modes when using the transverse component rather than the pitch. [**ER**] chap4/. 411a,411b,411c,411d

polarization associated with Rayleigh waves may be employed to identify ground roll.

The approach of machine learning is very different however. Where standard methods use an a priori, analytical model of ground roll (such as moveout or elliptical polarization), a machine learning approach does away with any predetermined physical model, and substitutes it for a model learned from the data themselves. The advantage of such an approach is that it may work in cases where a useful, representative physical model is beyond our initial, a-priori capability to obtain analytically.

The case of surface waves (ground roll) is of particular interest in this respect, since the near surface of the Earth is commonly very complex, and in general it is difficult to accurately model wave propagation in the near surface. For example, Rayleigh waves do not always have elliptical polarization, nor is their moveout necessarily predictable. Surface waves may also be generated by body waves inciding on near surface scatterers, in addition to being radiated directly away from the source position. Therefore, the prospect of enabling an algorithm to learn from the data what the source-generated ground roll noise may look like in multiple scenarios is compelling.

I have used the continuous-wavelet polarization vectors of multicomponent seismic data to train an SVM algorithm to identify ground roll. The classification results using the test data indicate that the SVM is indeed able to identify ground roll based on this (rather minimal) training. The method is effectively immune to spatial aliasing, making it useful for 3D seismic data with arbitrary acquisition patterns.

I have shown that adding the rotational pitch component to the standard set of three geophone components improves the SVM's capability to classify the ground roll vs the body waves. I also show that for differentiating between the two dominant types of ground roll visible in the Kettleman data, using the vertical, radial and transverse geophone components in the training and classification is better than using the vertical, radial and pitch components. I attribute this to the generally lower SNR levels in the pitch component derived either from geophone differencing (which inherently lowers SNR), or from the R2 rotation sensors themselves. The transverse component of motion of the slow ground roll is sufficiently different from the transverse motion of the fast ground roll so as to enable the SVM to tell them apart.

However, there are several open questions with respect to practical application of this machine learning algorithm:

1. In order to have a good representation of the various ways each wave mode may be polarized at multiple times/offsets/azimuths (given a set of data components), massive amounts of seismic data are required. How would we manually classify and train a machine learning algorithm to identify particular wave modes in large quantities of data?

2. Can an SVM trained on a particular dataset be used for classification of another dataset?

3. Are more components necessarily better for the SVM's classification of wave modes?

4. Would an unsupervised machine learning algorithm identify wave modes better than a supervised one such as SVM?

The Kettleman dataset is instrumental in showing the possibility of identifying wave modes in land data using machine learning, since it has multiple components, both translational and rotational, which enable enhanced wave-mode identification by polarization. However, the Kettleman dataset is very small. Machine learning methods generally rely on large volumes of data for training and evaluating test results. To properly answer the questions above, I would require a very large, 3D multicomponent land or OBS dataset.

I can speculate, however, that an SVM trained on one dataset would be unable to classify wave modes accurately in a dataset acquired over a region with very different geology. This would be the result of the general complexity of the seismic response in the different scenarios, but also of the differences in acquisition such as different source signatures, different receivers and different couplings. I would also say that having more independent data components should help the classification of wave modes, assuming that the noise levels are similar for each data component.

The support vector machine algorithm was able to identify the ground roll based on the polarization vectors of the multicomponent data in the continuous wavelet domain. Since the wave modes are indeed separable by their polarization vectors, I think that an unsupervised machine learning algorithm would do just as well if we provide it with the same polarization vectors. For a large volume of seismic data, an unsupervised learning algorithm would be preferable, since it would solve the problem,

stated in question 1 above, of manually classifying portions of the data to train a supervised learning algorithm. Two possible candidate classification algorithms are K-means and Neural Networks.

ACKNOWLEDGEMENTS

I thank Chevron for permission to use the Kettleman dataset. I also thank Fantine Huot for suggesting I look into Support Vector Machines as a classification algorithm and helping me understand the theory behind them.

Bibliography

Aki, K. and P. G. Richards, 2002, Quantitative seismology, 2nd ed.: University Science Books, **1**.

Aldridge, D. F. and R. E. Abbott, 2009, Investigating the point seismic array concept with seismic rotation measurements: Sandia National Lab Report.

Aldridge, D. F., N. P. Symons, and L. C. Bartel, 2007, Comparison of poroelastic and elastic fullwaveform avo responses: SEG Technical Program Expanded Abstracts, 2070–2074.

Anstey, N. A., 1986, Part 1: Whatever happened to ground roll?: The Leading Edge, **5**, 40–45.

Bale, R. A. and R. Stewart, 2002, The impact of attenuation on the resolution of multicomponent seismic data: SEG Technical Program Expanded Abstracts.

Barak, O., F. Herkenhoff, R. Dash, P. Jaiswal, J. Giles, S. de Ridder, R. Brune, and S. Ronen, 2014, Six-component seismic land data acquired with geophones and rotation sensors: Wave-mode selectivity by application of multicomponent polarization filtering: The Leading Edge, **33**, 1224–1232.

Barr, F. and J. Sanders, 1989, Attenuation of water column multiples using pressure and velocity detectors in a water bottom cable: SEG Technical Program Expanded Abstracts, 653–656.

Blausen, B., 2014, Blausen gallery: Wikiversity Journal of Medicine, DOI:10.15347/wjm/2014.010. ISSN 20018762.

Boue, P., M. Denolle, N. Hirata, S. Nakagawa, and G. C. Beroza, 2016, Beyond basin resonance: characterizing wave propagation using a dense array and the ambient seismic field: Geophysical Journal International, **206**, 1261–1272.

British Geological Survey, accessed on May 2014, http://www.geomag.bgs.ac.uk/data_service/models_compass/wmm_calc.html: Online World Magnetic Model Calculator.

Brokesova, J. and J. Malek, 2015, Six-degree-of-freedom near-source seismic motions ii: Examples of real seismogram analysis and s-wave velocity retrieval: Journal of Seismology, **19**, 511–539.

Brune, R., D. Aldridge, M. van der Baan, J. Gaiser, and E. Muyzert, 2012, Theta-data: Introduction to rotational seismology and its potential uses: Presented at the 82nd Annual International Meeting, SEG.

Cowles, C. S., 1984, Rotational geophone: US Patent 4,446,541.

Craft, K. and J. Paffenholz, 2007, Geophone noise attenuation and wavefield separation using a multidimensional decomposition technique: SEG Technical Program Expanded Abstracts, 2630–2634.

Daubechies, I., 1990, The wavelet transform, time-frequency localization and signal analysis: IEEE transactions on information theory, **36**, 961–1005.

de Meersman, K., M. van der Baan, and J. Kendall, 2006, Signal extraction and automated polarization analysis of multicomponent array data: Bulletin of the Seismological Society of America, **96**, 2415–2430.

Diallo, M., M. Kulesh, M. Holschneider, F. Scherbaum, and F. Adler, 2006, Characterization of polarization attributes of seismic waves using continuous wavelet transforms: Geophysics, **71**, V67–V77.

Diebel, J., 2006, Representing attitude: Euler angles, unit quaternions, and rotation vectors.

Donno, D., A. Nehorai, and U. Spagnolini, 2008, Seismic velocity and polarization estimation for wavefield separation: IEEE Transactions on Signal Processing, **56**, 4794–4809.

Edme, P., E. Muyzert, and E. Kragh, 2014, Efficient land seismic acquisition sampling using rotational data: 76th EAGE Conference and Exhibition, Seismic Noise Attenuation Session, **ELI1 08**.

Fichtner, A. and H. Igel, 2009, Sensitivy densities for rotational ground-motion meaasurements: Bulletin of the seismological society of America, **99**, 1302–1314.

Gimlin, D. R. and J. W. Smith, 1980, A comparison of seismic trace summing techniques: Geophysics, **45**, 1017–1041.

Grazier, V. M., 2005, Effect of tilt on strong motion data processing: Soil Dynamics and earthquake engineering, **25**, 197–204.

Haines, S. S., 2004, Seismoelectric imaging of shallow targets: Ph.D. Thesis, Stanford Exploration Project.

Hamilton, S. W. R., 1844, On quaternions: or on a new system of imaginaries in algebra: Philosophical Magazine, **XXV**, 10–13.

Hanson, A. J., 2005, Visualizing quaternions: ACM SIGGRAPH 2005 courses, 1.

Hastie, T., R. Tibshirani, J. Friedman, and J. Franklin, 2005, The elements of statistical learning: data mining, inference and prediction: The Mathematical Intelligencer, **27**, 83–85.

Huang, B. S., 2003, Ground rotational motions of the 1999 chi-chi, taiwan earthquake as inferred from dense array observations: Geophysical Research Letters, **30**.

Huang, K. Y. and J. R. Yang, 2015, Seismic velocity picking using hopfield neural network: SEG Technical Program Expanded Abstracts, 5317–5321.

Igel, H., A. Cochard, J. Wasserman, U. Schreiber, A. Velikoseltsev, and N. D. Pham, , Broadband observations of rotational ground motions.

Igel, H., U. S. A. Flaws, B. Schuberth, A. Velikoseltsev, and A. Cochard, , Rotational motions induced by the M 8.1 tokachi-oki earthquake, september 25, 2003: Geophysical Research Letters, **32**.

Kappler, K., N. Cuevas, and J. W. Rector, 2006, Response of induction coil magnetometers to perturbations in orientation: SEG Technical Program Expanded Abstracts, 899–903.

Kendall, R., S. Jin, S. Ronen, and K. de Meersman, 2005, An SVD polarization filter for ground roll attenuation on multicomponent data: 928–931.

Key, K., 2003, Application of broadband marine magnetotelluric exploration to a 3d salt structure and a fast-spreading ridge: Ph.D. thesis: University of California, San Diego.

Kuzma, H. A. and J. W. Rector, 2005, Nonlinear AVO inversion using support vector machines: SEG Technical Program Expanded Abstracts, 203–206.

Lantz, B. R., B. Schofield, D. O'Reilly, D. E. Clark, and D. DeBra, 2009, Review: requirements for a ground rotation sensor to improve advanced LIGO: Bulletin of the seismological society of America, **99**, 980–989.

Lee, W. H. K., H. Igel, and M. D. Trifunac, 2009, Recent advances in rotational seismology: Seismological Research Letters, **3**, 479–490.

Li, Z. and M. van der Baan, 2015, Enhanced microseismic event localization by reverse time extrapolation: SEG Technical Program Expanded Abstracts, 4111–4115.

Lin, C. J., H. P. Huang, C. C. Liu, and H. C. Chiu, 2010, Application of rotational sensors to correcting rotation-induced effects on accelerometers: Bulletin of the

Seismological Society of America, **100**, 585–597.

Morse, P. F. and G. F. Hildebrandt, 1989, Groundroll suppression by the stackarray: GEOPHYSICS, **54**, 290–301.

Muyzert, E., A. Kashubin, E. Kragh, and P. Edme, 2012, Land seismic data acquisition using rotation sensors: 74th Conference and Exhibition, EAGE, Extended Abstracts.

Ostrander, W. J., 1984, Planewave reflection coefficients for gas sands at nonnormal angles of incidence: GEOPHYSICS, **49**, 1637–1648.

Pillet, R. and J. Virieux, 2007, The effects of seismic rotations on inertial sensors: Geophysical journal international, **171**, 1314–1323.

Pride, S., 1994, Governing equations for the coupled electromagnetics and acoustics of porous media: Physical Review B, **50**, 15678–15696.

Pujol, J., 2003, Elastic wave propagation and generation in seismology: Cambridge University Press.

Ronen, S., P. S. Schultz, M. Hattori, and C. Corbett, 1994, Seismicguided estimation of log properties (part 2: Using artificial neural networks for nonlinear attribute calibration): The Leading Edge, **13**, 674–678.

Schalkwijk, K. M., C. P. A. Wapenaar, and D. J. Verschuur, 2003, Adaptive decomposition of multicomponent ocean-bottom seismic data into downgoing and upgoing p- and s-waves: Geophysics, **68**, 1091–1102.

Schreiber, K. U., G. E. Stedman, H. Igel, and A. Flaws, 2006, Ring laser gyroscopes as rotation sensors for seismic wave studies: Earthquake source asymmetry, structural media and rotation effects, Springer, 377–390.

Trifunac, M. D., 2006, Effects of torsional and rocking excitations on the response of structures: Earthquake Source Asymmetry, Structural Media and Rotation Effects, 569–582.

Trifunac, M. D. and M. I. Todorovska, 2001, A note on the useable dynamic range of accelerographs recording translations: Soil Dynamics and earthquake engineering, **21**, 275–286.

Vassallo, M., K. Eggenberger, D. J. van Manen, K. Ozdemir, J. Robertsson, and A. Ozbek, 2012, Contributions of the horizontal and vertical components of particle velocity in 3D pressure wavefield reconstruction on dense receiver grids using generalized matching pursuit: SEG Technical Program Expanded Abstracts, 1–5.

Vidale, J. E., 1986, Complex polarization analysis of particle motion: Bulletin of the

Seismological society of America, **76**, 1393–1405.

Wong, M., B. L. Biondi, and S. Ronen, 2015, Imaging with primaries and free-surface multiples by joint least-squares reverse time migration: GEOPHYSICS, **80**, S223–S235.

Yuanyuan, L. and W. E. Holt, 2015, Wave gradiometry and its link with helmholtz equation solutions applied to usarray in the eastern us: Journal of Geophysical Research: Solid Earth, **120**, 5717–5746.

Zhao, T., V. Jayaram, K. J. Marfurt, and H. Zhou, 2014, Lithofacies classification in barnett shale using proximal support vector machines: SEG Technical Program Expanded Abstracts, 1491–1495.

Zhao, T. and K. Ramachandran, 2013, Performance evaluation of complex neural networks in reservoir characterization: Applied to boonsville 3-D seismic data: SEG Technical Program Expanded Abstracts, 2621–2625.

Zhou, Y., C. Kumar, and I. Ahmed, 2011, Ocean bottom seismic noise attenuation using local attribute matching filter: SEG Technical Program Expanded Abstracts, 3586–3590.